Coherently driven three-level atoms in an optical cavity

Dissertation

zur
Erlangung des Doktorgrades (Dr. rer. nat.)
der
Mathematisch-Naturwissenschaftlichen Fakultät
der
Rheinischen Friedrich-Wilhelms-Universität Bonn

vorgelegt von

Tobias Kampschulte

aus
Herne

Bonn 2011

Erratum

This thesis contains the following copyrighted material:

- Figure 1.5 has been adapted from Ref. [7]: M. Khudaverdyan, W. Alt, I. Dotsenko, T. Kampschulte, K. Lenhard, A. Rauschenbeutel, S. Reick, K. Schörner, A. Widera, and D. Meschede, *Controlled insertion and retrieval of atoms coupled to a high-finesse optical resonator*, New Journal of Physics **10**, 073023 (2008). Copyrighted by the Institute of Physics and the Deutsche Physikalische Gesellschaft.

- Figures 3.1, 4.1(a), 5.3, 5.4(b), and text on pages 68, 70–72 and 109 have been reprinted/adapted from Ref. [30]: T. Kampschulte, W. Alt, S. Brakhane, M. Eckstein, R. Reimann, A. Widera, and D. Meschede, *Optical control of the refractive index of a single atom*, Phys. Rev. Lett. **105**, 153603 (2010). Copyrighted by the American Physical Society.

- Figure 5.2(b) has been adapted with permission from Ref. [32]: G. Morigi, J. Eschner, and C. H. Keitel, *Ground state laser cooling using electromagnetically induced transparency*, Phys. Rev. Lett. **85**, 4458 (2000). Copyrighted by the American Physical Society.

- Figure 5.7(a) has been adapted with permission from Ref. [98]: L. Förster, M. Karski, J.-M. Choi, A. Stefen, W. Alt, D. Meschede, A. Widera, E. Montano, J. H. Lee, W. Rakreungdet, and P. S. Jessen, *Microwave control of atomic motion in optical lattices*, Phys. Rev. Lett. **103**, 233001 (2009). Copyrighted by the American Physical Society.

Please note:

Abstract

We experimentally realize strong light-matter coupling of a single cesium atom to a single mode of a high-finesse optical cavity. In this regime, the optical properties of one atom change the transmission spectrum of the resonator significantly. The two hyperfine ground states of cesium can be distinguished by the relative transmission of a weak probe beam coupled to the cavity. Here, we coherently couple the two hyperfine ground states via an electronically excited state with two-photon transitions.

In the first experimental configuration, two-photon Raman transitions are driven between the two ground states while continuously observing the atomic state. I present a new in-situ spectroscopic technique for the internal hyperfine and Zeeman-sublevel dynamics of an atom inside the cavity mode, using time-dependent Bayesian analysis of quantum jumps.

In the second configuration, the three-level atomic structure forms the basis of Electromagnetically Induced Transparency (EIT). The modification of the absorptive and dispersive properties of an atom by destructive interference leads to strong changes in the transmission of the probe beam. Our observations are qualitatively described in a semiclassical picture in the weak-probing limit. I furthermore present a fully quantum mechanical model, where deviations from the weak-probing limit, dephasing effects and other hyperfine states are taken into account to fit our data quantitatively. Moreover, I formulated an extension of the semiclassical model to highlight a conceptual contrast to the quantum model.

Additionally, the EIT effect is connected with a strong cooling effect, resulting in a 20-fold increase of the storage time of the atoms inside the cavity. I present further results of investigations of this effect where the atoms are trapped and EIT-cooled outside the cavity. From microwave sideband spectra it can be inferred that almost 80% of the atoms are in the ground state of motion along the trap axis.

Parts of this thesis have been published in the following journal articles:

- T. Kampschulte, W. Alt, S. Brakhane, M. Eckstein, R. Reimann, A. Widera, and D. Meschede, *Optical control of the refractive index of a single atom*, Phys. Rev. Lett. **105**, 153603 (2010).

Contents

Introduction

Since my childhood I am fascinated by the motion of celestial bodies such as the moon and the planets in our solar system. We can observe their dynamics governed by Newton's laws in real time with our own eyes. For me, one of the most impressive and esthetic views in nature is the sudden reappearance of brilliant sunlight at the end of a total eclipse — exactly at the predicted moment.

Our perception of the world is mainly conveyed by visible light, whose propagation is determined by the optical properties of the media. When a light wave travels through the atmosphere, its amplitude will first be damped by absorption, and might later be reflected or refracted at a water surface due to the different phase velocities in the two media. A simple model for the interaction of electromagnetic radiation and matter is the Lorentz model [1]: small harmonically oscillating dipoles, like bound electrons around their cores, are driven by the electric or magnetic field of the light, but also damped due to the emission of radiation. This corresponds to the semiclassical model of a weakly driven[1] two-level atom with a resonance frequency ν_0, where the excited state decays back into the ground state at a rate Γ. The linear response of such a the system to a weak probe beam with frequency ν can be described in terms of a complex refractive index $n_{\rm ref}$ or a linear susceptibility $\chi^{(1)}(\nu) = n_{\rm ref}^2 - 1$. Its real part determines the phase shift (dispersion), while the imaginary part quantifies the damping (absorption) of the electromagnetic wave.

But how can we measure the optical properties of a single atom — the most fundamental case? In free space, this is quite difficult, since the resonant cross section of an atom is only of the order of λ_0^2, where λ_0 is the wavelength of the resonant light. Even if one focuses the probing beam very tightly, the effects are at most on the level of a few percent [3]. They can be enhanced by many orders by placing the atoms into an optical cavity made of highly reflective mirrors. A photon inside the cavity can thus interact with the same atom for many times. In the so-called strong-coupling regime of cavity quantum electrodynamics [4,5], the dispersive and absorptive effects of one atom are thus sufficient to strongly change the transmission of the probe beam coupled into the resonator.

Methods to cool and trap neutral alkali atoms using lasers [6] have enabled us to realize the textbook model system of a two-level atom strongly coupled to a single mode of the electromagnetic field [7], as described by the Jaynes-Cummings Hamiltonian [8]. For a two-level atom, the linear susceptibility only depends on the difference $\nu - \nu_0$ between probe and resonance frequency. However, cesium

---

[1]In this case, the optical Bloch equations [2] are approximated by the damped harmonic oscillator.

atoms have two hyperfine ground states, so they can be at least regarded as three-level systems. We can tune our probe laser frequency and the cavity resonance frequency such that the probe transmission is suppressed only if the atom is in one of the two ground states (the coupled state). In contrast, the uncoupled state does not affect the transmission, as if no atom was in the cavity. This non-destructive[2] way of atomic state measurement has been developed and brought to perfection within the last few years [9–11]. In our experiment, the continuous observation of the cavity transmission reveals quantum jumps [12, 13] — random switching between two fixed values of the atomic susceptibility, corresponding to the coupled or the uncoupled ground state. This dynamics relies on incoherent processes like spontaneous photon scattering.

In this thesis, I present experiments where transitions in the three-level atom(s) are driven coherently. The two ground states are coupled by two-photon transitions via an excited state.

First, we combine a coherent two-photon Raman process [14] with the continuous, non-destructive measurement described above, causing decoherence by projecting the atom's state onto one of its eigenstates. Intriguing fundamental questions such as the role of the measurement process in quantum mechanics arise. The impedance of a coherent time evolution by a measurement, called Quantum Zeno effect [15], was first observed in ions [16, 17] and recently observed in atom-cavity systems [18, 19]. This effect plays certainly a role also in our system. Here, I focus on the application of coherently driven quantum jumps as an in-situ diagnostic method for the internal state dynamics of a single atom inside the cavity, what may be called quantum jump spectroscopy.

In another, fully coherent scheme we couple both ground states to a common excited state with a strong control and a weak probe laser, forming a so-called Λ-system. The refractive index of an atom in the coupled state for the probe laser does not only depend on $\nu - \nu_0$ as in a two-level system, but can be strongly modified by the control laser via a destructive interference effect called Electromagnetically Induced Transparency (EIT) [20, 21]. By tuning the frequencies of the two lasers relative to each other, an atom can be made purely absorptive or dispersive or it can even become transparent. This happens within a frequency range which is much narrower than the atomic linewidth Γ. The rapid change of dispersion can be utilized to slow down light pulses [22–25] or even store them in and retrieve them from an atomic ensemble [26–28]. EIT in systems like single ions in free space [29] has recently been observed. However, the effects are relatively weak and one usually requires large ensembles that are optically thick for the probe field in order to obtain strong effects.

Here, we utilize the coupling to our high finesse cavity in order to obtain strong EIT effects even with a single atom [30]. In contrast to the resonant regime $\nu \approx \nu_0$ described in [31], we study the off-resonant case $\nu - \nu_0 \gg \Gamma$, where both absorptive and dispersive effects can be detected. The effects can be described qualitatively

---

[2]The state measurement does not rely on the selective removal of atoms in an certain state.

in a semiclassical picture. However, for good quantitative agreement one requires a fully quantum mechanical simulation, taking into account other excited hyperfine states and dephasing effects. In particular, I theoretically show that the cavity not only increases the sensitivity compared to probing in free space but also contributes to the probe transmission due to the strong atom-cavity coupling.

So far, only the dynamics of the internal atomic state have been considered. However, due to the Doppler effect, the scattering rate of near-resonant laser light strongly depends on the motion of the atom with respect to the beam direction. Making use of this effect results in Doppler laser cooling [6], which enables us to slow down the atoms sufficiently in order to trap them in our optical traps. The theoretical temperature limit T_D for Doppler cooling is related to the atomic linewidth: $T_D \approx \hbar\Gamma/2k_B$, where k_B is the Boltzmann constant. In our off-resonant regime, the EIT effect leads to the creation of an absorption peak which is much narrower than Γ. This gives rise to a sub-Doppler cooling mechanism [32], as has been demonstrated with trapped ions [33, 34]. We observe a strong increase of the storage times of atoms in our cavity on EIT resonance [30], which improves the stability of the atom-cavity coupling. Moreover, we investigate this EIT cooling effect outside of the cavity and show that a large fraction of the atoms is cooled to the quantum mechanical ground state in one dimension of the harmonic trapping potential.

1 Experimental setup

In this chapter, I will introduce the basic techniques used in the experiments presented in this thesis: cooling of trapping of a small number of atoms, precise positioning of the atoms in a high-finesse optical cavity followed by the detection of the strong light-matter coupling, and coherent manipulation and readout of the atoms' internal quantum state.

These tools and techniques have been developed and integrated into the experimental setup during the past decade. They are described in more detail in various doctoral theses [35–41] and Diplom theses [42–49]. Here, I will give a brief overview.

1.1 Laser-cooled atoms on demand

This section presents our tools to prepare a predetermined number of atoms inside the high-finesse optical resonator by means of a magneto-optical trap and an optical dipole trap, utilized as a conveyor belt.

1.1.1 Magneto-optical trap

A small number of neutral cesium atoms is cooled and trapped from the background gas in a magneto-optical trap (MOT) [6] inside a ultra-high vacuum chamber. The MOT is formed by three pairs of counter-propagating laser beams (optical molasses) in combination with a magnetic quadrupol field, see Fig. 1.1. The magnetic field gradient can be switched from a low value (30 G/cm) with a high atomic loading rate to a high value (300 G/cm) with slow loading but strong confinement of the atoms to about 15 μm. Loading a single atom into the MOT usually takes a few tens of milliseconds. The number of atoms inside the MOT is inferred from the fluorescence light collected with a specially designed objective lens [50] and detected with a single-photon counting module. For a single atom, the count rate is about $3 \times 10^4\,\mathrm{s}^{-1}$. A desired number of atoms is prepared by repeatedly loading the MOT until the corresponding count rate is detected [51].

1.1.2 Dipole trap and optical conveyor belt

The MOT relies on the continuous, near-resonant scattering of photons. Hence it is not suitable for the coherent manipulation of the quantum state of the atoms, because any coherences between states would be destroyed immediately. Therefore, we transfer the atoms from the MOT into the quasi-conservative potential of a far-off-resonant dipole trap (DT) [52]. In our case, two counter-propagating, linearly
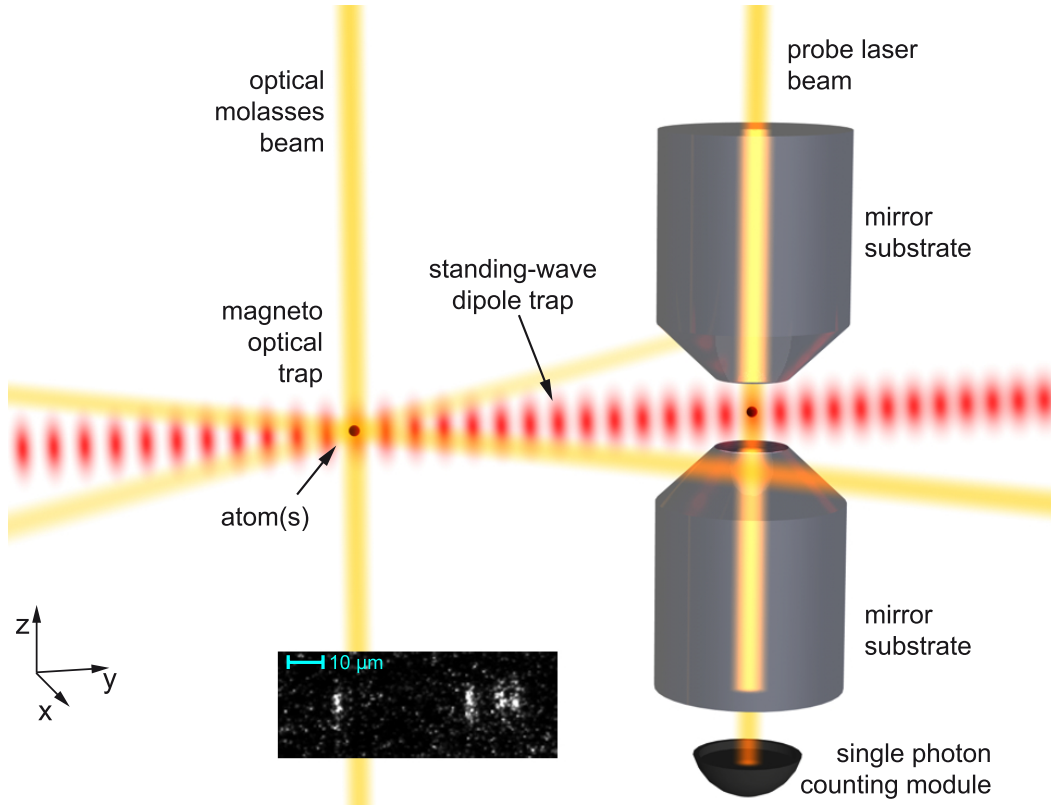
Figure 1.1: Schematic view of the experiment. A small number of cesium atoms
is cooled and trapped in a magneto-optical trap and subsequently transferred
into a standing-wave dipole trap. After determining their positions from a
fluorescence image (*inset*: four atoms in the dipole trap), they are transported
into the center of a high-finesse optical resonator. The coupling of the atom(s)
to the cavity mode is probe by a weak probe laser beam whose transmission is
measured with a single photon counting module.

polarized laser beams of wavelength $\lambda_{\mathrm{DT}} = 1030\,\mathrm{nm}$ and a total power of about
$P = 3.6\,\mathrm{W}$ form a standing-wave with periodicity $\lambda_{\mathrm{DT}}/2$. This one-dimensional
optical lattice strongly confines the atoms along the y-axis, see Fig. 1.1. We achieve
typical trap depths of about $U_0 = k_{\mathrm{B}} \times 1\,\mathrm{mK}$, where k_{B} denotes the Boltzmann
constant. Illuminating the atoms inside the DT with the optical molasses beams not
only cools them further down to about $30\,\mu\mathrm{K}$ [37], but allows us to take fluorescence
images [53] using an intensified CCD-camera (ICCD, ROPER SCIENTIFIC PI-MAX)
to determine their positions along the DT with sub-wavelength resolution [54].

Moreover, the standing wave dipole trap is used as an optical conveyor belt to
transport the atoms with sub-micrometer precision [54] over several millimeters
along the trap axis. This is realized by detuning the frequencies of the two counter-
propagating beams with respect to each other by means of acousto-optic modulators
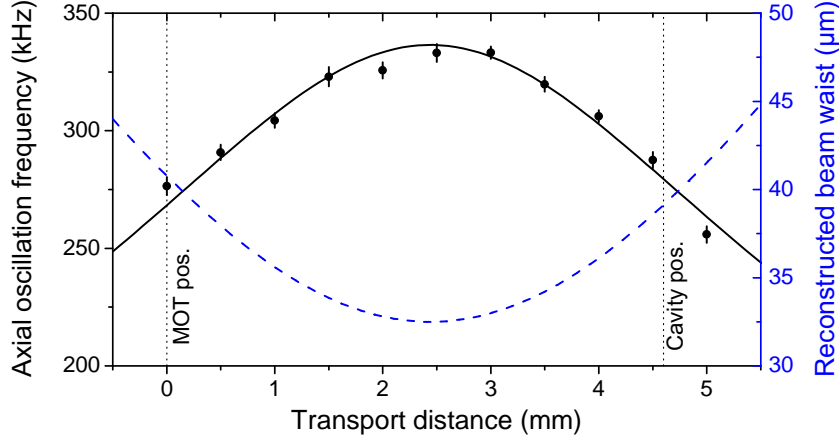
Figure 1.2: Axial trap frequencies, inferred from microwave sideband spectroscopy, as a function of the position along the dipole trap axis. The experimental data are fitted with a model (solid line, Eqn. (1.2)) assuming a Gaussian beam profile to obtain the position y_0 of the minimum beam waist. From this fit, the beam waist along the trap axis is reconstructed (dashed line).

(AOMs). Atoms are transported from the position of the MOT to the center of the high-finesse optical resonator, which is 4.6 mm apart and within a typical time of 2 ms.

Characterizing the optical dipole trap

The standing wave optical dipole trap is formed by Gaussian laser beams. They are focused from outside the vacuum chamber using lenses to a minimum $1/e^2$-radius (waist) of $w_{\text{DT},0} = (32.5 \pm 0.4)\,\mu\text{m}$[1] at a position y_0 along the y-axis. For other positions along this axis, the beams diverge according to

$$w_{\text{DT}}(y) = w_{\text{DT},0}\sqrt{1 + \left(\frac{y - y_0}{y_\text{R}}\right)^2}, \quad \text{where} \quad y_\text{R} = \frac{\pi w_{\text{DT},0}^2}{\lambda_{\text{DT}}}. \tag{1.1}$$

Here, $y_\text{R} = (3.2 \pm 0.1)\,\text{mm}$ is the Rayleigh range [55]. The beam divergence leads to a decreasing intensity, and with it, a decreasing trap depth $U_0(y)$ with increasing $|y - y_0|$. The optimum position of the minimum waist is somewhere in between the MOT and the cavity position: At the MOT position, the trap should not be too shallow in order not to lose the atoms from the trap during the exposure of the image. At the cavity position, the confinement should also be as good as possible to achieve a high and stable coupling of the atom(s) to the cavity mode.

The precise knowledge of the position y_0 of the minimum waist is very valuable since the oscillation frequencies of the atoms inside the trap and the AC-Stark

---

[1]inferred from measurements with a beam profile camera

shifts of atomic resonance frequencies depend on the trap depth, and thus on the position. Determining y_0 *inside* the chamber from a measurement *outside* the chamber, e.g. by means of a mirror and a beam profile camera, turns out to be very difficult. Here, I infer the beam profile from the axial oscillation frequencies $\nu_{\text{ax}}(y)$ of the atoms at different positions along the trap axis: On one hand, the trap depth $U_0(y)$ is proportional to $\nu_{\text{ax}}^2(y)$. On the other hand, it is proportional to the intensity $I_{\text{DT}} = 4P/(\pi w_{\text{DT}}^2)$ at the antinodes of the standing wave, which is inversely proportional to w_{DT}^2. The beam waist is thus inversely proportional to the trap frequency, yielding

$$\nu_{\text{ax}}(y) = \nu_{\text{ax},0} \times \frac{w_{0,\text{DT}}}{w_{\text{DT}}(y)} = \frac{\nu_{\text{ax},0}}{\sqrt{1 + (y - y_0)^2/(y_{\text{R}})^2}} \,, \tag{1.2}$$

where $\nu_{\text{ax},0}$ denotes the maximum trap frequency.

The axial oscillation frequencies are measured at a total power of $P = 3.7\,\text{W}$ by microwave sideband spectroscopy. For this, the directions of the linear polarizations of the two beams are rotated with respect to each other by an angle $\theta = 26°$. More details on this technique are given in section 5.3.1. The experimental data for $\nu_{\text{ax}}(y)$ have been fitted with Eqn. (1.2), where y_0 and $\nu_{\text{ax},0}$ are free parameters, see Fig. 1.2. The results are

$$y_0 = (2.44 \pm 0.05)\,\text{mm}, \quad \text{and} \quad \nu_{\text{ax},0} = (336 \pm 2)\,\text{kHz}, \tag{1.3}$$

respectively. This means that the minimum waist is almost exactly in between the MOT and the cavity position, cf. [37, 38]. The beam radius $w_{\text{DT}}(y)$ is then reconstructed using Eqn. (1.1), see Fig. 1.2. In particular, the obtained beam radii at the positions of the MOT and the cavity are

$$w_{\text{DT,MOT}} = (40.8 \pm 1.6)\,\text{µm}, \quad \text{and} \quad w_{\text{DT,cav}} = (39.1 \pm 1.5)\,\text{µm}, \tag{1.4}$$

respectively.

From the maximum trap frequency $\nu_{\text{ax},0}$ I infer a maximum trap depth of

$$U_0(y = y_0) = h \times (22.1 \pm 0.3)\,\text{MHz} = k_{\text{B}} \times (1.06 \pm 0.01)\,\text{mK}, \tag{1.5}$$

for details see section 5.3.1. This value is about 80% of $h \times (28.2 \pm 0.7)\,\text{MHz}$ calculated from the intensity I_{DT} [36]. The discrepancy may arise from a non-perfect beam overlap and optical abberations.

1.2 Coupling atoms to a high-finesse cavity

To efficiently couple our atom(s) to a single mode of the electromagnetic field, i.e. a Gaussian TEM_{00} mode, we position the atom(s) in the center of the high-finesse optical resonator inside our evacuated glass cell, see Fig. 1.1. The cavity consists of a pair of super-polished mirror substrates with highly-reflective coatings. Details on the characterization of the cavity and its technical implementation into the setup

Parameter	Symbol	Value
Mirror distance	l	$158.5\,\mu\text{m}$
Mode waist	$w_{0,\text{cav}}$	$23.15\,\mu\text{m}$
Free spectral range	$\omega_{\text{FSR}} = 2\pi c/(2l)$	$2\pi \times 946\,\text{GHz}$
Mirror transmission[†]	$\mathcal{T}$	$(0.6 \pm 0.1) \times 10^{-6}$
Mirror absorption[†]	$\mathcal{A}$	$(2.0 \pm 0.2) \times 10^{-6}$
Cavity field decay rate[†]	$\kappa \approx \omega_{\text{FSR}}(\mathcal{T} + \mathcal{A})/2\pi$	$2\pi \times (0.40 \pm 0.02)\,\text{MHz}$
Cavity line width (FWHM)[†]	$\omega_{\text{FWHM}} = 2\kappa$	$2\pi \times (0.80 \pm 0.04)\,\text{MHz}$
Finesse[†]	$\mathcal{F} = \omega_{\text{FSR}}/\omega_{\text{FWHM}}$	$(1.2 \pm 0.1) \times 10^{6}$
Birefringent splitting	$\Delta\omega_{\text{br}}$	$2\pi \times 3.9\,\text{MHz}$
Max. coupling strength	$g_{0,\text{max}}$	$2\pi \times 13.1\,\text{MHz}$
Atomic dipole decay rate	$\gamma = \Gamma/2$	$2\pi \times 2.6\,\text{MHz}$
Single-atom cooperativity	$C_1 = g_{\text{max}}^2/(2\kappa\gamma)$	82

Table 1.1: Some important cavity and coupling parameters, from [38]. The mirror distance l is given for typical experimental conditions, including heating effects by the dipole trap laser beams (the value in [36] is valid for the 'cold' cavity) [38], see also section 1.2.3. [†]For details on the measurement of these values, see [47]. The birefringent splitting $\Delta\omega_{\text{br}}$ is the difference between the resonance frequencies of two orthogonal, linear polarization modes of the cavity [36]. The maximum coupling strength $g_{0,\text{max}}$ is calculated for the atomic $|F = 4\rangle \leftrightarrow |F' = 5\rangle$ transition and linearly polarized light [38].

are discussed in [7, 36–38, 47]. Here, the main parameters are as summarized in table 1.1.

The low transmission and absorption[2] losses $\mathcal{T}$ and $\mathcal{A}$ of the mirrors result in a high finesse $\mathcal{F} \approx \pi/(\mathcal{T} + \mathcal{A})$ [38]. In a vivid picture, a photon inside the cavity would be reflected $\mathcal{F}/\pi \approx 400{,}000$ times on average before getting lost. Due to the confinement of the electromagnetic field to a small mode volume [36],

$$V_{\text{mode}} = \frac{\pi}{4} w_{0,\text{cav}}^2 l, \qquad (1.6)$$

the coherent energy exchange rate $g = g(\vec{r})$ between the cavity field and the electric dipole moment of the atom [36]

$$g \leq g_0 = d\sqrt{\frac{\omega}{2\hbar\epsilon_0 V_{\text{mode}}}} \qquad (1.7)$$

can be higher than the decay rates of the cavity field κ and of the atomic dipole γ (Here, d denotes the electric dipole moment and ω denotes the resonance frequency of the atomic transition. The value g_0 is valid for an atom at an electric field maximum.). In this so-called strong coupling regime, the transmission spectrum of the

---

[2]includes also the scattering of light into other spatial modes due to the mirror roughness

(a)

(b)
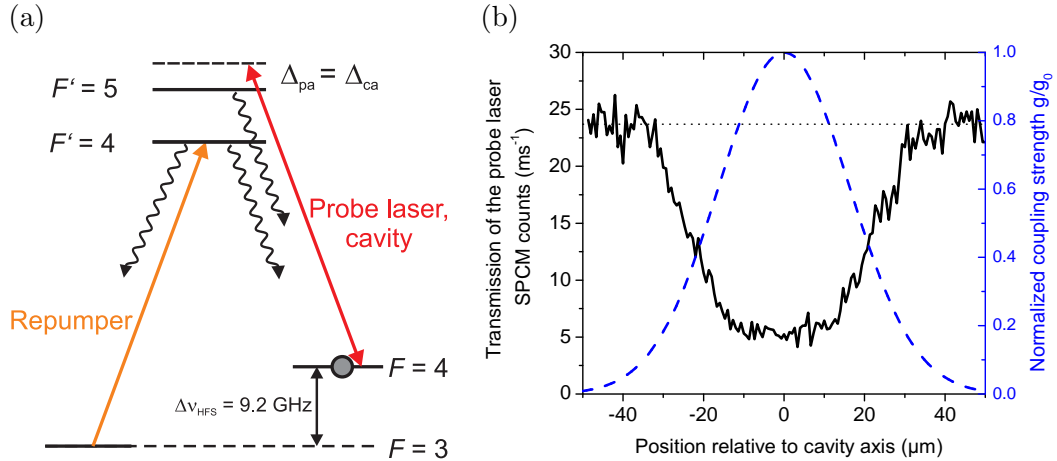
Figure 1.3: (a) Level scheme of the relevant hyperfine states for the transmission detection of atoms inside the cavity. Both the probe laser and a cavity mode are near-resonant with the atomic $|F = 4\rangle \leftrightarrow |F' = 5\rangle$ transition, a quasi-two-level system. However, due to off-resonant excitation of the state $|F' = 4\rangle$, an atom can also decay into the state $|F = 3\rangle$, from where it has to be repumped to $|F = 4\rangle$. (b) Transmission of the probe laser through the cavity (solid line) as a function of the position of a single atom in state $|F = 4\rangle$ (average over 19 experimental runs; adapted from [7]). The decrease in transmission with respect to the empty-cavity transmission (dotted line) reflects the Gaussian profile of the cavity mode (dashed line).

cavity is already changed significantly by the presence of only a single atom inside the mode. This can also be expressed in terms of the single-atom cooperativity $C_1 = g^2/(2\kappa\gamma)$. The transmission of a probe laser, which is resonant with both the cavity and the atomic transition, decreases by a factor of $(1 + 2C_1)^2$ when the atom couples to the mode. For a general model for the transmission with two- and three-level atoms inside a cavity, see chapter 3.

1.2.1 Detecting a single atom inside the cavity

The transmission of a probe laser beam through the cavity is our main source of information about the atom-cavity system. The transmitted light is detected on a single-photon counting module (SPCM, PERKIN ELMER SPCM-AQRH-13). The total detection efficiency for photons that decay from the cavity mode, including mirror losses and other coupling efficiencies is $\eta = 5.7\%$ [3]. For more details on the detection setup see [47].

---

[3] with an optional interference filter, it is only $\eta = 4.4\%$ [38]

Detection scheme

The typical detection scheme for atoms inside the cavity mode works as follows:
The probe laser (angular frequency ω_p) is resonantly coupled into the cavity mode
(angular frequency ω_c), i.e. the probe-cavity detuning is $\Delta_\mathrm{pc} \equiv \omega_\mathrm{p} - \omega_\mathrm{c} = 0$. The
power is adjusted such that the transmitted light causes a photon count rate of
typically $R_\mathrm{D} = 30\,\mathrm{ms}^{-1}$ on the SPCM. This rate corresponds to a mean intracavity
photon number of (cf. [38])

$$n_\mathrm{p,0} = \frac{R_\mathrm{D}}{\kappa\eta} = 7.0 \times 10^{-3} \times \frac{R_\mathrm{D}}{1\,\mathrm{ms}^{-1}} = 0.21, \tag{1.8}$$

so in 98% of the time there is at most one excitation in the cavity mode. Both the
cavity and the probe laser are near resonant with the atomic $|F = 4\rangle \leftrightarrow |F' = 5\rangle$
transition (angular frequency ω_a) of the D_2-line at a wavelength of $852\,\mathrm{nm}$, see
Fig. 1.3 (a). Since an atom in the excited state $|F' = 5\rangle$ can only decay back into
$|F = 4\rangle$ (selection rule: $|F' - F| \leq 1$), the two states form a quasi-two-level atomic
system. More precisely, we blue-detune both the cavity and the probe laser from
the atomic transition frequency by several atomic linewidths Γ:

$$\Delta_\mathrm{ca} \equiv \omega_\mathrm{c} - \omega_\mathrm{a} \approx 2\pi \times (20\ldots 40)\,\mathrm{MHz}, \tag{1.9}$$

$$\Delta_\mathrm{pa} \equiv \omega_\mathrm{p} - \omega_\mathrm{a} = \Delta_\mathrm{ca}. \tag{1.10}$$

When an atom in state $|F = 4\rangle$ is inside the cavity mode, the coupling g leads
to a dispersive shift of the cavity frequency by approx. g^2/Δ_ca, which can amount
to several cavity linewidths 2κ. The cavity is thus shifted out of resonance with
the probe laser and the transmission of the latter strongly decreases. However,
due to off-resonant inelastic Raman scattering, the atom can also leave the two-
level system and end up in $|F = 3\rangle$, the other hyperfine ground state. Due to
the large hyperfine splitting of $\Delta\nu_\mathrm{HFS} \approx 9.2\,\mathrm{GHz}$, the atom is then effectively
decoupled from the cavity. To counteract this, a repumping laser resonant with the
$|F = 3\rangle \leftrightarrow |F' = 4\rangle$ transition is shone onto the atoms to transfer them back to
$|F = 4\rangle$.

We demonstrate the controlled coupling of a single atom to the cavity mode
by shifting it within $(50..200)\,\mathrm{ms}$ through the Gaussian-shaped cavity mode [see
Eqn. (4.16)], using the optical conveyor belt, see Fig. 1.3 (b). At the cavity center,
the coupling strength is maximum (g_0) and the transmission reaches its minimum.
Moreover, we use this method as a preparatory step to calibrate the scale of our
fluorescence images such that the atoms are always transported to the center of the
cavity.

1.2.2 Trapping and cooling atoms inside the cavity

As described above, the atoms are trapped inside the cavity by the far-red-detuned
standing wave optical dipole trap, providing a strong confinement along the y-axis.
But confinement is also provided along the cavity axis: A blue-detuned standing

Figure 1.4: Illustration of the trapping potentials inside the cavity. The atoms are trapped in the pancake-shaped intensity maxima of the red-detuned dipole trap along the y-axis. In addition, the standing wave of the blue-detuned lock laser light forms potential walls inhibiting free atomic motion along the z-axis.
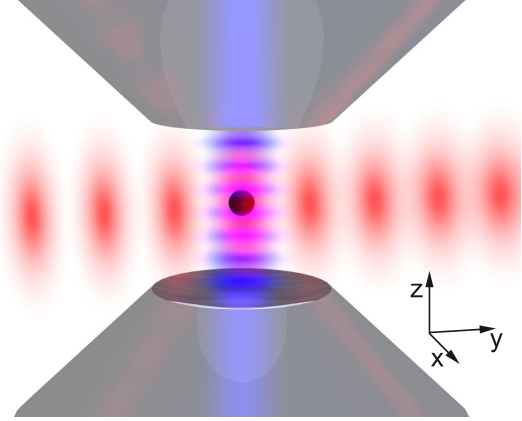
wave, caused by the so-called lock laser. The latter is needed for the active stabilization of the cavity length l, which will be discussed in the next section. While the probe laser is coupled to a longitudinal cavity mode that is near-resonant with the atoms, the lock laser is resonant with a different cavity mode whose frequency is $\Delta n_{\mathrm{FSR}} = 3$ free spectral ranges apart at $\lambda_{\mathrm{lock}} = 845\,\mathrm{nm}$ to avoid photon scattering by the atoms. However, the lock laser standing wave acts as a blue-detuned dipole trap inside the cavity, repulsing the atom(s) from the intensity maxima, see Fig. 1.4. Those potential hills are of similar height as the depth of the potential wells of the conveyor belt dipole trap. We have also demonstrated that a red-detuned, attractive lock laser standing wave at $\lambda_{\mathrm{lock}} = 857\,\mathrm{nm}$ can trap the atoms for several hundred milliseconds even if the conveyor belt dipole trap is switched off [38].

Trapping potentials and atomic motion

The two crossed standing waves along the y-axis and the z-axis form a two-dimensional optical lattice. Atoms are strongly confined along these axes but only weakly confined along the x-direction. Although the positions of the atoms along the y-axis can be precisely controlled by the optical conveyor belt, they can move around the potential walls of the lock laser standing wave and can thus change their position along the cavity axis. Due to the different wavelengths of the probe and the lock laser, the corresponding standing waves have a different periodicity. Hence the nodes of the lock laser standing wave, where the atoms are confined, coincide with different phases of the probe laser standing wave, see Fig. 1.5 (a). When atoms are confined around the antinodes of the probe laser standing wave, they are maximally coupled with $g = g_0$ to the cavity mode. Conversely, if they are at a node, the coupling strength g vanishes. The distance between trapping positions of the same phase is called beat length [38]

$$d_{\mathrm{beat}} = \frac{\lambda_{\mathrm{probe}}\lambda_{\mathrm{lock}}}{2|\lambda_{\mathrm{probe}} - \lambda_{\mathrm{lock}}|} = \frac{l}{\Delta n_{\mathrm{FSR}}}\,, \tag{1.11}$$
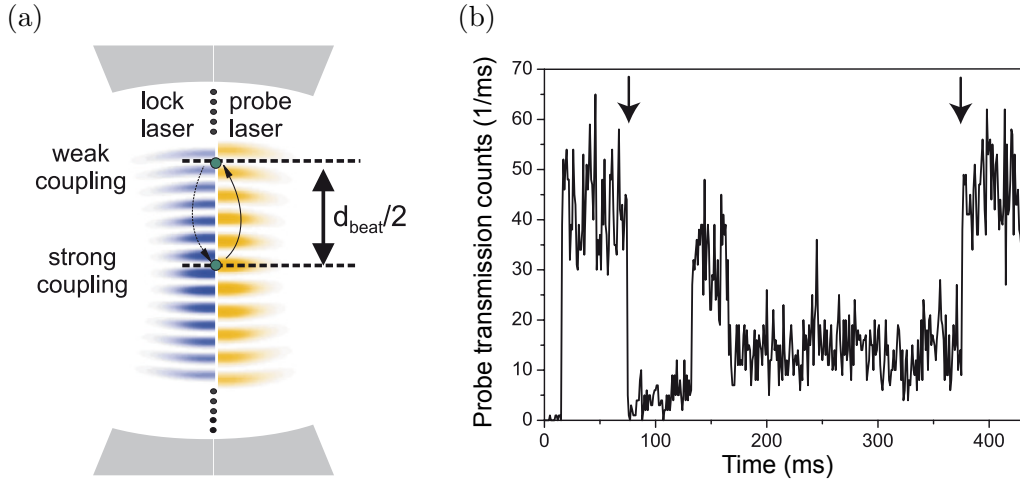
Figure 1.5: (a) Beating between the probe and lock laser standing waves inside the cavity. Atoms can be trapped at an antinode of the probe laser standing wave with maximum atom-cavity coupling or at a node where it vanishes. (b) Transmission of the probe laser beam through the cavity as a function of time. In the time interval between the two arrows, one atom is held inside the cavity mode. Figures taken from [7].

which equals to $l/3 = 52.8\,\mu$m for $\lambda_{\text{lock}} = 845\,$nm. Such a beat length is comparable with the beam radius $w_{\text{DT,cav}}$ of the dipole trap. Therefore, atoms are placed more or less randomly at vertical positions with strong and weak coupling when they are inserted into the cavity and may also 'hop' between those positions, causing random transmission fluctuations, see Fig. 1.5 (b). The average coupling is maximized by vertically aligning the dipole trap axis onto the strongly coupled sites, i.e. onto the cavity center if Δn_{FSR} is an odd number.

This dynamics is still the major obstacle for a reproducible and stable coupling of atoms to the cavity mode. One idea to improve the radial confinement of the atoms is the implementation of an additional, tightly focused dipole trap with a minimum waist at the cavity position [37].

Heating and cooling

The external dynamics of the atom is not only determined by its initial kinetic energy and the trapping potential, but also influenced by heating and cooling mechanisms inside the cavity. There are basically two different physical processes: The first one is the temporal fluctuation of the trapping potential(s) leading to resonant or parametric heating [35]. The second mechanism is near-resonant interaction of the atoms with laser light where the exchange of photon momenta leads to heating or cooling forces. Moreover, the interaction of two-level atoms with the field of an optical cavity can induce strong cooling forces [56].

Figure 1.6: Locking scheme for the frequency stabilization of the QED cavity. The error signals comparing two successive components are generated by Doppler-free polarization spectroscopy (spetr.) and by the Pound-Drever-Hall (PDH) method, respectively. Solid arrows 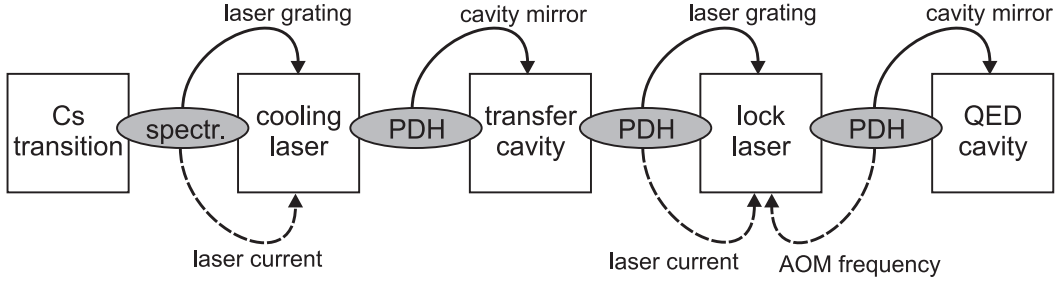indicate the slow branches of the control loops, where the feedback acts on laser gratings or cavity mirrors, respectively. Dashed arrows indicate fast feedback either to the laser diode currents or via an acousto-optical modulator (AOM).

Since the competition between cooling and heating rates determine the steady-state temperature and with it the trapping time of the atoms, one aims at avoiding heating processes and exploiting cooling mechanisms. Cavity cooling has enabled long storage times in experiments [57] and is probably of relevance also for our system [7, 38]. In particular, we observe that blue-detuning of both the cavity and the probe laser by the same amount from the atomic $|F = 4\rangle \leftrightarrow |F' = 5\rangle$ transition leads to trapping times of up to one minute.

Atoms inside the cavity are always heated by the fluctuations of the trapping potentials, especially by the intensity fluctuations of the lock laser standing wave. These fluctuations are caused by relative frequency fluctuations between the lock laser and the cavity. Since the lock laser wavelength serves as a reference for the cavity length, a perfect stabilization would suppress any fluctuations. In the early times of the experiment, the average trapping time was only about $20\,\mathrm{ms}$ [37]. Since then, much effort has been spent to characterize and improve the whole stabilization setup [44, 45] and to minimize the relative frequency fluctuations and with it the intensity fluctuations. In the next section, I will discuss this in more detail.

1.2.3 Lock chain and stabilization of the cavity

The active stabilization of the cavity length l with respect to the probe laser wavelength λ_{probe} is crucial for all experiments inside the cavity that rely on the detection of a change of the probe laser transmission. One can make a rough estimation on the required stability: The relative frequency fluctuations $\Delta\nu$ should be much less than the cavity linewidth $\omega_{\mathrm{FWHM}} = 2\kappa$. The cavity frequency changes by about $\Delta\omega_{\mathrm{FSR}}$ if we change its length by $\Delta l = \lambda_{\mathrm{probe}}/2$. This means, the frequency changes already by $\omega_{\mathrm{FWHM}} = \Delta\omega_{\mathrm{FSR}}/\mathcal{F}$ if we change the cavity length by only $\Delta l = \lambda_{\mathrm{probe}}/(2\mathcal{F}) \approx 4 \times 10^{-13}\,\mathrm{m}$! Although it might sound impossible to fulfil

this requirement, we are able to stabilize length by means of a shear-piezoelectric transducer (PZT) to better than $\Delta l/10$ — So how does it work?

In general, a relative stabilization (lock) between the frequencies of two elements is achieved using a servo loop. Such a loop requires a method that generates an error signal that is proportional to the difference between the two frequencies. In case of a laser and a cavity, we use the Pound-Drever-Hall method (PDH) [58]. The error signal is then processed by linear analog electronics (operational amplifiers and filters) and applied to an actuator, e.g. a PZT element that moves the grating of a diode laser or a cavity mirror, to counteract the disturbance and cause negative feedback.

However, there cannot be a direct lock between the high-finesse cavity inside the vacuum (QED cavity) and the probe laser, because we would need to permanently couple near-resonant probe light with relatively high power into the cavity. This would be incompatible with any reasonable measurement. Therefore, we need to go a long way round and stabilize the cavity on the lock laser which is far-detuned from any atomic transition in cesium. This also means that there is no simple spectroscopic way of generating an error signal.

The whole lock chain consists of four stages, see Fig. 1.6: The cooling laser, where the probe beam is derived from, is stabilized on the cesium transition frequency. The error signal is generated in a Doppler-free polarization spectroscopy. It is then processed and fed back on both the laser grating PZT (to correct for long-term drifts) and the laser diode current (to suppress fast fluctuations). The second stage is the lock between a transfer cavity and the cooling laser frequency with a (slow) feedback of the PDH error signal on the cavity mirror by a PZT. The lock laser is stabilized on a different longitudinal mode of the transfer cavity by a slow grating feedback and a fast current feedback. Finally, the lock laser and the QED cavity are stabilized with respect to each other.

For more details on the first three stages, see [7, 35, 42, 44, 53]. During my time at the experiment, I focused on the improvements of the last locking stage.

Improvements of the QED cavity lock

As discussed in the previous section, the atoms are heated inside the QED cavity by the fluctuating trapping potential created by the lock laser light, caused by relative frequency fluctuations between the lock laser and the cavity at several kilohertz. Another problem occurs on the timescale between 10 and 100 milliseconds: When loading atoms from the MOT into the dipole trap, laser beams are switched on. A tiny fraction of the dipole trap beams hits the QED cavity mirrors and heats them up, causing a change of the cavity length. Then, the cavity frequency changes by more than $100,000$ linewidths per second! Since the capture range of the PDH error signal, i.e. the maximum frequency deviation that causes a negative feedback, is only on the order of 100 linewidths, the servo loop can sometimes not counteract the heating and the cavity falls 'out of lock'.
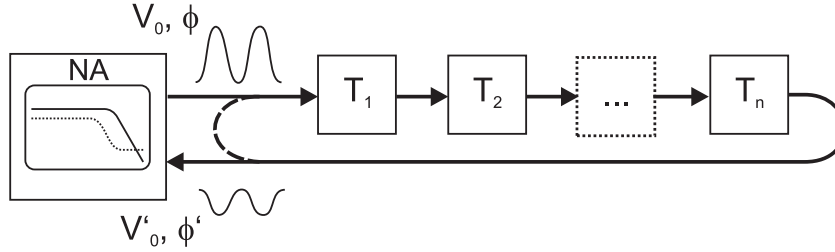
Figure 1.7: Characterizing a servo loop with a network analyzer (NA): if all elements $T_1, \ldots, T_n$ are linear, the control loop can be opened at any point (dashed curve) and the amplitude V_0 and phase ϕ of a sinusoidal input voltage can be compared with the output amplitude V_0' and phase ϕ', respectively. From this, one obtains loop gain $G = |V_0'/V_0|^2$ and phase delay $\Delta\phi = \phi' - \phi$ of the servo loop.

Analysis of the servo loop   To improve the performance of the QED cavity lock, one first needs to analyze the corresponding servo loop. In general, a servo loop consists of a closed chain of different elements $T_1, \ldots, T_n$ that process a signal, see Fig. 1.7. The signal can be represented in frequency space by amplitude $V_0(f)$ and phase $\phi(f)$. In case they are linear, the effect of the elements on the signal can be described by a gain $G(f) = |V_0'(f)/V_0(f)|^2$ and a phase shift $\Delta\phi(f) = \phi'(f) - \phi(f)$. These quantities can be measured by opening the loop at any point and connecting the ends to a network analyzer. An ideal servo loop would have infinite open-loop gain $G(f) \to \infty$ and a phase shift of $\Delta\phi(f) = -180°$ (negative feedback) for arbitrary high signal frequencies f. However, in real life, bandwidth limits cause usually additional phase delays and decreasing gain at high f. Above a certain frequency, the phase shift will reach $\Delta\phi = -360°$, turning the negative feedback into a positive feedback. If the gain at that frequency is still larger than unity, the servo loop is unstable and starts to oscillate. For the simplest case that the open-loop gain crosses the $0\,\text{dB}$-line only once, i.e. at the unity-gain frequency $f_{0\text{dB}}$, where $|G(f_{0\text{dB}})| = 1$, one can state the following Nyquist stability criterion [59]: A closed feedback loop is stable, if the phase margin $\Delta\phi(f_{0\text{dB}}) + 360°$ is positive at the unity-gain frequency $f_{0\text{dB}}$.

We analyze the properties of the servo loop for the PZT feedback on the cavity length by coupling a laser beam at a wavelength of $975\,\text{nm}$ into the cavity [44]. At that wavelength, the cavity finesse is only about 200 and therefore it is easy to manually control the offset such that the transmission of this laser is about 50% of the maximum transmission. Here, a change of the cavity length translates in first order linearly into a transmission change. The network analyzer output is connected to the error-signal input of a *lockbox*, a proportional-integral (PI) controller where the total gain and the proportional gain (P-Gain) can be varied independently. The output of the lockbox is coupled via a high-voltage amplifier and a resistor $R = 260\,\text{k}\Omega$ to the PZT. The capacity of cables and PZT of about $C = 500\,\text{pF}$
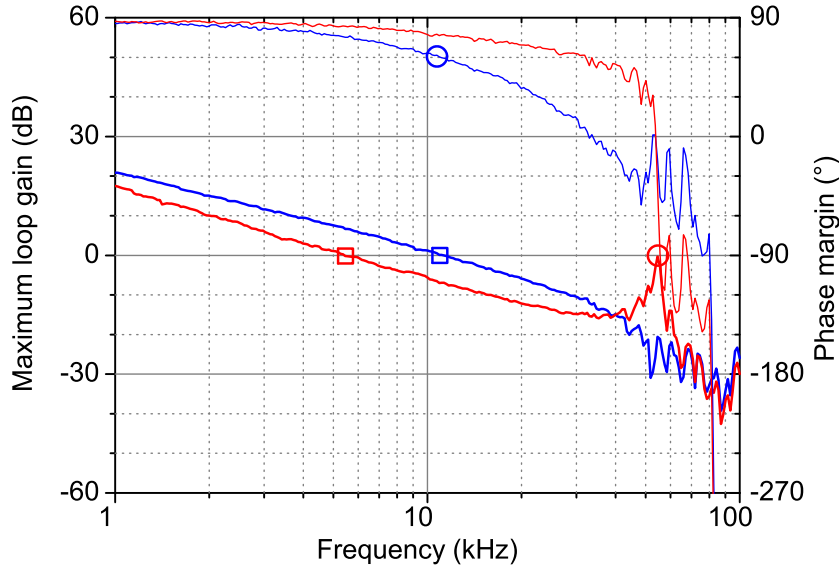
Figure 1.8: Open-loop gain (thick lines) and phase margin (thin lines) of the PZT servo loop for the QED cavity. Without notch filter (red), the mechanical PZT resonances are clearly visible (circle), limiting the the servo bandwidth to about 5 kHz (square). With notch filter (blue), the resonances are suppressed, but the phase margin decreases much earlier (circle), limiting the servo bandwidth to about 10 kHz (square).

and the resistor form an *RC*-lowpass filter with a cutoff-frequency of about 1 kHz, see Fig. 1.9 (1). The transmission of the 975 nm laser is measured by a photodiode which is connected to the input of the network analyzer. In this way, we obtain the open-loop gain and phase of the control loop, also called *Bode plot*, see Fig. 1.8.

Between 1 and 10 kHz, the gain decreases with about −20 dB/decade as is characteristic for an effective integrator, see Fig. 1.9 (3). This can be achieved by setting the P-gain of the lockbox such that it cancels the effect of the lowpass filter. At around 50 kHz, strong mechanical PZT resonances appear and the phase margin steeply decreases. The overall gain, i.e. the vertical position of the gain-curve in this log-log diagram is obviously limited by these resonances: They should be kept well below 0 dB, otherwise the closed loop would start to oscillate. So the servo bandwidth is limited to about 5 kHz (first 0 dB-crossing). On the one hand, the resonances can be suppressed by inserting a notch filter between the HV-amplifier and lowpass [42], as can be seen in the other graph in Fig. 1.8. On the other hand, the additional filter causes the phase margin to decrease at lower frequencies than before. Moreover, it cannot compensate the complex phase changes around the frequencies of the resonances. To our experience, the servo bandwidth of the PZT servo loop is then limited to about 10 kHz. The phase margin at that frequency is about 80°.
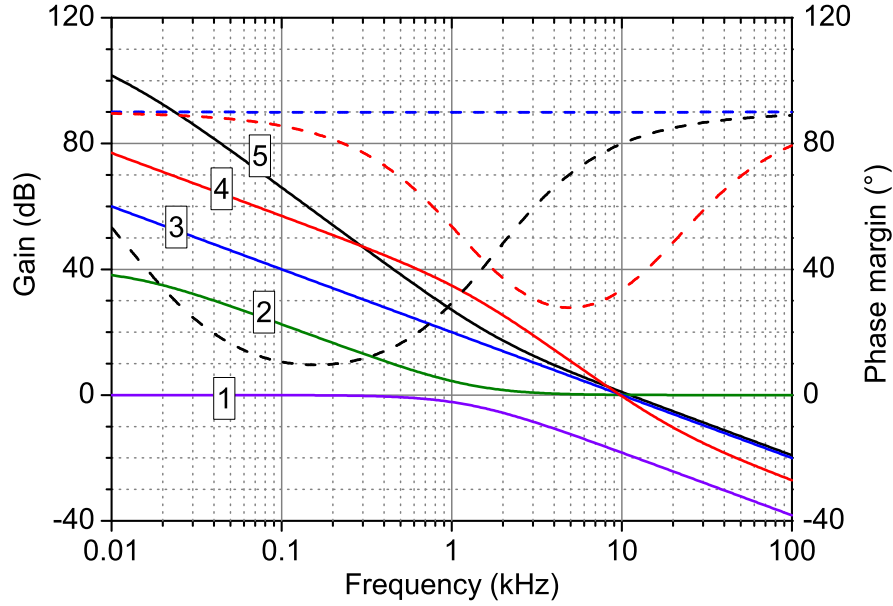
Figure 1.9: Calculated open-loop characteristics — gain (solid lines) and phase margin (dashed lines): (1) Lowpass, formed by resistor and PZT capacitance; (2) additional PI-circuit, used in the double-integrator; (3) Integrator, formed by lockbox with P-gain and lowpass; (4) same as (3), but with higher total gain and without P-gain; (5) double-integrator, same as (4), but with the additional PI-circuit (2). In this idealized picture, additional lowpass effects above 50 kHz are not considered.

Double integrator For the stability of the servo loop with respect to switching on and off the dipole trap, especially the low-frequency gain between 10 Hz and 100 Hz should be as high as possible. With the standard characteristic of an integrator of -20 dB/decade and a unity-gain (0 dB) frequency of 10 kHz, one could obtain a gain of 60 dB at 10 Hz, see Fig. 1.9 (3). When reducing the proportional gain such that the lockbox becomes an almost pure integrator, the lowpass is not compensated any more by the P-gain and one gets an additional slope of -20 dB/decade for $f \gtrsim 1$ kHz. One achieves a gain of almost 40 dB already at 1 kHz and almost 80 dB at 10 Hz, see Fig. 1.9 (4). However, this was still not sufficient to counteract the switching of the dipole trap reliably. Moreover, the phase margin at 10 kHz has significantly decreased, making the loop almost unstable. To increase the gain in the low-frequency range even more and improving the phase margin at 10 kHz at the same time, I integrated an additional PI-circuit into the lockbox right after its own PI-controller, see Fig. 1.10, box 'double-int.'. The gain of the additional PI-controller decreases with -20 dB/decade between approx. 13 Hz and 1.3 kHz, where it approaches unity, see Fig. 1.9 (2), and for details see [45]. To improve the phase margin at 10 kHz, I chose an intermediate P-gain setting of the lockbox. In total,
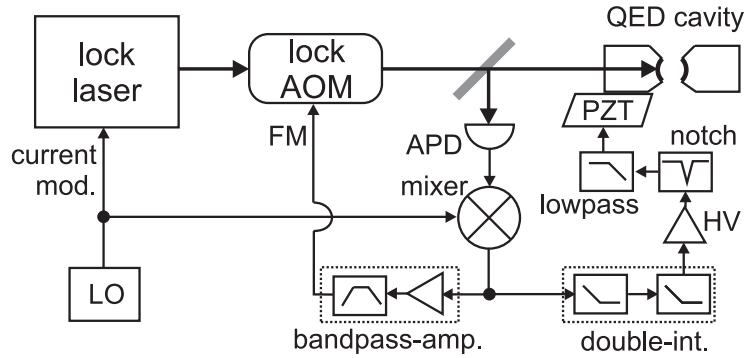
Figure 1.10: Final stage of the locking scheme in Fig. 1.6: The lock laser diode current is modulated with a frequency of about 50 MHz from a local oscillator (LO). The light is frequency-shifted by an AOM and then compared with the frequency of the QED cavity by the PDH method, using a beam splitter, a resonant avalanche photo diode (APD, [35]) and a mixer. The low-frequency components of the error signal are fed back on the cavity length via a double-integrator, HV-amplifier, filters and a shear-PZT element, while the high-frequency components are fed back on the laser frequency via a bandpass-amplifier and the FM input of the AOM.

one obtains $-40\,\mathrm{dB/decade}$ in the frequency range between about $10\,\mathrm{Hz}$ and $3\,\mathrm{kHz}$, see Fig. 1.9 (5) - a so called 'double-integrator' is formed in this range. The gain at $10\,\mathrm{Hz}$ could be increased by about $40\,\mathrm{dB}$. This has significantly improved the robustness of the servo loop, such that the cavity can better stand switching of the dipole trap and stay 'in lock' for hours.

Compensation laser   On the time scale of minutes to hours, the heating of the mirror substrates and the cavity holder by stray light or diffracted light from the dipole trap beams causes the cavity length to change by more than a wavelength and with it the cavity frequency by several free spectral ranges. This effect cannot be compensated by the shear-PZT alone. Moreover, to our experience, the high-frequency performance of the lock becomes better if the DC-offset voltage of the PZT is a low as possible. To counteract the long term drifts of the cavity length and to keep the PZT offset voltage close to zero, I integrated a fiber-coupled diode laser (compensation laser) into our setup. It is shone onto the cavity holder with a spot size of about $5\,\mathrm{mm}$ to heat it up. The power of up to $750\,\mathrm{mW}$ is controlled by another servo loop, for details see [7, 45].

Cross-lock   Concerning the high-frequency fluctuations between the lock laser and the cavity, causing intensity fluctuations inside the cavity, they cannot be sufficiently suppressed by the PZT servo loop due its bandwidth limit of about $10\,\mathrm{kHz}$. Two approaches have been realized: First, the high-frequency noise of the lock laser
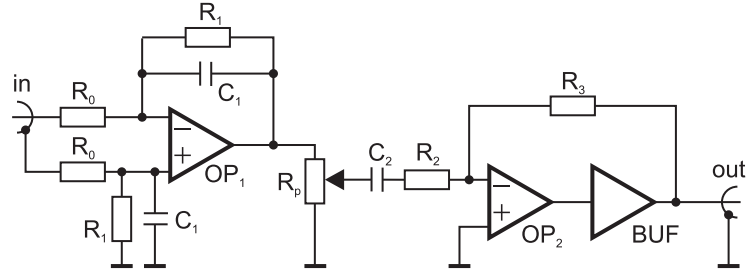
Figure 1.11: Electrical circuit of the bandpass-amplifier for the feedback of high frequencies on the laser frequency. The PDH error signal is applied to the input and then amplified in an inverted differential amplifier stage with lowpass characteristics. The output signal can be variably attenuated by R_p. Then it is AC-coupled to an inverted buffer amplifier, because the output is connected to the low-impedance FM input of the AOM.

could be drastically reduced, increasing the lifetime of atoms inside the resonator (without probe laser) from (18 ± 3) ms to (130 ± 18) ms [45]. Second, I implemented a so-called cross-lock: In addition to the low-frequency feedback on the cavity length via the double-integrator and the PZT, the high frequency components of the error signal are fed back on the lock laser frequency via a bandpass-amplifier and an AOM, see Fig. 1.10.

The electrical circuit of the bandpass-amplifier is shown in Fig. 1.11. The first stage is an inverting differential amplifier (insensitive to ground loops) with integrated lowpass, formed by the resistors $R_0 = 1\,\mathrm{k\Omega}$, $R_1 = 33\,\mathrm{k\Omega}$, the capacitors $C_1 = 2.7\,\mathrm{nF}$ and the operational amplifier OP_1 (model OP27). The PDH error signal is amplified by a factor of $-R_1/R_0 = -33$ or 30 dB with an upper cutoff frequency of $1/(2\pi R_1 C_1) = 1.8\,\mathrm{kHz}$. After having passed a variable voltage divider (poti) with $R_\mathrm{p} = 4.7\,\mathrm{k\Omega}$, the signal is capacitively coupled by $C_2 = 1\,\mathrm{\mu F}$ to another inverting buffer amplifier[4], formed by the resistors $R_2 = R_3 = 10\,\mathrm{k\Omega}$, the operational amplifier OP_2 (model OP27) and the buffer amplifier BUF (model BUF634), to drive the low-impedance ($50\,\Omega$) FM input of the AOM. The capacitor C_2 and the resistors R_2, R_p form a highpass with a lower cutoff frequency of about 10 Hz.

The typical open-loop gain of this bandpass-amplifier in combination with the AOM is about 30 dB, see Fig. 1.12. The total loop gain of the cross-lock is the vectorial sum of the double-integrator gain and the bandpass-amplifier gain. For this specific settings, the two curves intersect at a frequency of about 1 kHz. The different phases lead to a partially destructive interference, causing a small local minimum of the total gain. Here, the two branches of the feedback loop not only counteract the outer disturbances but also counteract each other. However, due to the increased phase margin at 10 kHz, the total gain could be improved with respect

---

[4]other control voltages for the AOM frequency are applied between R_2 and R_3 and added to the output signal (not shown).
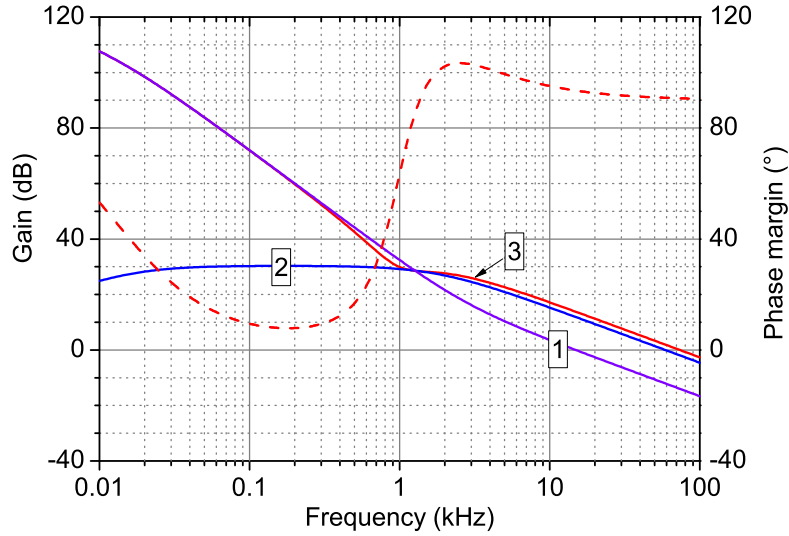
Figure 1.12: Calculated total open-loop gain (3) and phase margin (dashed line) of the cross-lock as the vectorial sum of the gain of the double-integrator (1) and the bandpass-amplifier (2). At the intersection, they interfere partially destructively because of different phases.

to the PZT servo loop, shifting the servo bandwidth to even higher frequencies.

When locking the QED cavity, the gain of the bandpass-amplifier has to be adjusted such that the root-mean-square (rms) noise of the error signal and with it the fluctuations of the lock laser transmission through the cavity are minimized.

Result After all these improvements of the lock chain for the QED cavity, the rms fluctuations of the frequency difference between the lock laser and the cavity could be reduced from $100 - 150$ kHz [44] to $30 - 40$ kHz. Frequency fluctuations around the resonance between lock laser and QED cavity translate into intensity fluctuations to first order quadratically. Therefore, this corresponds to a reduction of the relative intensity fluctuations by almost one order of magnitude. Today, an average lifetime of atoms inside the resonator of (0.7 ± 0.1) s is achieved, see chapter 5. Exploiting also cavity-cooling effects, we are routinely able to observe a single atom inside the cavity for several seconds.

1.3 Coherently driving the atoms

The precision of atomic clocks and the formal definition of the second relies on the fact that the transition between the two hyperfine levels $|F = 3\rangle$ and $|F = 4\rangle$ of the $6^2\mathrm{S}_{1/2}$ ground state in cesium is extremely narrow [40]. A coherent superposition of the two states can thus survive for relatively long times. Therefore, they are hot

Figure 1.13: Relevant levels of the cesium D_2-transition for coherent two-photon Raman transitions between the two ground states. The laser frequencies ω_{pump} and ω_{Stokes} are far detuned by $\Delta_{\mathrm{R}} \gg \Gamma$ from the atomic resonance frequencies.
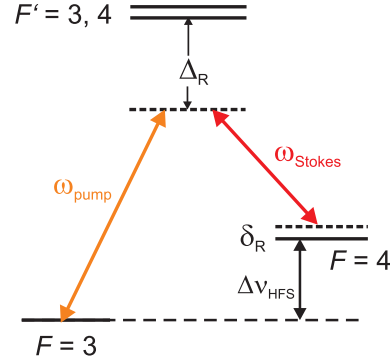
candidates to serve as qubit states in quantum information processing[5].

Coherent superpositions of the two states can be directly prepared by exposing the atoms to a magnetic field that varies in time with a frequency $\Delta\nu_{\mathrm{HFS}} = 9.2\,\mathrm{GHz}$ corresponding to their energy splitting $\Delta E_{\mathrm{HFS}} = h\Delta\nu_{\mathrm{HFS}}$. The spin dynamics can be described analogous to nuclear magnetic resonance (NMR) experiments by optical Bloch equations [2].

In our experiment, we expose the atoms to microwave radiation and the atoms couple to its time-dependent magnetic field. In this way, coherent superpositions of two Zeeman sublevels, e.g. of $|F = 3, m_F = 0\rangle$ and $|F = 4, m_F = 0\rangle$ can be prepared and the hyperfine state can be detected with high efficiency by a push-out technique [40, 60]. The latter is the selective removal of all atoms in the hyperfine state $|F = 4\rangle$ from the dipole trap by exposing them to a laser beam which is resonant with the $|F = 4\rangle \leftrightarrow |F' = 5\rangle$ transition. Moreover, by using the magnetic-field sensitive Zeeman states $|F = 3, m_F = 3\rangle$ and $|F = 4, m_F = 4\rangle$, the resonance frequency can be made position-dependent by applying a static magnetic field gradient along the trap axis. In this way, we are able to selectively address and manipulate single qubits out of a row [39, 61].

1.3.1 Raman transitions

An alternative way to drive coherent transitions between the two hyperfine ground states is to couple them via a two-photon Raman process [14]. Two laser fields, a so-called pump field and a Stokes field, drive electric dipole transitions between each ground state and a common excited state, e.g. $|F' = 3\rangle$ or $|F' = 4\rangle$. To avoid spontaneous photon scattering that can destroy the coherence of a ground state superposition, the lasers are typically far detuned from the atomic transition frequencies, i.e. with a single-photon detuning Δ_{R} that is much larger than the atomic linewidth Γ, see Fig. 1.13. In this limit, the excited hyperfine states are only virtually excited. A transition between the two ground states occurs then by the simultaneous stimulated absorption and emission of a photon, e.g., absorption from the pump field and emission into the Stokes field.

---

[5]More precisely, one would select two Zeeman sublevels of the hyperfine states.

As in the microwave case, the system can be regarded as a driven, effective two-level system. Although they are effectively very similar to microwave transitions when applied for qubit manipulation, Raman transitions have some more applications due to the fact that photons at optical frequencies are involved. Since they carry a much higher momentum than microwave photons, there can be a significant momentum transfer between atoms and photons depending on the angle between the two laser beams. This can be exploited for the coherent control of the motion of the atoms and for sub-Doppler cooling schemes, see chapter 5. Moreover, a Raman scheme can be combined with cavity QED by replacing one laser field with the quantized field of an optical cavity. In this way, one can transfer a coherent superposition between ground states to the cavity field and back [62] or one can realize deterministic single-photon sources [63, 64]. The coupling of two atom to the cavity field could be used to create entanglement of the atomic ground states in a deterministic way [65].

Simple model

The effective coupling of the two levels with Raman lasers that are far-detuned from the optical transition frequencies can be quantified by the Raman-Rabi frequency [66]

$$\Omega_{\mathrm{R}} = \frac{\Omega_{\mathrm{pump}}\, \Omega_{\mathrm{Stokes}}}{2\Delta_{\mathrm{R}}} \,, \tag{1.12}$$

where Ω_{pump} and Ω_{Stokes} are the single-photon Rabi frequencies of the optical transitions. A Rabi frequency for a transition $|g\rangle \leftrightarrow |e\rangle$ is defined via the corresponding dipole matrix element

$$\Omega_{\mathrm{ge}} = \frac{\langle e|\hat{\vec{d}} \cdot \vec{E}|g\rangle}{\hbar} \,, \tag{1.13}$$

where $\hat{\vec{d}}$ denotes the electric dipole operator and $\vec{E}$ the electric field. Atomic population oscillates between the two ground states with the angular frequency $\Omega_{\mathrm{R}}/2$ between the two states if the Raman two-photon detuning

$$\delta_{\mathrm{R}} \equiv (\omega_{\mathrm{pump}} - \omega_{\mathrm{Stokes}}) - 2\pi\Delta\nu_{\mathrm{HFS}} \tag{1.14}$$

vanishes, i.e. in the two-photon Raman resonance case. Here, ω_{pump} and ω_{Stokes} are the angular frequencies of the pump and the Stokes laser, respectively.

In the general case ($\delta_{\mathrm{R}} \neq 0$), the probability to find a system that is prepared in state $|F=3\rangle$ at $t=0$ in state $|F=4\rangle$ at a time t is given by

$$P_4(t) = \Lambda \sin^2\left(\frac{\Omega}{2}\,t\right) \,, \tag{1.15}$$

$$\text{where} \quad \Lambda = \frac{\Omega_{\mathrm{R}}^2}{\Omega_{\mathrm{R}}^2 + \delta_{\mathrm{R}}^2} \quad \text{and} \quad \Omega = \sqrt{\Omega_{\mathrm{R}}^2 + \delta_{\mathrm{R}}^2} \tag{1.16}$$

are the contrast and effective Raman-Rabi frequency, respectively.

1.3.2 Raman laser setup

The first implementation of Raman transitions in our setup was based on a single diode laser in combination with an electro-optic modulator (EOM) [67]. The latter was used to modulate the phase of the laser beam such that sidebands in frequency space at about $\pm\Delta\nu_{\mathrm{HFS}}$ with respect to the laser frequency are generated. It is technically challenging to separate the different frequency components by interferometric means [68] to avoid destructive interference between them.

The current Raman laser setup consists of two individual lasers, which are optically phase locked with respect to each other at a frequency difference of about $\Delta\nu_{\mathrm{HFS}}$. The main advantages are that the two laser beams can be separated much more easily and that almost the entire power of each laser is available for the pump and the Stokes transition, respectively. However, in contrast to the single-laser setup, the relative phase stability between the two lasers is not only determined by the reference radio frequency source (providing the $9.2\,\mathrm{GHz}$) but also by the performance of the servo loop. It took two Diplom theses until the lasers and the optically phase locked loop (OPLL) were sufficiently stable and Raman transitions could be successfully demonstrated with this setup [46, 48]. Now, the Raman laser setup is a powerful and reliable tool. In particular, it forms the basis for the measurements of EIT inside the cavity, for details see chapter 4.

1.3.3 Raman transitions in the dipole trap

The first measurements that have been performed using our current Raman setup are the spectroscopy of Zeeman sublevels, the demonstration of optical pumping to a specific Zeeman sublevel and Rabi oscillations. Here, I will give a brief overview of the results, for more details see [48].

The two Raman laser beams (the pump and the Stokes beam) propagate collinearly and are spatially overlapped with the optical dipole trap. The circularly polarized beams have an $1/e^2$ waist of $w_{\mathrm{con,MOT}} = 103\,\mu\mathrm{m}$ at the MOT position and a waist of $w_{\mathrm{con,MOT}} = 86\,\mu\mathrm{m}$ at the cavity position, which is significantly larger than the waists of the dipole trap at those positions (about $40\,\mu\mathrm{m}$). This ensures that the atoms trapped in the dipole trap see an almost constant intensity.

In this configuration, two types of Raman transitions can be driven between Zeeman sublevels of the hyperfine ground states, see Fig. 1.14. The degeneracy of Zeeman sublevels is lifted by applying a magnetic guiding field. The selection rules for Raman transition depend on the angle between the Raman laser beams and the magnetic field lines: If the angle is zero, both Raman beams drive either σ^- or σ^+ transitions. This gives either a (σ^-,σ^-) or a (σ^+,σ^+) Raman transition (only the first one is shown). The magnetic quantum number m_F of the initial and final Zeeman sublevel will thus not change — only transitions with $\Delta m_F = 0$ are allowed. If the magnetic field is perpendicular to the beam axis, both Raman beams drive a mixture of σ^+, σ^- and π transitions. Out of several possible combinations, only the superposition of (π,σ^-) and (σ^+,π) Raman transitions interferes constructively, i.e.
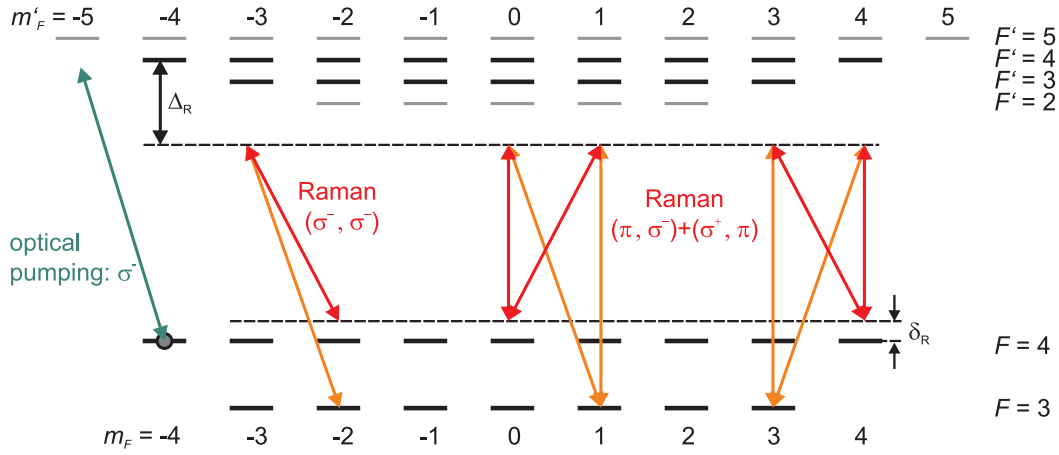
Figure 1.14: Cesium level scheme with all Zeeman sublevels of the D_2 transition and the possible Raman couplings between the ground-state m_F sublevels. (σ^-, σ^-) transitions can be driven if the magnetic field lines are parallel to the circularly polarized Raman laser beams, while in the perpendicular case, superpositions of (π, σ^-) and (σ^+, π) can be driven. A circularly polarized optical pumping beam resonant with the $|F = 4\rangle \leftrightarrow |F' = 4\rangle$ transitions can be applied to prepare atoms in, e.g. $|F = 4, m_F = -4\rangle$.

the magnetic quantum number has to change by $\Delta m_F = \pm 1$.

A typical Raman spectrum is shown in Fig. 1.15 (a). After atoms are loaded from the MOT into the DT, they are are all prepared in the hyperfine state $|F = 4\rangle$ by exposing the atoms to the repumping beam longer than to the cooling laser beams of the MOT. A magnetic guiding field with $|B| = 0.4\,\text{G}$ is then applied along the z-direction, shifting the transition frequencies between the outermost Zeeman sublevels $|3, \pm 3\rangle$ and $|4, \pm 4\rangle$ by about $\pm 1\,\text{MHz}$. Raman pulses with a fixed duration of $20\,\mu\text{s}$ and a total power of $600\,\mu\text{W}$, and a single-photon detuning of $\Delta_\text{R}/2\pi = 320\,\text{GHz}$ are applied with variable δ_R. At the end of the sequence, the fraction of atoms that have been transferred to $|F = 3\rangle$ is measured by the push-out technique. The spectrum exhibits eight peaks in the range $\delta_\text{R}/2\pi \approx (-1 \ldots 1)\,\text{MHz}$, corresponding to all 14 possible transitions with $\Delta m_F = \pm 1$, twelve of which are pairwise degenerate: $2 + 12/2 = 8$.

Efficient optical pumping to the outermost Zeeman sublevel $|F = 4, m_F = -4\rangle$ can be performed with by exposing the atoms to a circularly polarized laser beam resonant with the $|F = 4\rangle \leftrightarrow |F' = 4\rangle$ transition in addition to the repumper. If the magnetic field is parallel to the optical pumping beam, only σ^- transitions are driven. After a few milliseconds, the atoms will end up in the 'dark' state $|F = 4, m_F = -4\rangle$. The effect is clearly visible in a Raman spectrum, see Fig. 1.15 (a): There is only a single peak at $\delta_\text{R}/2\pi \approx -1\,\text{MHz}$, corresponding to the $|4, -4\rangle \leftrightarrow |3, -3\rangle$ Raman transition.

Having prepared the atoms in the $|F = 4, m_F = -4\rangle$ sublevel, we can now drive

(a)

(b)
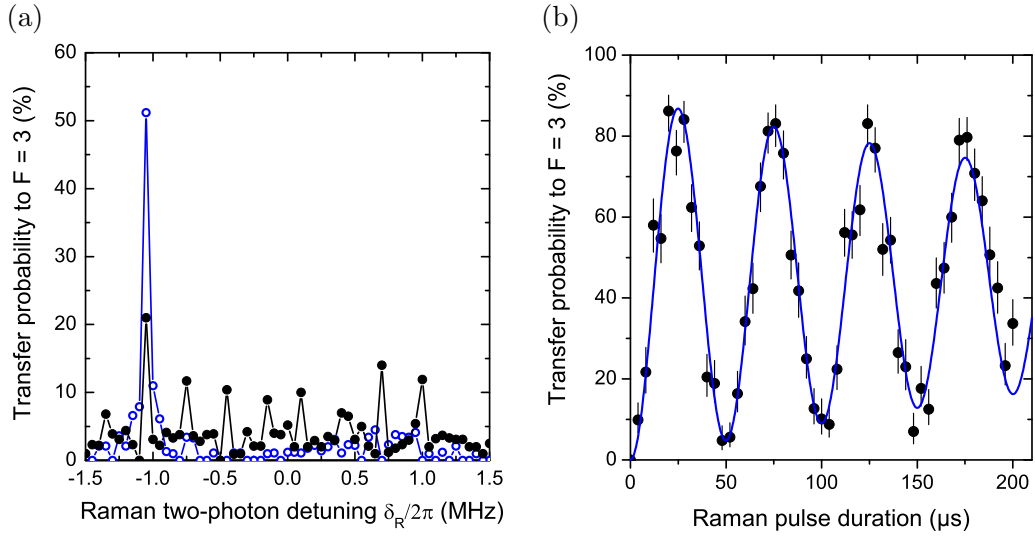
Figure 1.15: (a) Raman spectra taken with the magnetic field perpendicular to the
Raman beams. *Full circles*: Atoms are prepared in $|F = 4\rangle$ without optical
m_F pumping before the Raman pulse . Since the atoms are distributed over
the Zeeman sublevels, 14 transitions can occur resulting in the eight peaks.
Open circles: Atoms are optically pumped to the outermost Zeeman sublevel
$|F = 4, m_F = -4\rangle$ before the Raman pulse. The spectrum has only a single
peak, corresponding to the $|4, -4\rangle \leftrightarrow |3, -3\rangle$ transition. (b) Raman Rabi
oscillations on the $|4, -4\rangle \leftrightarrow |3, -3\rangle$ transition, with an exponentially damped
sinusoidal fit function (solid line).

the $|4, -4\rangle \leftrightarrow |3, -3\rangle$ transition resonantly, i.e. at $\delta_R/2\pi \approx -1\,\text{MHz}$. Here, the
total laser power is $1000\,\mu\text{W}$ and the single-photon detuning is $\Delta_R/2\pi = 169\,\text{GHz}$,
but this should only affect the Raman Rabi frequency. To observe Raman Rabi
oscillations, we measure the population in the state $|F = 3\rangle$ as a function of the
duration t of the Raman pulse, see Fig. 1.15 (b). The data can be fitted with an
exponentially damped sinusoidal function with a Rabi frequency of about $20\,\text{kHz}$
and a damping time constant of about $400\,\mu\text{s}$, related to dephasing effects. For a
detailed discussion, see [48].

2 Coherently driven atom under continuous observation

2.1 Introduction

In the last chapter I have shown that the transmission of our high-finesse optical cavity sensitively depends on the position of a single atom, see section 1.2.1. In addition to this external atomic state, the cavity transmission is strongly related to the internal hyperfine state of the atom: If we tune, e.g., the cavity frequency close to the transition frequency between the $|F = 4\rangle$ ground state and the $|F' = 5\rangle$ excited state [Fig. 1.3 (a)], the transmission of the probe beam is strongly suppressed and the atom is in state $|F = 4\rangle$. In contrast, an atom in $|F = 3\rangle$ has a negligible effect on the cavity transmission since all possible transitions between $|F = 3\rangle$ and the $|F' = 2, 3, 4\rangle$ excited state are far detuned from the cavity frequency. The atomic state can thus be deduced from the number of transmitted photons per time interval [9], see Fig. 2.1. These histograms of the photon counts per binning time interval almost don't overlap for the chosen binning time.

In contrast to the state detection method with a push-out laser which relies on the state-selective removal of atoms from the trap, this is a non-destructive state detection method where one-and-the-same atom can be used for many successive state measurements. In the ideal case, the cavity transmission measurement would projects the atomic state onto one of the two hyperfine ground states $|F = 3\rangle$ and $|F = 4\rangle$, and every subsequent repetition of the state measurement would have the same outcome. This represents a projective quantum-non-demolition (QND) measurement [69] of the internal atomic state. With more than one atom inside
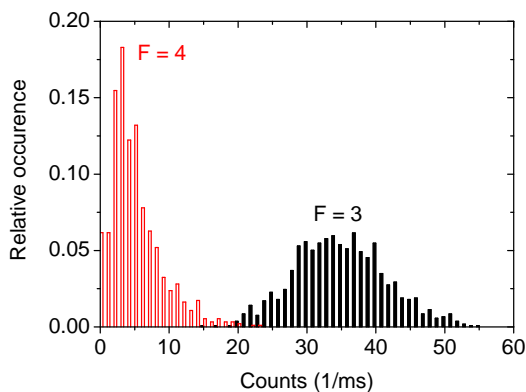

Figure 2.1: Histograms of the number of detected probe photons which are transmitted through the cavity within a time interval of $1\,\mathrm{ms}$. If one atom in state $|F = 4\rangle$ is inside the cavity mode, the mean number of detection events is about eight times lower than for the state $|F = 3\rangle$, corresponding to the empty-cavity case.
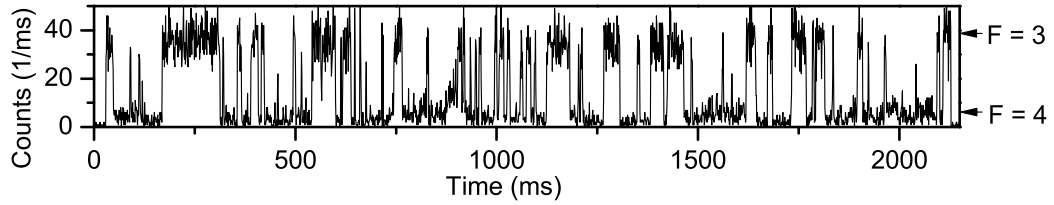
Figure 2.2: Random telegraph signal with a single atom inside the cavity. The transmission of the probe beam through the resonator changes randomly with time between two levels, indicating quantum jumps of the atomic hyperfine ground state. While the probe laser causes transitions from $|F = 4\rangle$ to $|F = 3\rangle$, a weak repumping laser resonant with the $|F = 3\rangle \leftrightarrow |F' = 4\rangle$ transition induces jumps in the other direction.

the cavity, this could be employed to create multi-atom entangled states [70].

However, continuous observation of the cavity transmission reveals quantum jumps [12]. They have also been observed in single-ion experiments [71, 72] or with single photons stored in a cavity [73]. In our case, quantum jumps are sudden changes of the hyperfine ground state. They are caused by inelastic Raman scattering events of atoms in $|F = 4\rangle$, resulting from off-resonant excitation of the states $|F' = 3, 4\rangle$ by the probe laser light with subsequent decay to $|F = 3\rangle$. This unwanted side effect reduces the fidelity of our state detection, since the hyperfine state can change during our detection interval. With a relatively weak repumping laser on the $|F = 3\rangle \leftrightarrow |F' = 4\rangle$ transition, quantum jumps can be deliberately induced also in the other direction [12], resulting in so-called random telegraph signals, see Fig. 2.2.

This incoherent dynamics of the hyperfine states, relying on spontaneous photon scattering, has extensively been studied in our system using one and two atoms [13, 47]. Our experimental data which contains noise is processed in an optimal way using Bayesian data analysis [13, 74]. First steps towards quantum feedback [75, 76], e.g. the stabilization of an entangled multi-atom state with a control loop, have been demonstrated, however, making use of probabilistic, uni-directional scattering processes [49].

Here, we drive the hyperfine dynamics by coupling the two ground states via a two-photon Raman process, see section 1.3.3. First, a coherently driven system under continuous observation is of general fundamental interest, since it reveals the impact of the measurement on the quantum state of a system. The Quantum Zeno effect (QZE) [15–19] can 'freeze' the coherent evolution from one state of the system to the other one by projecting the system always back onto the initial state, due to the measurement. Second, bi-directional transitions can be selectively induced by controlling the two-photon detuning δ_R and the intensity of the Raman beams. When a magnetic field is applied, the degeneracy of the Zeeman-sublevels of the hyperfine states is lifted and the Raman transitions even become m_F-selective.

Moreover, the polarization of the laser beams with respect to the magnetic field direction determines the selection rules for the transitions. This gives rise to a new method of spectroscopy, where the hyperfine dynamics of a single atom is coherently driven by a Raman transition while the transmission through the cavity, i.e. the quantum jumps, are continuously observed. The spectroscopy provides an in-situ diagnostics the internal dynamics of a single atom inside the cavity, e.g. to study effects of optical pumping in our system [38].

After a brief introduction into the QZE, I will present the method of quantum jump spectroscopy. For this, I extend our Bayesian update formalism to analyze data with time-dependent rates, and finally, I demonstrate its application in our setup.

2.2 Quantum Zeno effect

We wonder how the rate of quantum jumps in a spectroscopy experiment would be related to the Rabi frequency Ω_R and detuning δ_R of the coherent drive while the system is continuously measured at a rate Γ_m. The basic scaling of the transition probability with those parameters is provided by a simple and intuitive picture of the Quantum Zeno effect: Let us consider a two-state system which is prepared in state $|0\rangle$ at $t = 0$ and coherently driven by a microwave or Raman transition with resonant Rabi frequency Ω_R and detuning δ_R. The probability to find the system in state $|1\rangle$ at a time t is given by

$$P_1(t) = \Lambda \sin^2\left(\frac{\Omega}{2}t\right), \quad \text{where} \tag{2.1}$$

$$\Lambda = \frac{\Omega_R^2}{\Omega_R^2 + \delta_R^2} \quad \text{and} \quad \Omega = \sqrt{\Omega_R^2 + \delta_R^2} \tag{2.2}$$

are the contrast and effective Rabi frequency of the oscillations, see Fig. 2.3. First, I consider the case that the state of the system is repeatedly measured with pulses, spaced by fixed, short time intervals $\Delta t_p \ll 1/\Omega$, which project the system each time into one of its eigenstates $|0\rangle$ or $|1\rangle$, and re-initialize the system. The probability that the system is still in the initial state $|0\rangle$ after Δt_p is $1 - P_1(\Delta t_p) \approx 1 - \Lambda(\Omega\Delta t_p/2)^2$ and after $N \gg 1$ successive measurements or a time $T = N\Delta t_p$ [77–79]

$$P(T) \approx \left[1 - \Lambda\left(\frac{\Omega}{2}\Delta t_p\right)^2\right]^N \approx \exp\left[-N\Lambda\left(\frac{\Omega}{2}\Delta t_p\right)^2\right] = \exp\left[-\frac{\Lambda\Omega^2\Delta t_p}{4}T\right]. \tag{2.3}$$

There are obviously no Rabi-type oscillations between the two states but an effective 'decay' of the initial state $|0\rangle$ into state $|1\rangle$ [77–79] at rate

$$R_{01,p} = \frac{\Lambda\Omega^2\Delta t_p}{4} = \frac{\Omega_R^2\Delta t_p}{4}. \tag{2.4}$$
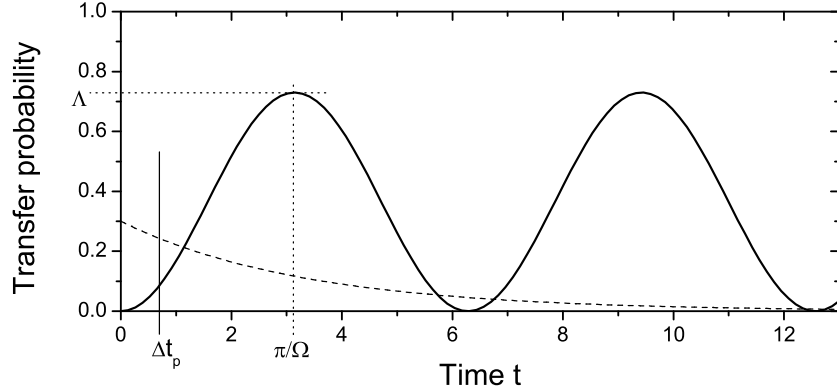
Figure 2.3: Solid line: probability $P_1(t)$ of a coherently driven two-level system that is prepared in state $|0\rangle$ at time $t = 0$ to be measured in state $|1\rangle$ after a time t. In the pulsed case, the measurement occurs after a fixed time Δt_p (narrow peak). In the random case, the measurement events are exponentially distributed (dashed line).

The shorter and thus more frequent the probing intervals Δt_p are, the smaller is the decay rate and the slower is the evolution of the system. I note that R_{01} is independent of the detuning δ_R as long as $\Delta t_\mathrm{p} \ll (1/\Omega_\mathrm{R}, 1/\delta_\mathrm{R})$. However, for large detunings $\delta_\mathrm{R} \gg (1/\Delta t_\mathrm{p}, \Omega_\mathrm{R})$, this condition is no longer fulfilled and the quadratic approximation used in Eqn. (2.3) is not justified any more. Moreover, in the limit of random and arbitrary long probing intervals $\Delta t_\mathrm{p} \gg 1/\Omega$, the mean probability to find the system in state $|1\rangle$ is $\langle P_1 \rangle = \Lambda/2 \propto 1/\delta_\mathrm{R}^2$.

When the system is probed continuously, e.g. with coherent light, where each photon projects the state of the system in an eigenstate, one can model this process by a series of random, temporally uncorrelated measurement pulses with an average spacing of $1/\Gamma_\mathrm{m}$. In contrast to equally spaced pulses with fixed interval, the distribution of the time between the pulses is described by an exponential probability density function, see Fig. 2.3:

$$P_\mathrm{m}(t)\mathrm{d}t = \Gamma_\mathrm{m} \exp(-\Gamma_\mathrm{m} t)\mathrm{d}t \qquad (2.5)$$

is the probability of no measurement pulse, e.g. coherent evolution, during $[0, t[$ and a measurement pulse during $[t, t + \mathrm{d}t]$. The probability that the system has changed its state when a measurement occurs is thus given by

$$P_{1,\mathrm{m}} = \int_0^\infty P_1(t) P_\mathrm{m}(t)\mathrm{d}t = \Gamma_\mathrm{m}\Lambda \int_0^\infty \sin^2\left(\frac{\Omega}{2}t\right) \exp(-\Gamma_\mathrm{m} t)\mathrm{d}t \qquad (2.6)$$

$$= \frac{\Omega_\mathrm{R}^2}{2(\Gamma_\mathrm{m}^2 + \Omega_\mathrm{R}^2 + \delta_\mathrm{R}^2)} \qquad (2.7)$$

and thus the state-changing rate reads

$$R_{01,\mathrm{r}} = \Gamma_\mathrm{m} P_{1,\mathrm{m}} = \frac{\Gamma_\mathrm{m} \Omega_\mathrm{R}^2}{2(\Gamma_\mathrm{m}^2 + \Omega_\mathrm{R}^2 + \delta_\mathrm{R}^2)} \, . \tag{2.8}$$

For strong probing ($\Gamma_\mathrm{m} \gg \Omega_\mathrm{R}$), I obtain

$$R_{01,\mathrm{r}} = \frac{\Omega_\mathrm{R}^2}{2\Gamma_\mathrm{m}} \times \frac{1}{1 + (\delta_\mathrm{R}/\Gamma_\mathrm{m})^2} \, , \tag{2.9}$$

a Lorentzian function with a full-width-at-half-maximum (FWHM) of $2\Gamma_\mathrm{m}$. The maximum value $\Omega_\mathrm{R}^2/(2\Gamma_\mathrm{m})$ at $\delta_\mathrm{R} = 0$ equals the rate obtained for equally spaced pulses if $\Gamma_\mathrm{m} = 2/\Delta t_\mathrm{p}$, cf. [79]. However, modelling a continuous measurement by randomly spaced measurement pulses is only a rough approximation. It should provide an intuitive picture and the orders of magnitude transition rates and their dependence on detuning. An exact treatment would require to include the continuous measurement rate Γ_m as a decoherence rate into the quantum dynamics of the system [19,78]. For instance, the resonant ($\delta_\mathrm{R} = 0$) state-changing rate in the presence of continuous strong measurement by a coherent laser beam $R_{01,\mathrm{c}} = \Omega_\mathrm{R}^2/\Gamma_\mathrm{m}$ is twice as large as for the random pulse measurement case [79].

2.2.1 QZE within a cavity

An ideal cavity in the strong-coupling regime $g^2 \gg (\kappa, \gamma)$ can be tuned such that it either completely transmits or reflects the probe light impinging on its input mirror, depending on the hyperfine ground state of the atom. A photon detected in the transmitted mode would, e.g., project the atomic state into $|0\rangle = |F = 3\rangle$, while a reflected photon would project it into $|1\rangle = |F = 4\rangle$. The photon output rate from *one* mirror is thus to the rate at which the system is measured [19]

$$\Gamma_\mathrm{m} = \kappa n_{\mathrm{p},0} \, , \tag{2.10}$$

where $n_{\mathrm{p},0}$ denotes the intra-cavity photon number of the empty cavity on resonance with the probe laser.

In the realistic case of a non-ideal cavity there are absorption or scattering losses in the mirror coatings. On one hand, a fraction of the impinging light will always be reflected at the input mirror even if there's no atom inside. This doesn't change the situation because this fraction does not contain any information about the atomic state and therefore does not contribute to the measurement rate. On the other hand, one considers the fraction that is coupled into the cavity mode. Then, it also doesn't matter for the decoherence whether it leaves the cavity by transmission, absorption or scattering into other spatial modes. All effects are subsumed in κ. Therefore, Eqn. (2.10) is also valid for a non-ideal cavity [19].

2.3 Quantum jump spectroscopy with Bayesian update

The basic idea of quantum jump spectroscopy is to measure the coherently induced transition rates between two long-lived atomic states by observing the frequency of quantum jumps in the transmission of a weak probe laser through the cavity. By sweeping the detuning δ_{R} of the coherent coupling from the transition frequency between the two states, the rates may change with time and with it the frequency of quantum jumps. The spectrum is thus given by the rates R_{01} and R_{10} between the atomic hyperfine states $|0\rangle$ and $|1\rangle$ as a function of the detuning δ_{R}.

2.3.1 Bayesian update algorithm

The atomic state and the rates can be extracted from the random telegraph signals using a Bayesian update algorithm [38,47,49]: From the Bayesian point of view, the knowledge of our system in terms of the atomic state $|\alpha\rangle$ and the transition rates R_{01}, R_{10} is represented by a probability distribution $0 \leq p(\alpha, R_{01}, R_{10}) \leq 1$. Perfect knowledge of the system would mean that there exists a set of values $(\alpha', R'_{01}, R'_{10})$ such that

$$p(\alpha, R_{01}, R_{10}) = \begin{cases} 1 & \text{if} \quad (\alpha, R_{01}, R_{10}) = (\alpha', R'_{01}, R'_{10}), \\ 0 & \text{otherwise.} \end{cases} \tag{2.11}$$

On the other hand, a flat distribution with equally small entries corresponds to an almost complete ignorance of the system, as is usually the case before experimental data in terms of the recorded photon clicks are taken. So how can one get from a flat to a peaked distribution, i.e. how can one improve (update) the knowledge with more and more data being taken?

First of all, we seperately measure the probability distribution $p(n|\alpha)$ that n photon clicks are recorded during an observation time interval (time bin, here: $\Delta t_{\mathrm{bin}} = 1\,\mathrm{ms}$) with the atom being in a known, prepared state $|\alpha\rangle$, see Fig. 2.1. For the state $|0\rangle = |F = 3\rangle$, we record just the transmission of a probe beam through the cavity without any atom inside. For the other state, we place one atom inside the cavity and apply a strong repumping laser on the $|F = 3\rangle \leftrightarrow |F' = 4\rangle$ transition to pump atoms which are eventually in $|F = 3\rangle$ back to $|F = 4\rangle$. While for the state $|0\rangle$, the count rate distribution can be well described by a Poissonian distribution with an a mean number of clicks $n_{\mathrm{c},0} = 34.0$, the other distribution with $n_{\mathrm{c},1} = 4.3$ is significantly broader than a Poissonian with the corresponding mean value. This is due to fluctuations of the transmission in this state which can be attributed to a time-varying coupling strength $g(t)$ [38,47].

State update without dynamics

Regardless of our knowledge of the rates R_{01}, R_{10}, one can already gain some knowledge about the atomic state $|\alpha\rangle$ when n photons have been detected in a time bin

by means of Bayes' theorem:

$$p_{\text{post}}(\alpha) = \frac{p(n|\alpha)\,p_{\text{pri}}(\alpha)}{\sum_{\alpha'} p(n|\alpha')\,p_{\text{pri}}(\alpha')}\,, \qquad (2.12)$$

where $p_{\text{post}}(\alpha)$ denotes the *a-posteriori*-probability of the atom to be in state $|\alpha\rangle$, depending on the *a-priori*-probability $p_{\text{pri}}(\alpha)$, which represents our previous knowledge just before the update. In particular, if one has no previous knowledge about the state: $p_{\text{pri}}(0) = p_{\text{pri}}(1) = 1/2$. After one has updated the knowledge according to Eqn. (2.12) with the data of one time bin, one can use $p_{\text{post}}(\alpha)$ as the new *a-priori*-probabilities $p_{\text{pri}}(\alpha)$ for the next time bin and and apply Eqn. (2.12) again. With more and more time bins taken into account, the probabilities would approach 0 or 1, respectively, expressing our full knowledge of the atomic state.

State update including dynamics

However, if one takes into account the temporal dynamics of the atomic state, the updated probabilities will change during the next observation time interval, i.e. before the next update will occur. The *a-priori*-probabilities $p_{\text{pri}}(\alpha)$ right before the next update will thus be different from the *a-posteriori*-probabilities $p_{\text{post}}(\alpha)$ after the last update. The dynamics of the state probabilities can be modelled by a system of rate equations

$$\frac{\mathrm{d}}{\mathrm{d}t}\vec{p}(t) = \begin{pmatrix} -R_{01} & R_{10} \\ R_{01} & -R_{10} \end{pmatrix} \vec{p}(t)\,, \quad \text{where} \quad \vec{p}(t) \equiv \begin{pmatrix} p(\alpha=0,t) \\ p(\alpha=1,t) \end{pmatrix}. \qquad (2.13)$$

For time bins that are much shorter than the evolution of the system governed by the rates, i.e. $\Delta t_{\text{bin}} \ll (1/R_{01}, 1/R_{10})$, one can give a linear approximation of the solution

$$\vec{p}(t + \Delta t_{\text{bin}}) = \vec{p}(t) + \Delta t_{\text{bin}} \begin{pmatrix} -R_{01} & R_{10} \\ R_{01} & -R_{10} \end{pmatrix} \vec{p}(t)\,. \qquad (2.14)$$

Before each new state update according to Eqn. (2.12), one uses Eqn. (2.14) to obtain $p_{\text{pri}}(\alpha) = p(\alpha, t + \Delta t_{\text{bin}})$ from the latest $p(\alpha, t) = p_{\text{post}}(\alpha)$.

Update of time-dependent states and constant rates

If the rates R_{01}, R_{10} are not known before but should also be determined using the update formalism, one needs an update formalism for the combined probabilities $p(\alpha, R_{01}, R_{10})$ of the atomic states and the rates [49]. Applying the general rule for combined probabilities $p(a, b) = p(a|b)\,p(b)$, they can be separated as follows:

$$p(\alpha, R_{01}, R_{10}) = p(\alpha|R_{01}, R_{10})\,p(R_{01}, R_{10})\,, \qquad (2.15)$$

where $p(\alpha|R_{01}, R_{10})$ is the probability for state $|\alpha\rangle$ under the assumption of the rates R_{01}, R_{10}. This term evolves in time according to Eqn. (2.14), whereas the
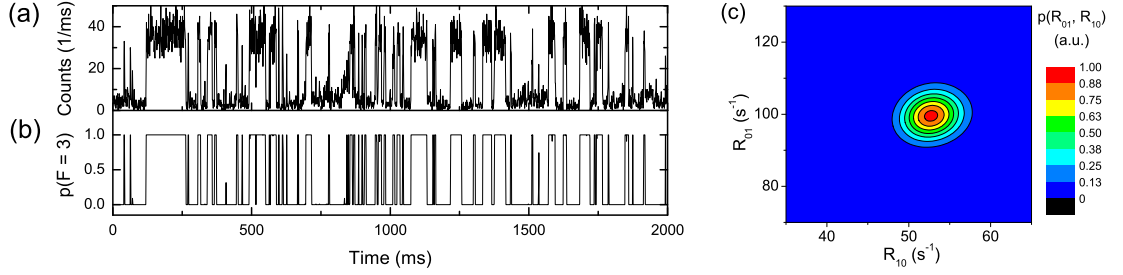
Figure 2.4: (a) Single random telegraph signal, as in Fig. 2.2. (b) Reconstructed atomic state after Bayesian state and rate update in terms of the probability to be in state $|0\rangle = |F = 3\rangle$. (c) Probability distribution for the rates after seven random telegraph signals like in (a) have been analyzed.

second factor $p(R_{01}, R_{10})$ is assumed to be time-independent. It can be calculated by summing over the atomic states:

$$p(R_{01}, R_{10}) = \sum_{\alpha'} p(\alpha', R_{01}, R_{10}) \,. \tag{2.16}$$

Analogous to Eqn. (2.12), the combined probabilities are updated after each time bin as follows:

$$p_{\text{post}}(\alpha, R_{01}, R_{10}) = \frac{p(n|\alpha, R_{01}, R_{10}) \, p_{\text{pri}}(\alpha, R_{01}, R_{10})}{\sum_{\alpha'} \sum_{R'_{01}} \sum_{R'_{10}} p(n|\alpha', R'_{01}, R'_{10}) \, p_{\text{pri}}(\alpha', R'_{01}, R'_{10})} \,, \tag{2.17}$$

where $p(n|\alpha, R_{01}, R_{10}) = p(n|\alpha)$ are the count rate probabilities as shown in Fig. 2.1 which only depend on the atomic state $|\alpha\rangle$.

So the whole procedure works as follows: First, one chooses an initial (flat) distribution $p(\alpha, R_{01}, R_{10})$. The rates are usually discretized on a grid. Using Eqns. (2.16) and (2.15), the distribution can be factorized into $p(R_{01}, R_{10})$ and $p(\alpha|R_{01}, R_{10})$ for each possible combination of R_{01}, R_{10}. The time evolution of the $p(\alpha, t|R_{01}, R_{10}) \rightarrow p(\alpha, t + \Delta t_{\text{bin}}|R_{01}, R_{10})$ are calculated according to Eqn. (2.14). Applying Eqn. (2.15) again, on obtains the *a-priori*-probabilities needed for the next update

$$p_{\text{pri}}(\alpha, R_{01}, R_{10}) = p(\alpha, t + \Delta t_{\text{bin}}|R_{01}, R_{10}) \, p(R_{01}, R_{10}) \,. \tag{2.18}$$

Depending on the number of counts n, the *a-posteriori*-probabilities are calculated using Eqn. (2.17) for each combination of α, R_{01}, R_{10}. Then the whole cycle starts again.

If one is only interested in the probabilities of the rates, one applies Eqns. (2.16). Conversely, if one is only interested in the probabilities of the atomic states, one

has to sum up over all possible rates:

$$p(\alpha) = \sum_{R'_{01}} \sum_{R'_{10}} p(\alpha, R'_{01}, R'_{10}) \, . \tag{2.19}$$

The random telegraph signal from Fig. 2.2 is shown again in Fig. 2.4 (a) together with the state probability $p(0) = p(|F = 3\rangle)$ as a function of time (b) and the probability distribution for the rates $p(R_{01}, R_{10})$, see Fig. 2.4 (c). This represents the knowledge about the rates in our system after seven experimental runs. From a flat distribution at the beginning, it has evolved to a well-defined 2D-Gaussian, becoming more and more narrow with time. The distribution can be characterized by the expectation values $\langle R_{01} \rangle, \langle R_{10} \rangle$ and the variances of the distribution along the R_{01} and R_{10}-axes, for instance

$$\sigma_{R_{01}}^2 = \sum_{R'_{01}} \sum_{R'_{10}} (R'_{01} - \langle R_{01} \rangle)^2 \, p(R'_{01}, R'_{10}) \, . \tag{2.20}$$

For this specific measurement, the results are

$$R_{01} = (100.0 \pm 4.5) \, \text{s}^{-1}, \quad R_{10} = (52.7 \pm 2.5) \, \text{s}^{-1}. \tag{2.21}$$

Update of time-dependent states and rates

So far, the transition rates between the states $|0\rangle$ and $|1\rangle$ were assumed to be constant in time. This assumption was reflected by the continuous update of the probability distribution for the rates $p(R_{01}, R_{10})$ during the experimental sequences and not resetting it to a flat distribution. However, in a quantum jump spectroscopy experiment, I expect the rates to change with detuning, i.e. with time. This can already be recognized in a random telegraph signal where the detuning is swept see Fig. 2.5 (a). The frequency of quantum jumps obviously increases and decreases again. To account for the rapidly changing rates, the sequence with a typical total duration of $\tau_{\text{seq}} = 3000 \, \text{ms}$ is sub-divided into N_{int} time slots of length

$$\tau_{\text{int}} = \frac{\tau_{\text{seq}}}{N_{\text{int}}}, \tag{2.22}$$

in which the rates are assumed to be constant, as in the previous section. While the *state* probabilities $p(\alpha)$ are still initialized only at the beginning of each experimental run (when a new atom has been prepared) and are continuously updated until the end of the sequence, the *rate* probabilities are initialized and updated within each of the N_{int} time slots. Instead of a single, there are now N_{int} independent probability distributions for the rates. At the beginning of each time slot in the first run, the corresponding $p(R_{01}, R_{10})$ is initialized to a flat distribution, see Fig. 2.5 (b). The combined probability is then given by

$$p(\alpha, R_{01}, R_{10}) = p(\alpha) \, p(R_{01}, R_{10}) \, , \tag{2.23}$$
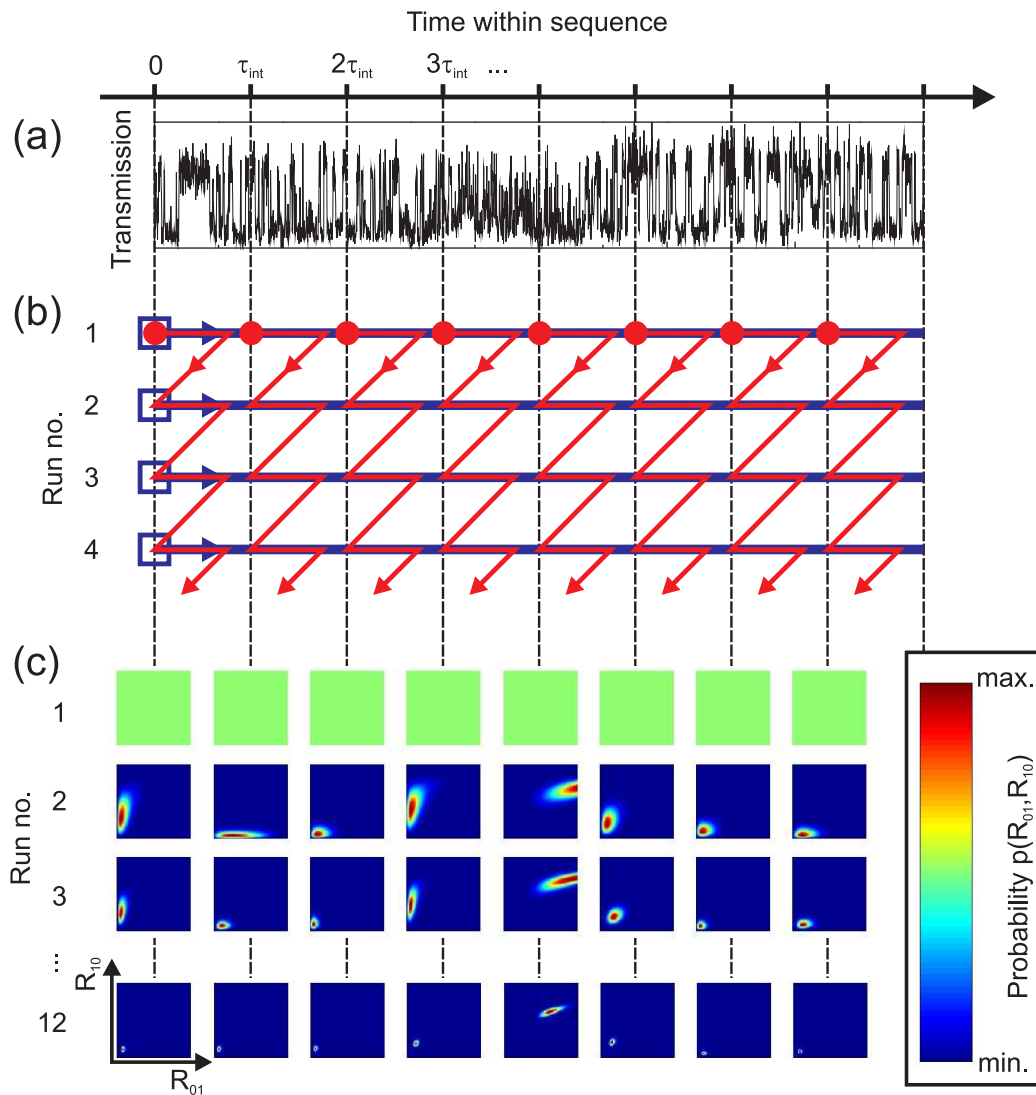
Figure 2.5: (a) Random telegraph signal measured in a single experimental run with a single atom. (b) Bayesian update scheme: The atomic states are initialized (blue squares) at the beginning of each experimental run and are updated (blue lines) until the end of the sequence. The rates are initialized (red dots) at the beginning of each time slot in the first run and then updated (red lines) only within their time slot. (c) Evolution of the rate distributions $p(R'_{01}, R'_{10})$ in the range $(0 \dots 1000\,\mathrm{s}^{-1}) \times (0 \dots 1000\,\mathrm{s}^{-1})$. Snapshots at the beginning of each time slot are shown with the color indicating the relative probability density (a.u.)

where $p(\alpha)$ is the state probability at the end of the previous time slot according to Eqn. (2.19). The combined probability is then updated as described in the previous section until the end of the time slot. Then, the updated rate distribution $p(R_{01}, R_{10})$ is calculated with Eqn. (2.16). This distribution is then further updated in the same time slot of the second and following runs.

Note that this update scheme is a generalized version of the update scheme described in the preceding section. They are equivalent for the case $N_{\text{int}} = 1$.

2.3.2 Experimental results

For quantum jump spectroscopy, random telegraph signals as shown in Fig. 2.5 (a) are recorded. Here, a single atom is prepared inside the cavity and the transmission of the probe laser is recorded. At the same time, it is exposed to the two circularly polarized Raman laser beams running along the dipole trap with a total power of about $100\,\mu\text{W}$ and a single-photon detuning of $\Delta_{\text{R}}/2\pi = 33\,\text{GHz}$. While the atom is kept for three seconds inside the cavity, the Raman-two-photon detuning is swept from $\delta_{\text{R}}/2\pi = 1.5\,\text{MHz}$ to $-1.5\,\text{MHz}$. In addition, a magnetic guiding field can be applied to lift the degeneracy of the Zeeman sublevels.

Measurement without magnetic guiding field　First, I discuss the measurement without magnetic guiding field, which is shown in figs. 2.5 and 2.6, respectively.

The sequence is subdivided into $N_{\text{int}} = 60$ time slots, which is a good compromise between spectral resolution and signal-to-noise ratio. Exemplary, the rate distributions $p(R_{01}, R_{10})$ at the beginning of eight time slots are shown in Fig. 2.5 (c). They are each discretized on a equidistantly spaced grid with 100×100 entries for a range of rates $(0 \ldots 1000\,\text{s}^{-1}) \times (0 \ldots 1000\,\text{s}^{-1})$. After eleven experimental runs, most of the rate probability distributions have converged from a flat distribution (uniform green) to narrow peaks. From the final distributions, the most probable rates and their standard deviations are calculated, see Fig. 2.6 (c).

However, at around $t = 1500\,\text{ms}$, the frequency of quantum jumps is almost at the limit of what can be resolved at this binning time of $1\,\text{ms}$. This can also be seen in the trace of the calculated state probabilities in Fig. 2.6 (b), where they become very 'dense' at that time. When I stretch the time scale by a factor of five, it is hard to identify any quantum jump in the transmission trace and even the Bayesian state probabilities become 'spiky'[1], see Fig. 2.6 (d,e). To resolve dynamics that is faster than about $1/\Delta t_{\text{bin}} = 1\,\text{ms}^{-1} = 1000\,\text{s}^{-1}$, a shorter binning time would be required[2]. Moreover, in this regime, the linear approximation of Eqn. (2.14) becomes inappropriate and should be replaced by the exact, exponential solution of Eqn. (2.13).

---

[1]A 'spike' is an non-complete transition between the two states
[2]Unfortunately, the count rate histograms for other binning times were not available.
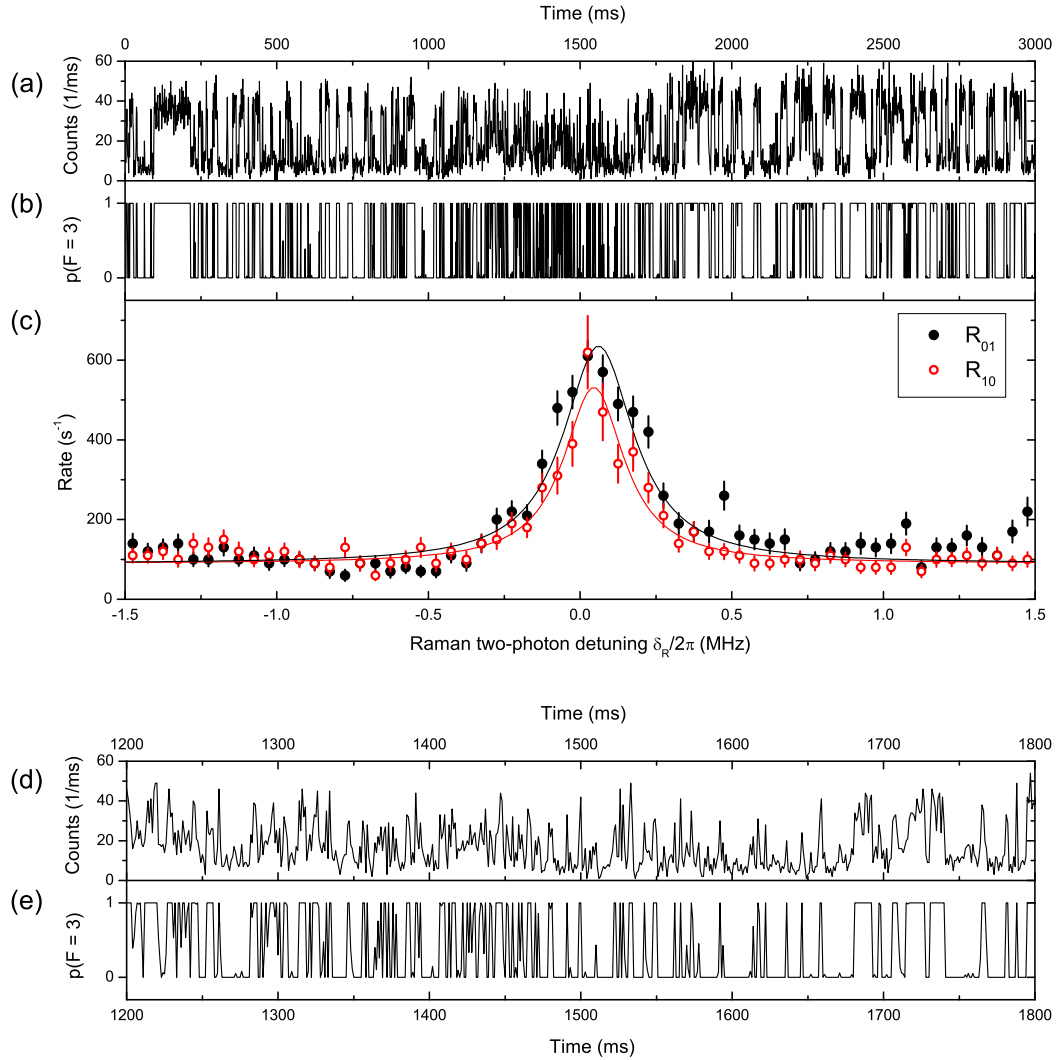
Figure 2.6: (a) Single transmission trace, obtained with a single atom inside the cavity. (b) Probability for the atom to be in state $|0\rangle = |F = 3\rangle$ for the trace in (a), obtained with the Bayesian time-dependent rate update. (c) Transition rates R_{01} and R_{10}, obtained from the Bayesian analysis of twelve experimental runs. (d) Detail enlargement of the trace shown in (a), with the time axis stretched by a factor of five. (e) Corresponding state probability for the trace in (d).

When I fit the spectra in Fig. 2.6 (c) with a Lorentzian function

$$R = R_0 + \frac{\hat{R}}{1 + 4(\delta_{\mathrm{R}} - \delta_{\mathrm{R},0})^2/w^2} \,, \tag{2.24}$$

I obtain the following parameters:

Rate	R_{01}	R_{10}
$w/(2\pi\,\mathrm{kHz})$	284 ± 33	244 ± 29
$\hat{R}/(\mathrm{s}^{-1})$	546 ± 46	442 ± 52
$R_0/(\mathrm{s}^{-1})$	89 ± 7	90 ± 4
$\delta_{\mathrm{R},0}/(2\pi\,\mathrm{kHz})$	61 ± 11	45 ± 10

First of all, the full-width-at-half maximum w is about three times larger than the (inhomogeneous) spectral width of $(74 \pm 25)\,\mathrm{kHz}$ that has been measured in a microwave spectroscopy experiment without probing the atomic state during the microwave pulses. Here, the coherently driven system is continuously probed, thus the spectrum should be broadened due to the Quantum Zeno effect, as discussed in section 2.2. The width has to be compared with the measurement rate Γ_{m}, that is given by $\kappa n_{\mathrm{p},0}$, see Eqn. (2.10). From a photon count rate of $R_{\mathrm{D}} = 33\,\mathrm{ms}^{-1}$ without background, I infer a mean intracavity photon number of $n_{\mathrm{p},0} = 0.23$, see Eqn. 1.8. The measurement rate is thus $\Gamma_{\mathrm{m}} = 2\pi \times 92\,\mathrm{kHz}$ and the width of the spectrum should be at least twice as large. If one takes also into account the inhomogeneous width of $(74 \pm 25)\,\mathrm{kHz}$, one expects a spectral width of about $260\,\mathrm{kHz}$. One can at least conclude that measured values for w are on the same order of magnitude.

To compare the amplitude $\hat{R}$ with the theoretical value $R_{01,\mathrm{c}} = \Omega_{\mathrm{R}}^2/\Gamma_{\mathrm{m}}$ for the resonant case, one needs to estimate the resonant Rabi frequency Ω_{R} of the Raman transition between the two hyperfine states. Driving Raman Rabi oscillations between the outermost Zeeman sublevels $|F = 4, m_F = -4\rangle$ and $|F = 3, m_F = -3\rangle$ yields an effective maximum Rabi frequency of $\Omega_{0,\mathrm{max}} = 2\pi \times 14\,\mathrm{kHz}$. Since the dipole matrix elements between the ground and excited states are on average lower than for this specific transition, I assume an effective average Raman Rabi frequency of only $\Omega_{\mathrm{R}} \approx 0.6\,\Omega_{0,\mathrm{max}} \approx 2\pi \times 8\,\mathrm{kHz}$. From this, I obtain a state-changing rate of about $R_{01,\mathrm{c}} = 4000\,\mathrm{s}^{-1}$. This value is almost one order of magnitude higher than the measured ones. One possible explanation for this discrepancy is the limited time resolution of the measurement of $1\,\mathrm{ms}$, as discussed above. In order to exclude this, one would need to perform the experiment at a higher temporal resolution or with even smaller Rabi frequencies Ω_{R}. Another, physical reason might be optical pumping of the atoms to Zeeman sublevels where the Raman Rabi frequencies are even smaller (only about 40%) than I have assumed here, in conjunction with the strong (quadratic) dependence of $R_{01,\mathrm{c}}$ on Ω_{R}. To check this, one would need to prepare the atoms in a specific Zeeman sublevel before performing the measurement, making sure at the same time that de-pumping to other sublevels can be neglected, i.e. that the Rabi frequency doesn't change.

Figure 2.7: Polarization configuration: The probe laser is linearly polarized and propagating along the cavity axis, while the Raman laser and optical pumping beams are circularly polarized and running along the dipole trap axis.
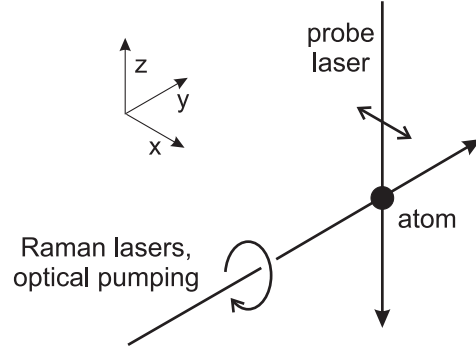
If the transitions between the two hyperfine ground states would be purely coherent, i.e. without any spontaneous scattering events, the transition rates R_{01} and R_{10} would vanish for large two-photon detunings $|\delta_R| \gg (\Gamma_m, \Omega_R)$, according to Eqn. (2.7). However, the measured spectra have an offset R_0 of about $100 \, \text{s}^{-1}$. One contribution to the state-changing rate is the off-resonant inelastic Raman scattering of the probe laser light. This leads to a transition rate from state $|1\rangle$ to state $|0\rangle$ of about $50 \, \text{s}^{-1}$, as obtained from the measurement with a weak repumping beam applied instead of the Raman lasers. This cannot fully explain the measured offset, in particular not the offset of R_{01} for the opposite direction. Therefore, one has to consider the scattering rate induced by the Raman laser beams: From a total power of about $P \approx 0.1 \, \text{mW}$ and a beam waist of $w = 86 \, \mu\text{m}$ at the position of the cavity, one obtains an intensity of $I = 2P/(\pi w^2) \approx 900 \, \text{mW/cm}^2$. The total scattering rate far from atomic resonance is given by (cf. [80])

$$R_{\text{sc,tot}} \approx \gamma \frac{I}{I_{\text{sat}}} \left(\frac{\gamma}{\Delta} \right)^2 \approx 80 \, \text{s}^{-1} \,, \tag{2.25}$$

where $I_{\text{sat}} = 1.1 \, \text{mW/cm}^{-2}$ denotes the saturation intensity and $\Delta = \Delta_R$ is the single-photon detuning. In this far-off-resonant regime, the hyperfine ground state changes on average after two scattering events, thus $R_{\text{sc,tot}}/2 \approx 40 \, \text{s}^{-1}$. Therefore, the spontaneous scattering induced by the Raman laser beams is probably the main contribution to our measured offset R_0 of the rates. A minor contribution should be spontaneous scattering by the trapping laser fields, which is on the order of several s^{-1} for both the lock laser [38] and the dipole trap [39]. To quantify the contributions of all possible sources of spontaneous scattering, one would need to vary them independently.

Magnetic guiding fields and optical pumping

The method of quantum jump spectroscopy can be applied as an in-situ diagnostics of the internal dynamics of the atoms inside the cavity. In particular, when a magnetic guiding field is applied, the degeneracy of the Zeeman sublevels is lifted and the two-photon detuning δ_R depends on the specific $|F = 3, m_F\rangle \leftrightarrow |F =$
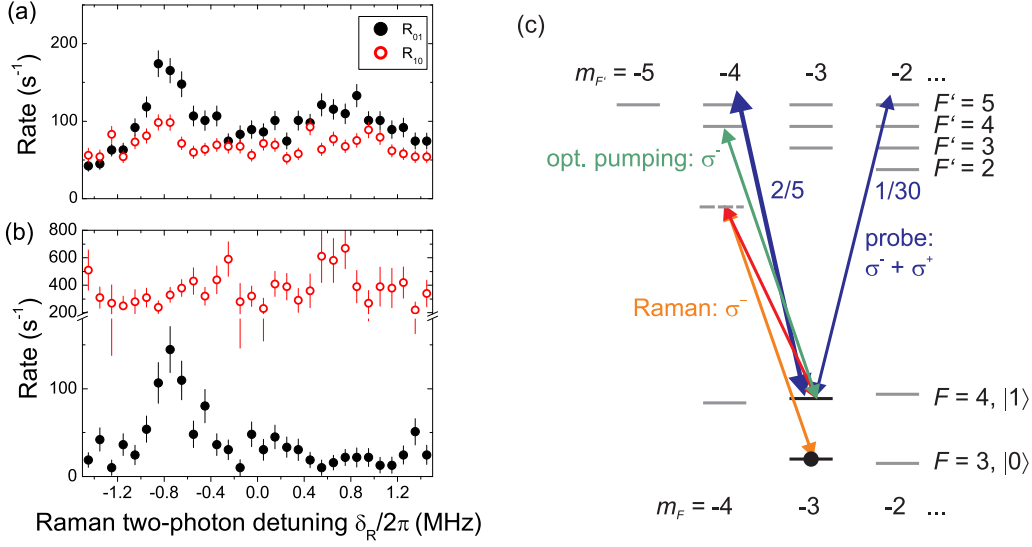
Figure 2.8: (a) Quantum jump spectra taken with a magnetic guiding field along the y-direction. (b) Same as in (a) but with an additional optical pumping beam applied along the y-axis. (c) Part of the scheme of the Zeeman sublevels in Cesium and the laser couplings. The numbers $2/5$ and $1/30$ are proportional to the line strengths (excitation probabilities) of the corresponding transitions ($\propto |\Omega_{\text{ge}}|^2$).)

$4, m_F'\rangle$ transition. Moreover, only specific values of $\Delta m_F \equiv m_F' - m_F$ are allowed, depending on the laser light polarizations and propagation directions with respect to the direction of the guiding field (selection rules). The transition rates R_{01}, R_{10} should thus depend on δ_R according to the occupation of the corresponding Zeeman sublevels.

Here, we apply magnetic guiding field with a flux density of $|\vec{B}| = 0.4\,\text{G}$. This leads to an frequency shift of $-0.14\,\text{MHz}\cdot m_F$ for the $|F = 3\rangle$ sublevels and of $+0.14\,\text{MHz}\cdot m_F$ for the $|F = 4\rangle$ sublevels. In particular, the transitions between the outermost Zeeman sublevels $|3, \pm 3\rangle \leftrightarrow |4, \pm 4\rangle$ occur at $\delta_\text{R}/2\pi = \pm 0.96\,\text{MHz}$. Moreover, we study the influence of an optical pumping beam on the distribution over Zeeman sublevels.

B-field along the y-direction The spectra with a magnetic guiding field applied along the y-direction are shown in Fig. 2.8 (a,b). They are obtained from 17 and 3 (!) random telegraph signals, respectively. The data are subdivided into $N_\text{int} = 30$ time slots. The spectrum in (b) was taken with an additional, circularly polarized optical pumping beam, resonant with the $|F = 4\rangle \leftrightarrow |F' = 4\rangle$ transition and co-propagating with the Raman laser beams. Concerning the spectrum in (a), the rate R_{01} exhibits a strong maximum at $\delta_\text{R}/2\pi = -0.77\,\text{MHz}$ and a weaker and broader

one at about $+0.8\,\text{MHz}$. The stronger one lies $-0.83\,\text{MHz}$ with respect to the center $\delta_\text{R}/2\pi = 0.06\,\text{MHz}$ of the resonance without B-field. Since the Raman lasers can only drive transitions with $\Delta m_F = 0$ due to selection rules, it can be attributed to the transition from $|3, -3\rangle$ to $|4, -3\rangle$, see Fig. 2.8 (c). Since the Raman Rabi frequencies Ω_R of the $|3, m_F\rangle \leftrightarrow |4, m_F\rangle$ transitions are symmetric with respect to m_F and are even highest for $m_F = 0$, I conclude: if an atom is in the hyperfine state $|0\rangle = |F = 3\rangle$, it is most likely in the $|F = 3, m_F = -3\rangle$ sublevel. With a lower probabilty they can also be found on the opposite side, e.g. in state $|F = 3, m_F = 3\rangle$, causing the weaker maximum at $\delta_\text{R}/2\pi = +0.8\,\text{MHz}$. The occupation of the outer m_F-states is an optical pumping effect caused by the probe laser light. With the quantization axis (the B-field direction) perpendicular to its linear polarization, it can be regarded as driving σ^+ and σ^- transitions simultaneously, see Fig. 2.8 (c). The σ^- component has a higher coupling strength than the σ^+ component if $m_F < 0$, and vice versa. Therefore, the atom will be pumped to the outermost m_F-states [38]. The imbalance in favor of the negative m_F-values might arise from the inelastic scattering of Raman laser light (σ^- transitions), which has been estimated above. To check this, one would need to change the polarization of the Raman beams and/or reverse the direction of the magnetic field.

However, the double-peak structure in the R_{01} data is not significantly reflected in the spectrum for R_{10}, although the coherent Raman transitions are bi-directional. The latter spectrum is even significantly lower and almost compatible with the independently measured transition rate $R_{10} \approx 50\,\text{s}^{-1}$ caused by the probe laser. A possible explanation for those observations is rapid optical pumping to the outermost $m_F = \pm 4$ states as soon as the atom is in state $|F = 4\rangle$. From the states $|F = 4, m_F = \pm 4\rangle$, there are no allowed Raman transitions to $|F = 3, m_F = \pm 3\rangle$ in this configuration (selection rule: $\Delta m_F = 0$) and thus $R_{10} < R_{01}$ and there also no maxima at $\delta_\text{R}/2\pi = \pm 0.96\,\text{MHz}$ related to $|3, \pm 3\rangle \leftrightarrow |4, \pm 4\rangle$ transitions.

The spectra presented in Fig. 2.8 (b) are recorded while the additional optical pumping beam is continuously switched on and driving σ^- transitions, see (c). Concerning the R_{01} spectrum, there is still a strong maximum at $\delta_\text{R}/2\pi = -0.74\,\text{MHz}$ as in (a), but for larger values, the rate has strongly decreased. This indicates optical pumping to sublevels with negative m_F, as is expected for this configuration. Moreover, the rate R_{10} has strongly increased over the whole frequency range, with no significant dependence on δ_R. I attribute this to inelastic scattering by the optical pumping beam: If the beam is not perfectly left-handed circularly polarized but contains a small fraction of the opposite polarization, it can also drive σ^+ transitions. So even if the atom is the state $|F = 4, m_F = -4\rangle$, which is a dark state for σ^- transitions, it can be excited to $|F' = 4, m'_F = -3\rangle$ and decay from there to $|F = 3\rangle$. For a typical intensity of $I = 0.4\,\text{mW/cm}^2$, assuming of a polarization impurity of 10^{-3}, I estimate a state-changing rate of about $400\,\text{s}^{-1}$. This value is compatible with our measurement.
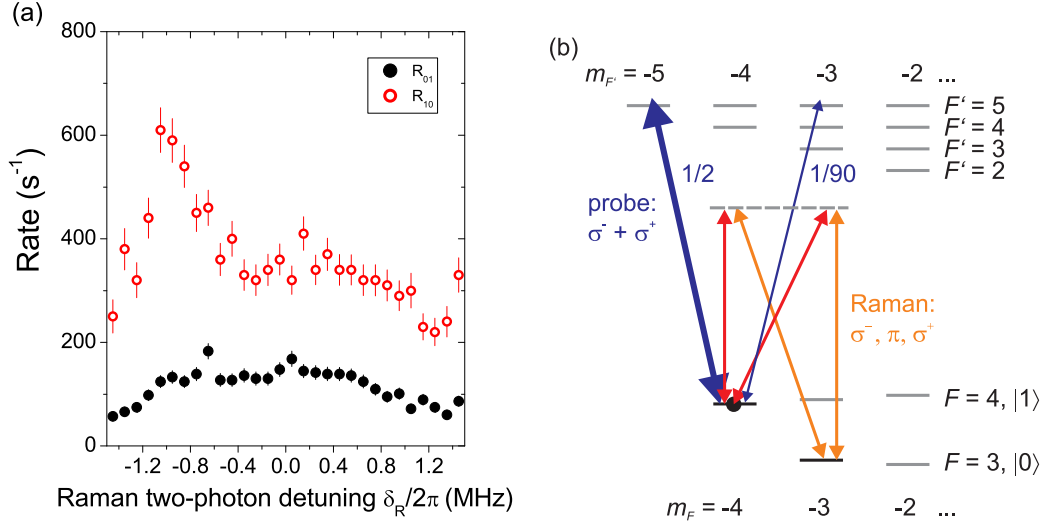
Figure 2.9: (a) Quantum jump spectra taken with a magnetic guiding field along the z-direction. (b) Part of the scheme of Zeeman sublevels in Cesium and the laser couplings.

B-field along the z-direction   When we apply a magnetic guiding field along the z-direction, i.e. along the cavity axis, the probe laser will still drive σ^+ and σ^- transitions simultaneously, as in the B_y-case, resulting in optical pumping to to the outer m_F sublevels, see Fig. 2.9 (b). In contrast to the previous case, the selection rule for the Raman transition is now $\Delta m_F = \pm 1$, see section 1.3.3. Thus transitions between the outermost sublevels are allowed. In fact, the measured R_{10}-spectrum in Fig. 2.9 (a) exhibits a strong maximum at $\delta_{\mathrm{R}}/2\pi = -1.0\,\mathrm{MHz}$ which can be attributed to the $|4, -4\rangle \rightarrow |3, -3\rangle$ transition.

However, it is unclear why there is an imbalance in favor of the negative m_F values. As proposed already for the B_y-case, the reason for this asymmetry could be narrowed down by reversing the direction of the magnetic guiding field: If the B-field itself breaks the symmetry of the system, i.e. by Zeeman-shifting positive and negative m_F sublevels into opposite directions, the spectrum should not change, since the B-field also defines the quantization axis. Otherwise, if the laser polarizations cause the imbalance, the spectrum should be flipped horizontally. For instance, a circularly polarized laser beam running along the B-field direction would drive σ^+ instead of σ^- transitions when we reverse the field and optically pump the atoms to, e.g., $|4, 4\rangle$ instead of $|4, -4\rangle$. One should then see a maximum in the spectrum at $\delta_{\mathrm{R}}/2\pi = +1.0\,\mathrm{MHz}$, corresponding to the $|4, 4\rangle \rightarrow |3, 3\rangle$ transition.

Moreover, the strong maximum at $\delta_{\mathrm{R}}/2\pi = -1.0\,\mathrm{MHz}$ is not reflected in the R_{01}-spectrum, although the Raman transitions are in general bi-directional. One possible explanation could be a three-level EIT-effect, suppressing the $|3, -3\rangle \rightarrow |4, -4\rangle$

transition, since the states $\{|3, -3\rangle, |4, -4\rangle, |5', -5\rangle\}$ form a coherently coupled ladder system. This speculation could be checked by varying the probe-atom detuning Δ_{pa}, since an EIT-effect sensitively depends on the two-photon resonance condition, see next chapter.

2.4 Summary and conclusions

In this chapter I have presented first results on the continuous observation of a single atom which is driven by a two-photon Raman process, connecting the two hyperfine ground states, serving also as qubit states in various schemes for quantum information processing. The dynamics of the internal state of an atom is monitored in real time over several seconds in a non-destructive way, by a projective QND-type of measurement as a random telegraph signal. In contrast to our previous work, the transitions between the two hyperfine states are now coherently driven, which is not only a bi-directional process, but gives also rise to a fundamental effect, the Quantum Zeno effect. I estimated that this effect should cause a significant reduction of the hyperfine state-changing rates. This should be taken into account when coherent pulses are used in a feedback scheme [49].

Moreover, the coherent process in combination with magnetic guiding fields allows for selectively driving transitions between certain Zeeman-sublevels. This gives rise to a new in-situ diagnostic technique for the internal-state dynamics of a single atom inside a high-finesse cavity. Here, I have generalized a Bayesian update formalism for the analysis of random telegraph signals for the case of time-dependent transition rates, with in principle arbitrarily high resolution. Using only a few or a dozen atoms, detailed spectra can already be obtained due to the long observation time, because of the non-destructiveness of the measurement and the high information rate. In contrast, with our standard push-out technique we gain only a single bit of information per trapped atom and one requires hundreds or thousands of atoms for a similar spectrum.

3 Theory of EIT in an optical cavity

3.1 Introduction

Before presenting our measurements on Electromagnetically Induced Transparency with a small number of atoms inside our optical resonator, I will first discuss different theoretical models. The basic problem is to calculate the transmission of a cavity filled with an atomic medium with three internal states, in a so-called Λ-configuration, see Fig. 3.1. In the extreme case, this medium is formed by a single atom only. The atomic $|g_1\rangle \leftrightarrow |e\rangle$ transition is driven by a strong (''classical'') control laser. We are interested in the linear response of the combined atom-cavity system to an arbitrarily weak probe field, which is coupled to the cavity. Especially, we want to study the steady state of the system. First, I will present two different approaches: a so-called ''semiclassical model'', considering both light in a classical way and only the atom quantum mechanically, and a ''quantum model'', treating also the cavity field quantum mechanically. By comparing the results of the two models, I point out conceptual differences between them. It turns out that in the regime of strong atom-cavity coupling, $g^2/(2\kappa\gamma) \gg 1$, the Purcell-effect [81] adds a contribution to the transmission that is not contained in the semiclassical model. I derive an analytical expression for this additional contribution to extend the semiclassical model such that the numerical results of the quantum model can be reproduced.

Furthermore, the quantum model will be extended to the case of more than one atom. Doing so, the effects of a non-vanishing probe laser power and the multilevel hyperfine structure of cesium are taken into account. However, the computational
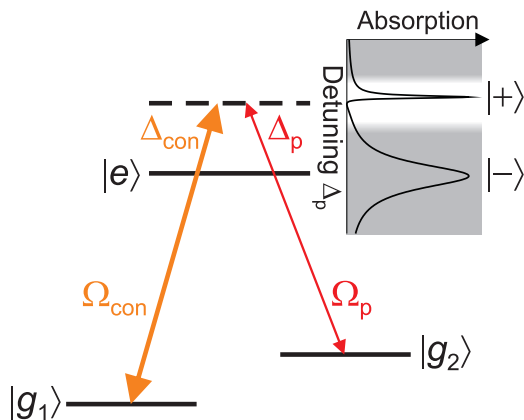
Figure 3.1: Energy level scheme of a three-level atom in free space, interacting with a strong control laser with Rabi frequency Ω_{con} detuned by Δ_{con} from the atomic $|g_1\rangle \leftrightarrow |e\rangle$ transition. The insert shows the absorption of a weak probe beam with Rabi frequency Ω_{p} as a function of its detuning Δ_{p} from the atomic $|g_2\rangle \leftrightarrow |e\rangle$ transition, while Δ_{con} remains fixed.

load of the more realistic model can be enormous. Finally, I will outline methods to reduce the number of effective levels and thus the dimension of the Hilbert space.

3.2 Semiclassical model

The linear response of a medium with three internal states in free space to a probe beam at angular frequency ω_{p} can be described in terms of the linear susceptibility $\chi^{(1)}(\omega_{\mathrm{p}})$. Here, the Rabi frequency Ω_{p} of the probe beam is much lower than the control laser Rabi frequency Ω_{con}, so $\chi^{(1)}$ is determined by the control beam. The real part $\chi' \equiv \mathrm{Re}\, \chi^{(1)}$ determines the phase shift and the imaginary part $\chi'' \equiv \mathrm{Im}\, \chi^{(1)}$ the absorption of the probe beam when it passes through the medium. The linear susceptibility is related to the coherence $\rho_{g_2 e}$ between ground state $|g_2\rangle$ and the excited state $|e\rangle$ by [82]

$$\chi^{(1)} = \frac{\varrho d_{g_2 e}^2}{\hbar \epsilon_0} \frac{\rho_{g_2 e}}{\Omega_{\mathrm{p}}}, \tag{3.1}$$

where ϱ denotes the atomic density and $d_{g_2 e}$ the electric dipole moment of the $|g_2\rangle \leftrightarrow |e\rangle$ transition. The coherence $\rho_{g_2 e}$ in first order with respect to the probe is obtained from a steady-state solution of a Lindblad master equation [21, 82][1]:

$$\rho_{g_2 e} = \Omega_{\mathrm{p}} \frac{1}{-\Delta_{\mathrm{p}} + \frac{\Omega_{\mathrm{con}}^2}{2i\gamma_{\mathrm{deph}} + 4\delta} - i\gamma}, \tag{3.2}$$

where $\delta = \Delta_{\mathrm{p}} - \Delta_{\mathrm{con}}$ is the two-photon detuning and $2\gamma = 2\gamma_1 + 2\gamma_2 = \Gamma$ is the sum of the decay rates from state $|e\rangle$ to the states $|g_1\rangle$ and $|g_2\rangle$. The phenomenological ground state dephasing rate γ_{deph} is used to model mainly technical effects that destroy the coherence between the two ground states, see next chapter. In this chapter, I consider only the idealized case where $\gamma_{\mathrm{deph}} = 0$. If one considers now a medium consisting of N atoms inside the mode volume V_{mode} of an optical cavity, each coupled to the cavity mode with a strength g defined as [36]:

$$g = d_{g_2 e} \sqrt{\frac{\omega}{2\hbar\epsilon_0 V_{\mathrm{mode}}}}, \tag{3.3}$$

where ω is the frequency of the $|g_2\rangle \leftrightarrow |e\rangle$ transition, and setting the density to $\varrho = N/V_{\mathrm{mode}}$, one obtains:

$$\chi^{(1)} = \frac{2Ng^2}{\omega} \frac{1}{-\Delta_{\mathrm{p}} + \frac{\Omega_{\mathrm{con}}^2}{2i\gamma_{\mathrm{deph}} + 4\delta} - i\gamma}. \tag{3.4}$$

The medium characterized by $\chi^{(1)}$ imposes additional losses and phase shifts on the light circulating inside the resonator of length l. These effects can be modeled

---

[1]In ref. [82], the definitions of Ω_{con} and γ_{deph} are two times smaller. In ref. [21], χ' has the opposite sign.

by adding terms to the expressions for the mirror intensity loss coefficient L and the empty cavity round-trip phase Φ, respectively (cf. [83]). For $|\chi^{(1)}| \ll 1$, the complex refractive index reads:

$$
n_{\text{ref}} = n' + in'' = \sqrt{1 + \chi^{(1)}} = \underbrace{1 + \frac{\chi'}{2}}_{n'} + i \underbrace{\frac{\chi''}{2}}_{n''} . \tag{3.5}
$$

A light wave with frequency ω_{p} travelling along the z-axis can be described by its time dependent electric field:

$$
\begin{aligned}
\vec{E}(z,t) &= \vec{E}_0 \exp\left\{-i(\omega_{\text{p}}t - n'kz)\right\} \exp\{-n''kz\} \\
&= \vec{E}_0 \exp\left\{-i(\omega_{\text{p}}t - kz)\right\} \exp\left\{ikz\frac{\chi'}{2}\right\} \exp\left\{-kz\frac{\chi''}{2}\right\},
\end{aligned} \tag{3.6}
$$

where $k = \omega_{\text{p}}/c$ denotes the magnitude of the wave vector. The last two exponential factors in (3.6) describe the additional phase shift and the absorption by the medium, respectively. Inside the filled cavity the wave accumulates a round-trip phase [36]

$$
\Phi' = \frac{2\pi\omega_{\text{p}}}{\omega'_{\text{FSR}}} = \omega_{\text{p}}\frac{2n'l}{c} = \underbrace{\frac{2\pi\omega_{\text{p}}}{\omega_{\text{FSR}}}}_{\Phi} + \frac{\omega_{\text{p}}l}{c}\chi' = 2\pi\frac{\omega_{\text{p}} - \omega_{\text{c}}}{\omega_{\text{FSR}}} + 2\pi\underbrace{\frac{\omega_{\text{c}}}{\omega_{\text{FSR}}}}_{\text{integer}} + \frac{\omega_{\text{p}}l}{c}\chi', \tag{3.7}
$$

where $\omega'_{\text{FSR}} = 2\pi c/(2n'l)$ is the free spectral range of the filled cavity. Substracting integer multiples of 2π, and substituting the empty-cavity round-trip time $\tau_{\text{r}} \equiv 2l/c$, one obtains

$$
\Phi' = \tau_{\text{r}}\left(\Delta_{\text{pc}} + \frac{\omega_{\text{p}}}{2}\chi'\right), \tag{3.8}
$$

where $\Delta_{\text{pc}} \equiv \omega_{\text{p}} - \omega_{\text{c}}$ is the detuning of the probe laser from the empty cavity resonance frequency.

In the limit of small intensity losses per round trip, the intensity loss L' during a single pass ($z = l$) is the sum of the losses L of one mirror and the absorption $1 - |\vec{E}(l,t)|^2/|\vec{E}_0|^2$ by the medium. In this limit, the mirror losses defined as the sum of the mirror transmission T and absorption A can further be substituted by $L = T + A = \kappa\tau_{\text{r}}$ [38], where κ denotes the cavity field decay rate. One obtains:

$$
L' = L + \left(1 - \exp\left\{-kl\frac{\chi''}{2}\right\}^2\right) \approx L + \frac{\omega_{\text{p}}l}{c}\chi'' = \tau_{\text{r}}\left(\kappa + \frac{\omega_{\text{p}}}{2}\chi''\right). \tag{3.9}
$$

Using expressions (3.8) and (3.9) one can now calculate the normalized transmission through the cavity, i.e. the transmission of a detuned probe laser through the filled cavity divided by the transmission of a resonant probe laser through the empty cavity (cf. [36]):
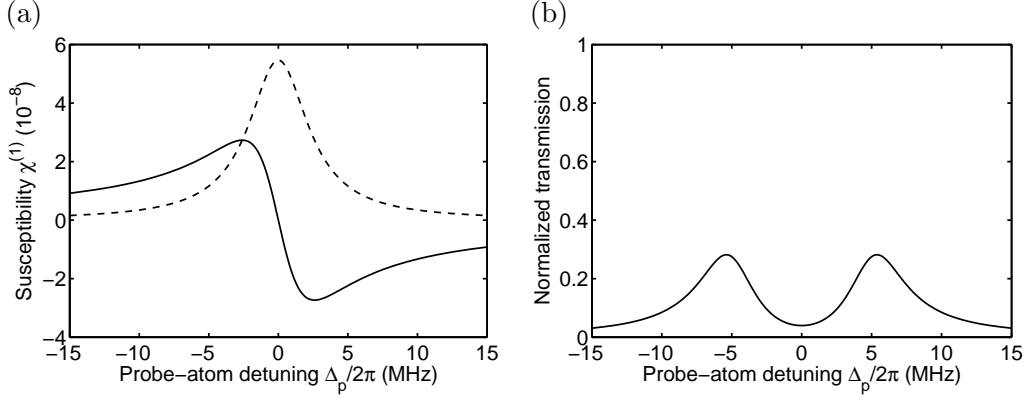
(a)

(b)

Figure 3.2: (a) Linear susceptibility of an effective two-level atom with $\gamma/2\pi = 2.6\,\text{MHz}$, coupled with $g/2\pi = 5$ MHz to the mode of an optical cavity. Solid line: real part χ'; dashed line: imaginary part χ''. (b) Normalized transmission of the cavity with $\kappa/2\pi = 2.4$ MHz, revealing the normal mode splitting.

$$\bar{T}_{\text{sc}}(\chi^{(1)}, \Delta_{\text{pc}}) = \frac{L^2}{L'^2 + 4(1 - L')\sin^2\frac{\Phi'}{2}}$$

$$\approx \frac{\kappa^2}{\left(\Delta_{\text{pc}} + \frac{\omega_{\text{p}}}{2}\chi'\right)^2 + \left(\kappa + \frac{\omega_{\text{p}}}{2}\chi''\right)^2}$$

$$= \frac{\kappa^2}{|\Delta_{\text{pc}} + i\kappa + \frac{\omega_{\text{p}}}{2}\chi^{(1)}|^2}. \tag{3.10}$$

In the well-known limit of an effective two-level system, which can be reached by simply setting the coupling between, e.g., $|g_1\rangle$ and $|e\rangle$ to zero ($\Omega_{\text{con}} = 0$, $\gamma_1 = 0$), one can derive an analytical expression for the normalized cavity transmission also from this semiclassical approach. In the idealized case of no dephasing ($\gamma_{\text{deph}} = 0$) and being near-resonant ($\omega \approx \omega_{\text{p}}$), the expression for the susceptibility (3.4) reduces to

$$\chi^{(1)} = -\frac{2g^2}{\omega_{\text{p}}}\frac{1}{\Delta_{\text{p}} + i\gamma} = \frac{2g^2}{\omega_{\text{p}}}\left(-\frac{\Delta_{\text{p}}}{\Delta_{\text{p}}^2 + \gamma^2} + i\frac{\gamma}{\Delta_{\text{p}}^2 + \gamma^2}\right). \tag{3.11}$$

The real and imaginary parts of the right-hand-side of equation (3.11) clearly reveal the dispersion and absorption profile of the atomic resonance, see Fig. 3.2(a). After insertion into (3.10), one obtains for the normalized transmission

$$\bar{T}(\Delta_{\text{pc}}, \Delta_{\text{p}}) = \kappa^2 \times \left[\left(\kappa + g^2\frac{\gamma}{\Delta_{\text{p}}^2 + \gamma^2}\right)^2 + \left(\Delta_{\text{pc}} - g^2\frac{\Delta_{\text{p}}}{\Delta_{\text{p}}^2 + \gamma^2}\right)^2\right]^{-1}, \tag{3.12}$$

which is equal to the corresponding expression in [38], the solution of a master equation in the weak probing limit with a *quantum mechanical* treatment of the cavity
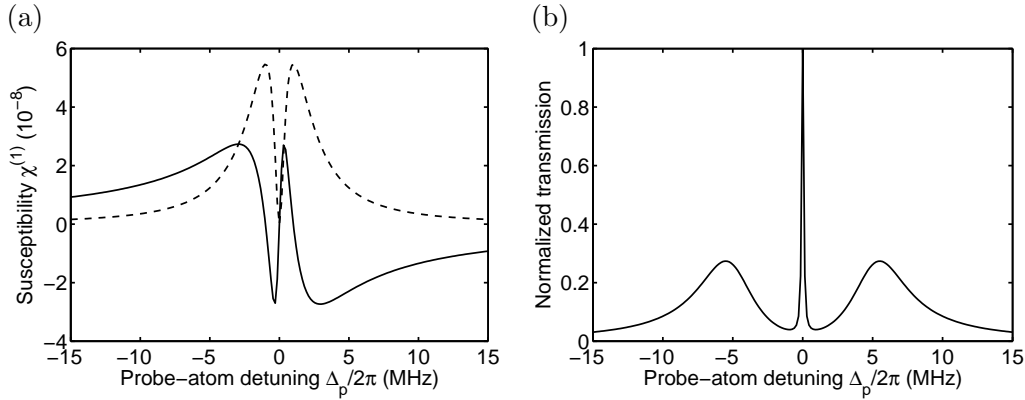
(a)

(b)

Figure 3.3: (a) Linear susceptibility of a three-level atom coupled with $g/2\pi = 5$ MHz to the mode of an optical cavity. Solid line: real part χ'; dashed line: imaginary part χ''. The control laser strength and detuning are $\Omega_{\mathrm{con}}/2\pi = 2$ MHz and $\Delta_{\mathrm{con}} = 0$, respectively. At $\Delta_{\mathrm{p}} = 0$, both χ' and χ'' vanish due to the EIT effect. (b) Normalized transmission of the cavity with $\kappa/2\pi = 2.4$ MHz, revealing the normal mode splitting and the narrow EIT transmission peak.

field. For a cavity which is resonant with the atomic transition, the transmission spectrum exhibits the symmetric normal mode splitting of $2g$, see Fig. 3.2(b).

When the coupling between $|g_1\rangle$ and $|e\rangle$ is now turned on, $\Omega_{\mathrm{con}} > 0$, the absorption χ'' vanishes at two-photon resonance and the dispersion χ' changes its slope around that point — the EIT effect. In the resonant case, Δ_{con}, a narrow dip in the center of the Lorentzian absorption curve is created, see Fig. 3.3(a). This leads ideally to a narrow transmission window through the cavity, see Fig. 3.3(b), which has been observed in experiments with a cold atomic ensemble [84] and recently with a few cold atoms [31]. The inverted, steep slope of χ' around two-photon resonance leads to a strong reduction of the group velocity of light pulses, called slow light [22–25].

In our off-resonant regime, $\Delta_{\mathrm{con}} \approx \Delta_{\mathrm{p}} \gg \gamma$, instead of a narrow absorption minimum at two-photon resonance, a narrow absorption peak with a Fano-like shape [85] is created at

$$\delta_{\mathrm{abs}} \approx \Omega_{\mathrm{con}}^2/(4\Delta_{\mathrm{con}}), \qquad (3.13)$$

see Fig. 3.4(a). Here, the increased losses from the resonator due to spontaneous scattering of the probe laser field by the atom lead to a transmission minimum, see Fig. 3.4(b). The full-width-at-half maximum of the absorption peak

$$\Delta\delta_{\mathrm{abs}} \approx \frac{\Gamma\Omega_{\mathrm{con}}^2}{4\Delta_{\mathrm{con}}^2}, \qquad (3.14)$$

can be much less than both the atomic linewidth Γ and the cavity linewidth 2κ. This is also the basis for a sub-Doppler cooling mechanism [32], see chapter 5.
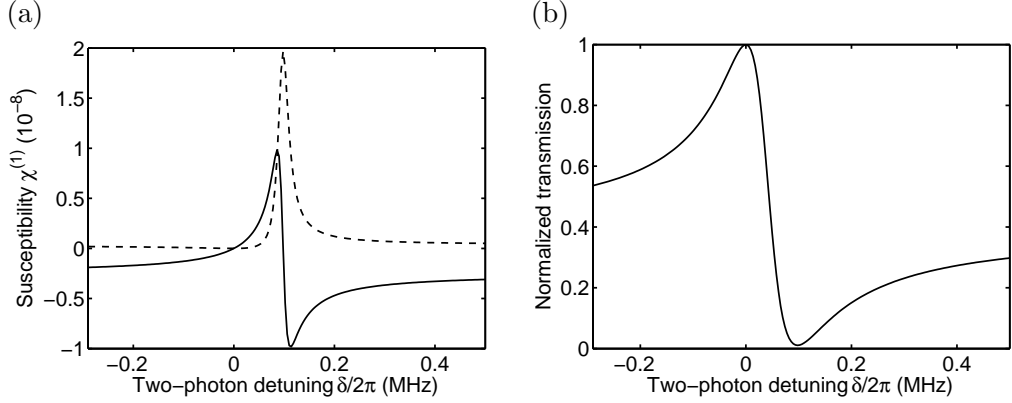
(a)

(b)

Figure 3.4: (a) Linear susceptibility of a three-level atom coupled with $g/2\pi = 3$ MHz to the mode of an optical cavity at a fixed probe laser detuning of $\Delta_\mathrm{p}/2\pi = 20$ MHz. Solid line: real part χ'; dashed line: imaginary part χ''. The control laser with strength $\Omega_\mathrm{con}/2\pi = 2.8$ MHz is swept over the two-photon resonance. In this off-resonant regime, only δ is important, so one could also sweep Δ_p instead, as long as $|\delta| \ll (\Delta_\mathrm{p}, \Delta_\mathrm{con})$. (b) Normalized transmission of the cavity with $\kappa/2\pi = 0.4$ MHz, resonant with the probe laser ($\Delta_\mathrm{pc} = 0$).

3.3 Quantum model

The system dynamics — now with the interaction of the atoms with the cavity field treated fully quantum mechanically — will be modeled using a master equation. The Hamiltonian, in a frame rotating with the probe laser frequency, in the rotating wave approximation, reads:

$$\hat{H} = \hat{H}_\mathrm{atom} + \hat{H}_\mathrm{cavity} + \hat{H}_\mathrm{int}, \tag{3.15}$$

$$\text{where} \quad \hat{H}_\mathrm{atom} = -\hbar\Delta_\mathrm{p}\hat{\sigma}_{ee} - \hbar\delta\hat{\sigma}_{g_1 g_1},$$

$$\hat{H}_\mathrm{cavity} = -\hbar\Delta_\mathrm{pc}\hat{a}^\dagger\hat{a},$$

$$\hat{H}_\mathrm{int} = i\hbar\frac{\Omega_\mathrm{con}}{2}(\hat{\sigma}_{eg_1} - \hat{\sigma}_{g_1 e}) + i\hbar g(\hat{\sigma}_{eg_2}\hat{a} - \hat{\sigma}_{g_2 e}\hat{a}^\dagger) + \hbar\mathcal{E}(\hat{a}^\dagger + \hat{a}),$$

where $\hat{\sigma}_{kl} \equiv |k\rangle\langle l|$ is the atomic projection operator, $\hat{a}$ is the annihilation operator and $\mathcal{E}$ the driving strength of the cavity field. To take into account the coupling to the environment, causing spontaneous emission, cavity field decay and ground state dephasing, one considers the time evolution of the reduced density matrix operator

$$\hat{\rho}(t) = \sum_{m,n} \rho_{mn}(t)\hat{\sigma}_{mn}, \tag{3.16}$$

where $\rho_{mn}(t)$ are the density matrix elements and $\hat{\sigma}_{mn}$ is defined on the product Hilbert space of the atomic and cavity states. We are interested in the steady state

transmission of the probe laser through the cavity. It can be obtained from the steady state of the density matrix operator $\hat{\rho}_{\mathrm{ss}}$, fulfilling

$$\frac{\mathrm{d}}{\mathrm{d}t}\hat{\rho}_{\mathrm{ss}} = 0. \tag{3.17}$$

The photon output rate from (both mirrors of) the cavity in steady-state is then proportional to the expectation value of the photon number operator $\hat{a}^\dagger\hat{a}$,

$$R_{\mathrm{p}} = 2\kappa\langle\hat{a}^\dagger\hat{a}\rangle = 2\kappa\,\mathrm{Tr}(\hat{a}^\dagger\hat{a}\hat{\rho}_{\mathrm{ss}}), \tag{3.18}$$

and the normalized transmission is obtained by comparing this with the output rate of an empty cavity on resonance (cf. [38]):

$$\bar{T}_{\mathrm{qu}} = R_{\mathrm{p}}\Big/\left(2\kappa\times\frac{\mathcal{E}^2}{\kappa^2}\right) = \frac{\kappa^2}{\mathcal{E}^2}\mathrm{Tr}(\hat{a}^\dagger\hat{a}\hat{\rho}_{\mathrm{ss}}). \tag{3.19}$$

The time evolution of $\hat{\rho}(t)$ is determined by the master equation in the Lindblad form [86]

$$\frac{\mathrm{d}}{\mathrm{d}t}\hat{\rho} = -\frac{i}{\hbar}[\hat{H},\hat{\rho}] + \gamma_1\mathcal{D}[\hat{\sigma}_{g_1e}]\rho + \gamma_2\mathcal{D}[\hat{\sigma}_{g_2e}]\rho + \kappa\mathcal{D}[\hat{a}]\rho + \frac{\gamma_{\mathrm{deph}}}{2}\mathcal{D}[\hat{\sigma}_{g_1g_1}]\rho, \tag{3.20}$$

$$\text{where}\quad \mathcal{D}[\hat{b}]\rho = 2\hat{b}\rho\hat{b}^\dagger - \hat{b}^\dagger\hat{b}\rho - \rho\hat{b}^\dagger\hat{b}.$$

The ground state dephasing is here (cf. [21]) assigned to the *state* $|g_1\rangle$ instead of the *transition* $|g_1\rangle \leftrightarrow |g_2\rangle$, causing all coherences $\{\rho_{kl}(t)|k\neq l\}$ between the state $|g_1\rangle$ and all other states to decay at a rate[2] $\gamma_{\mathrm{deph}}/2$.

Since an exact analytical solution of the master equation is only possible in special cases, one needs in general a numerical method. Here, I used the *quantum optics toolbox* [87] for *Matlab*, largely automating the process of setting up the equations of motions of the problem.

In Fig. 3.5, the normalized transmissions calculated numerically with this quantum model, Eqn. (3.19), are compared with the semiclassical solution, Eqn. (3.10). It turns out that they are equal only in the limit where all population of the excited state $|e\rangle$ decays back to the state $|g_2\rangle$ only, and not to $|g_1\rangle$, i.e. $\gamma_1 = 0$. In the more physical and realistic case where the decay rates to both ground states are almost equal ($2\gamma_1 \approx 2\gamma_2$), the transmission obtained from the quantum model is considerably higher than in the semiclassical model, in which the linear susceptibility does not depend on this branching ratio but only on the total decay rate. This difference is noteworthy because it contradicts the picture in which the cavity just converts the free-space susceptibility of the medium into transmission [31, 83]. So what is the physical effect of the cavity — in other words: how does it act on the system?

---

[2]Here, the definition of γ_{deph} is according to [21] and used in [30]. However, it would be more natural to replace $\gamma_{\mathrm{deph}}/2$ with γ_{deph}.
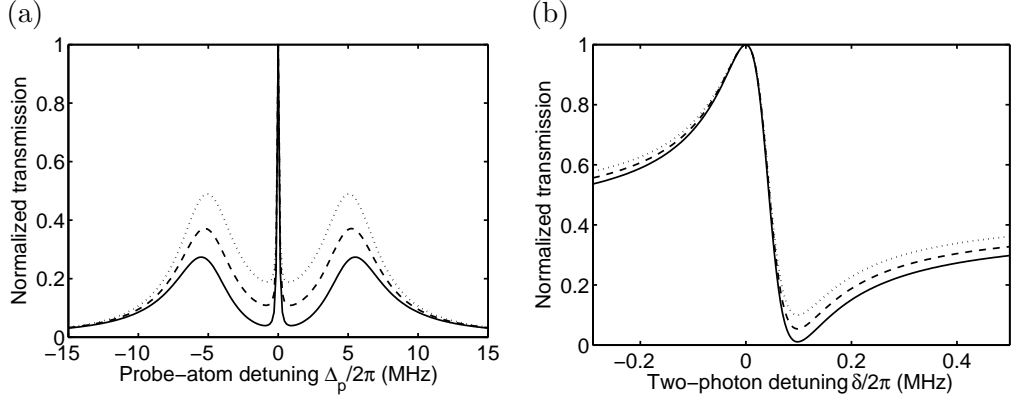
(a)

(b)

Figure 3.5: Comparison of the normalized transmission obtained from the semi-classical model (solid lines, $\gamma/2\pi = 2.6\,\mathrm{MHz}$) and the quantum model for different branching ratios (solid lines: $(\gamma_1, \gamma_2)/2\pi = (0, 2.6)\,\mathrm{MHz}$; dashed lines: $(\gamma_1, \gamma_2)/2\pi = (1.3, 1.3)\,\mathrm{MHz}$; dotted lines: $(\gamma_1, \gamma_2)/2\pi = (2.5, 0.1)\,\mathrm{MHz}$) (a) Resonant case, as in Fig. 3.3(b). (b) Dispersive regime, as in Fig. 3.4.

3.4 Extended semiclassical model

In the last section I have shown that the cavity transmission obtained from the semiclassical model is only equivalent to the full quantum treatment in a very special case. However, since the semiclassical model provides a more intuitive picture of the underlying physical mechanism, it is worthwhile to extend it such that the results of the quantum model can be reproduced. In the following discussion, I assume one idealized three-level atom in the weak-probing-limit without ground-state dephasing. In particular, a physical mechanism that generates the additional transmission in the quantum case has to be found.

The rate coefficient for photon loss from the filled cavity mode is given by the single-pass intensity loss (3.9) divided by half the round-trip time:

$$2\kappa_{\mathrm{ext}} = \frac{\tau_{\mathrm{r}}}{\tau_{\mathrm{r}}/2} \left(\kappa + \frac{\omega_{\mathrm{p}}}{2} \chi'' \right) = 2\kappa + \omega_{\mathrm{p}} \chi''. \tag{3.21}$$

The first term of the right-hand side of Eqn. (3.21) describes the loss through both mirrors and the last term describes absorption losses due to the medium. In the case of an ideal symmetric cavity, one half of the first kind of losses can be detected as transmission. For every photon that is detected directly in transmission, there are $\omega_{\mathrm{p}} \chi''/\kappa$ photons which are absorbed by the atom. With a probability of $\gamma_1/(\gamma_1 + \gamma_2)$, the excited atom decays subsequently to the state $|g_1\rangle$. An atom in this state can undergo a stimulated Raman transition to state $|g_2\rangle$, during which a photon is emitted from the cavity and every 2nd can be detected as additional transmission. The probability P_{rec} of this 'photon-recycling' can be calculated numerically from the time-dependent solution of the master equation (3.20), where the driving field
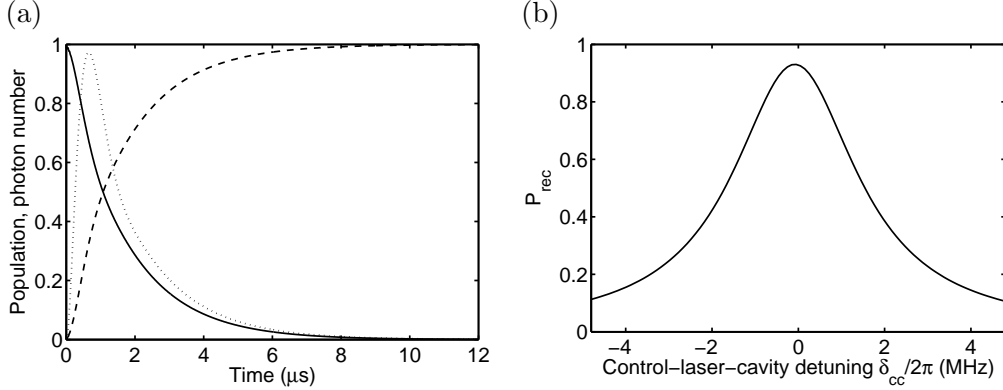
(a) (b)

Figure 3.6: (a) Populations of the states $|g_1\rangle$ (solid) and $|g_2\rangle$ (dashed) and the intracavity photon number (dotted, $10\times$ exaggerated) as a function of time after the system has been prepared in $|g_1\rangle$, obtained from a time-dependent solution of the master equation with parameters as in Fig. 3.4(b). (b) Recycling probability as a function of the detuning δ_{cc} of the control laser from the cavity, as a result of the numerical integration of the cavity output rate over time.

strength $\mathcal{E}$ is set to zero, by integrating the photon output rate (3.18) over time:
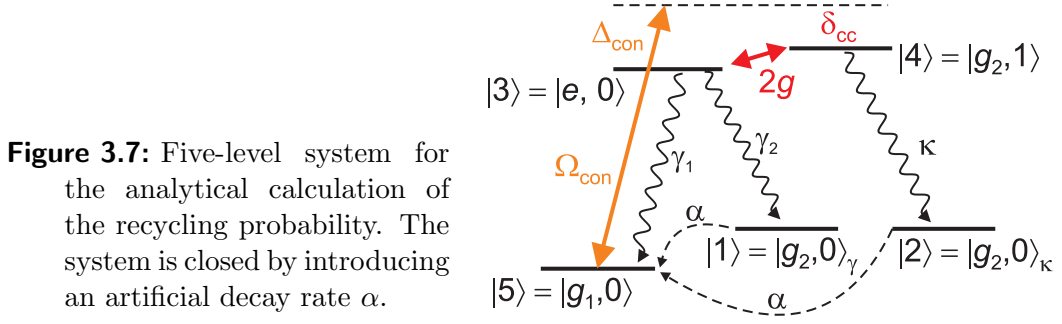
$$P_{\mathrm{rec}} = \int_0^\infty R_{\mathrm{p}} \, \mathrm{d}t = 2\kappa \int_0^\infty \mathrm{Tr}\left[\hat{a}^\dagger \hat{a} \hat{\rho}(t)\right] \, \mathrm{d}t. \tag{3.22}$$

A result of this numerical calculation is shown in Fig. 3.6(a). The recycling probability depends in a Lorentzian way on the two-photon detuning between control laser and cavity $\delta_{\mathrm{cc}} \equiv \Delta_{\mathrm{con}} - \Delta_{\mathrm{ca}}$ and is centered around $\delta_{\mathrm{cc}} = 0$, see Fig. 3.6(b). The total normalized transmission is then given by

$$\bar{T}_{\mathrm{ext}} = \bar{T}_{\mathrm{sc}} \times \left(1 + \frac{\omega_{\mathrm{p}}\chi''}{\kappa} \frac{\gamma_1}{\gamma_1 + \gamma_2} \frac{P_{\mathrm{rec}}}{2}\right), \tag{3.23}$$

which is in very good numerical agreement with the result of the quantum model.

Moreover, I have obtained an analytical expression for the recycling probability. I consider the steady-state of a five-level system, see Fig. 3.7. The states are the elements of the product basis of the atomic and the cavity states with at most one excitation. For instance, the vector $|e, 0\rangle$ represents the state with the atom in the excited state $|e\rangle$ and zero photons inside the cavity. When the system is initialized in state $|g_1, 0\rangle$ after a spontaneous decay due to γ_1, it stays in the manifold of the three coherently coupled states $\{|g_1, 0\rangle, |e, 0\rangle, |g_2, 1\rangle\}$ as long as no irreversible decay due to γ_2 or κ occurs. The latter case leads to a recycled photon, i.e. additional transmission. In any case the system will end up in $|g_2, 0\rangle$. To distinguish whether this state is reached either by spontaneous decay or by photon loss from the cavity, I split the final state into sub-states $|1\rangle = |g_2, 0\rangle_\gamma$ and $|2\rangle = |g_2, 0\rangle_\kappa$, respectively. For mathematical reasons, i.e. to find a *unique* steady-state after setting $\dot{\rho}_{\mathrm{ss}} = 0$, I

Figure 3.7: Five-level system for the analytical calculation of the recycling probability. The system is closed by introducing an artificial decay rate α.

closed the cycle by introducing an artificial decay rate α which connects the 'final' states with the initial state $|g_1, 0\rangle$. In steady state, the recycling probability is given by

$$P_{\text{rec}} = \frac{\rho_{22}}{\rho_{11} + \rho_{22}} , \tag{3.24}$$

where ρ_{11} and ρ_{22} denote the steady-state populations of the states $|1\rangle$ and $|2\rangle$, respectively. The analytical expressions for ρ_{11}, ρ_{22} have been obtained using *Mathematica*. Both expressions factorize into a common factor $f(\alpha)$ and an α-independent-part. Therefore, the ratio (3.24) does not depend on α any more. Alternatively, one can consider the limit $\alpha \ll (\kappa, \gamma)$, where only $|1\rangle$ and $|2\rangle$ are populated, i.e. $\rho_{11} + \rho_{22} \rightarrow 1$ and thus

$$P_{\text{rec}} = \lim_{\alpha \rightarrow 0} \rho_{22} . \tag{3.25}$$

In the opposite limit $\alpha \gg (\kappa, \gamma)$, the levels $|1\rangle$ and $|2\rangle$ are instantaneously depopulated. The five-level scheme reduces to a three-level scheme where the populations of $|3\rangle = |e, 0\rangle$ or $|4\rangle = |g_2, 1\rangle$ decay directly back to $|g_1, 0\rangle$ at rates 2γ or 2κ, respectively, see Fig. 3.8. In fact, this system is not closed in the sense that the sum of the populations of the three levels is conserved. There is irreversible loss of population from the manifold at a rate $2\gamma_2\rho_{33} + 2\kappa\rho_{44}$. The recycling probability is then given by the fraction that decays via the cavity mode:

$$P_{\text{rec}} = \frac{\kappa\rho_{44}}{\gamma_2\rho_{33} + \kappa\rho_{44}} . \tag{3.26}$$

In the limit of small control laser power $\Omega_{\text{con}} \ll (g, \gamma, \kappa)$, this system is mathematically equivalent to the standard case of a two-level atom inside a cavity which is probed by a weak laser. However, the roles of the cavity and the atom have been interchanged, because the atom is driven instead of the cavity.

To consider the other limit of α is just a different mathematical way to solve the problem. In any case, the full analytical result for the recycling probability is given by
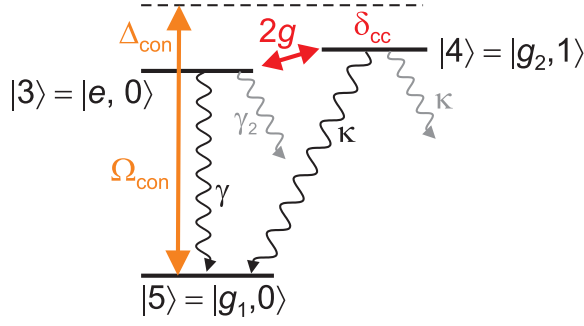
Figure 3.8: Open three-level system as a reduction of the five-level system in Fig. 3.7 in the limit $\alpha \gg (\kappa, \gamma)$. The irreversible population loss from this system is indicated by the gray arrows.

$$
\begin{aligned}
P_{\text{rec}} = {} & 4g^2\kappa \left(4\gamma\kappa\Delta_{\text{ca}}^2 + \lambda \left[4\left(g^2 + \gamma\kappa\right)\lambda + \gamma\Omega_{\text{con}}^2\right]\right) / \\
& \left\{16\left[g^2\kappa + \gamma_2\left(\kappa^2 + \delta_{\text{cc}}^2\right)\right]\left[\left(g^2 + \gamma\kappa\right)\lambda^2 + \gamma\kappa\Delta_{\text{ca}}^2\right]\right. \\
& \left. + 4\kappa\left(g^2\gamma\lambda + \gamma_2\left[\left(g^2 + 2\gamma\kappa\right)\lambda + 2\gamma\delta_{\text{cc}}\Delta_{\text{ca}}\right]\right)\Omega_{\text{con}}^2 + \gamma\kappa\gamma_2\Omega_{\text{con}}^4\right\},
\end{aligned}
$$

$$
\text{where} \quad \lambda = \kappa + \gamma. \tag{3.27}
$$

This result is plotted for different values of the control laser Rabi frequency Ω_{con} in Fig. 3.9. The resulting normalized transmission in the extended semiclassical model [Eqn. (3.23)] deviates from the result of the full numerical quantum simulation by less than 10^{-6} for the chosen set of parameters, compared to about 0.1 when using the semiclassical model, see last section.

With increasing Ω_{con}, the function (3.27) is shifted to lower values of δ_{cc} and its maximum value decreases. The position of the maximum is given by:

$$
\delta_{\text{cc,max}} = -\Omega_{\text{con}}^2 \times \frac{\gamma\kappa\Delta_{\text{ca}}}{4\left(\left(g^2 + \gamma\kappa\right)\lambda^2 + \gamma\kappa\Delta_{\text{ca}}^2\right)}. \tag{3.28}
$$

In the following I will discuss the analytical expression (3.27) in the limit of small control laser power (arbitrarily slow recycling), where it becomes much simpler:

$$
P_{\text{rec}} = \frac{g^2\kappa}{g^2\kappa + \gamma_2\left(\kappa^2 + \delta_{\text{cc}}^2\right)}. \tag{3.29}
$$

It represents a Lorentzian with a maximum value of

$$
P_{\text{rec,max}} = \frac{1}{1 + \kappa\gamma_2/g^2} \tag{3.30}
$$

at $\delta_{\text{cc}} = 0$ and a full-width-at-half-maximum of

$$
\Delta\delta_{\text{cc}} = 2\kappa\sqrt{1 + \frac{g^2}{\kappa\gamma_2}}. \tag{3.31}
$$

Note that both $P_{\text{rec,max}}$ and $\Delta\delta_{\text{cc}}$ depend on $g^2/(\kappa\gamma_2)$ which is a factor of γ/γ_2 times the single-atom-cooperativity $C_1 = g^2/(2\kappa\gamma)$. An expression equivalent to

Figure 3.9: The maximum recycling probability, calculated with Eqn. (3.27), decreases with increasing control laser Rabi frequency $\Omega_{\text{con}}/2\pi = 0.1, 5, 10\,\text{MHz}$.
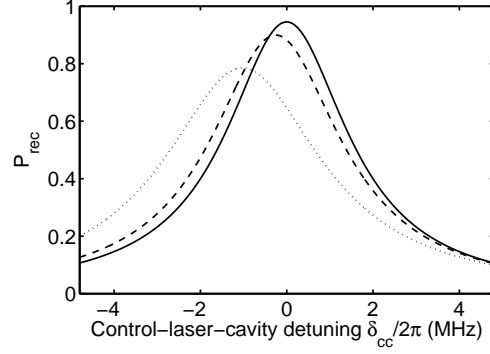
(3.30) has been obtained for the fractional emission of a four-level atom into the cavity mode compared to emission into free-space in the framework of single-atom lasing [88]. In the strong-coupling limit $g \gg (\kappa, \gamma)$ [4] and thus $C_1 \gg 1$, the maximum recycling probability becomes unity for all detunings.

Finally, I will estimate the strongest possible deviation of the semiclassical result (3.10) from the full quantum model for the normalized transmission, i.e. the second part in Eqn. (3.23):

$$\frac{\bar{T}_{\text{ext}} - \bar{T}_{\text{sc}}}{\bar{T}_{\text{sc}}} = \frac{\omega_{\text{p}} \chi''}{\kappa} \frac{\gamma_1}{\gamma_1 + \gamma_2} \frac{P_{\text{rec}}}{2} \,. \tag{3.32}$$

The imaginary part χ'' of the linear susceptibility (3.4) has a maximum value of

$$\chi''_{\text{max}} = \frac{2g^2}{\gamma\omega} \quad \text{for} \quad \delta \approx \frac{\Omega^2_{\text{con}}}{4\Delta_{\text{con}}} \,. \tag{3.33}$$

With $P_{\text{rec}} \to 1$ in the strong-coupling limit and assuming a branching ratio such that $\gamma_1 \approx \gamma$, I obtain a maximum modification of the semiclassical transmission by:

$$\bar{T}_{\text{ext,max}} = \bar{T}_{\text{sc}} \times \left(1 + \frac{g^2}{\kappa\gamma}\right) = \bar{T}_{\text{sc}} \times (1 + 2C_1) \,. \tag{3.34}$$

This is a remarkable result because it implies that in the strong-coupling-regime the transmission of a cavity filled with a three-level medium is not simply given by the absorptive and dispersive properties of this medium, using the cavity just as a passive 'phase-to-amplitude' converter. In free space, those properties would be sufficient to describe the propagation of a weak probe beam through the medium. Scattered photons would be irreversibly lost from the mode of the probe beam. In contrast, inside a high-finesse optical cavity, the coherent atom-light coupling g can become much stronger than the incoherent rates κ, γ. In the strong coupling regime, there is a significant probability that this excitation is coherently transferred back into the cavity mode by a stimulated Raman process driven by the control laser and the cavity mode. It is closely related to the Purcell effect [81], the enhanced spontaneous emission of an atom into the cavity mode. However, the 'secondary' photons generated in this process have in general a different energy

than the 'primary' probe photons: In the limit of a small control laser power, the energy of the secondary photons is by $-\hbar\delta$ different from the energy of the primary ones. In principle, one could distinguish them by spectroscopic means.

These considerations are valid for a *single* atom inside the cavity so far. Here, the scaling parameter is obviously the *single*-atom-cooperativity C_1. For more than one atom, however, it doesn't seem to be straightforward to replace g in Eqns. (3.27–3.34) by the collective coupling strength $g\sqrt{N}$ and thus C_1 by NC_1: The full quantum simulation does not agree with the extended model for $N > 1$ when those simple replacements are made. There are presumably higher-order contributions due to atom-atom interactions, mediated by the cavity field. However, a theoretical investigation would go far beyond the scope of this thesis.

3.5 Few Multilevel Atoms

For a more realistic treatment of cavity EIT, one has to take into account additional excited hyperfine states, and, in the case of more than one atom, the multi-atom spin dynamics: One cannot just treat multiple atoms as one atom with a higher coupling strength once probe and control power are of the same order of magnitude and population can be transferred from state $|g_2\rangle$ to state $|g_1\rangle$. To illustrate this, let's compare the situation of N atoms, each coupled with g to the cavity field, with one atom coupled more strongly with a coupling strength of $g\sqrt{N}$: In the weak-excitation limit, the normalized transmission according to Eqn. (3.10) and thus the intracavity photon number n_{p} would be equal in both cases. The total scattering rate and thus the probability for an atom to undergo a quantum jump from $|g_2\rangle$ to state $|g_1\rangle$ is $P \propto n_{\mathrm{p}}g^2$. If we assume a small, but finite value of P, the probability that *one* out of the N atoms changes its state is almost as high as the probability NP that the more strongly coupled atom changes its state. But in the multi-atom case, there would be still $N - 1$ atoms left in state $|g_2\rangle$ which suppress the cavity transmission and the intracavity photon number would not increase as much as in the effective one-atom case.

The basic quantum model described in section 3.3 has to be extended by additional terms, yielding the total Hamiltonian of the system:

$$\hat{H}_{\mathrm{tot}} = \hat{H}_{\mathrm{cavity}} + \sum_{m=1}^{N} \left[\hat{H}_{\mathrm{atom}}^{(m)} + \hat{H}_{\mathrm{int}}^{(m)} \right], \tag{3.35}$$

$$\text{where} \quad \hat{H}_{\mathrm{atom}}^{(m)} = -\hbar\delta\hat{\sigma}_{g_1g_1}^{(m)} + \hbar \sum_{k=c,d,e,f} (\Delta_{ke} - \Delta_{\mathrm{p}})\hat{\sigma}_{kk}^{(m)},$$

$$\hat{H}_{\mathrm{int}}^{(m)} = \frac{i\hbar}{2} \sum_{k=c,d,e} \Omega_{\mathrm{con}}^{(k)} \left[\hat{\sigma}_{kg_1}^{(m)} - \hat{\sigma}_{g_1k}^{(m)} \right] + i\hbar \sum_{k=d,e,f} g_k \left[\hat{\sigma}_{kg_2}^{(m)}\hat{a} - \hat{\sigma}_{g_2k}^{(m)}\hat{a}^\dagger \right],$$

where $\hat{\sigma}_{kl}^{(m)} \equiv |k\rangle^{(m)}\langle l|^{(m)}$ only acts on the m-th atom. The indices c, d, e, f denote the exited $|F' = 2, 3, 4, 5\rangle$ hyperfine states, and $\Delta_{ke} \equiv \omega_k - \omega_e$ are the energies of
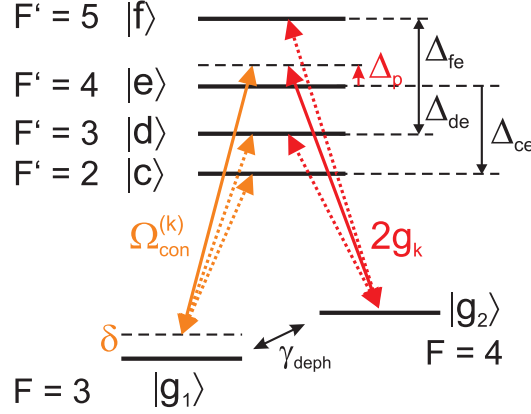
Figure 3.10: Six-level atomic scheme, including all states of the caesium $^2S_{1/2}$ and $^2P_{3/2}$ hyperfine manifold.

the states $|k\rangle$ with respect to the state $|e\rangle$, see Fig. 3.10. The control laser Rabi frequencies for the $|g_1\rangle \leftrightarrow |k\rangle$ transitions are denoted by Ω_{con}^k and the atom-cavity coupling strengths for the $|g_2\rangle \leftrightarrow |k\rangle$ transitions are denoted by g_k.

For the sake of simplicity, the Zeeman substates are not taken into account in this model. Therefore, I assume isotropic pumping fields with equal components in all three possible polarizations where the coupling to the atom is independent on the distribution of population among the sublevels [80], thus neglecting effects of optical pumping in our system [38]. By summing up the dipole matrix elements from a single ground-state Zeeman sublevel of an $|F\rangle$ to all sublevels of a particular $|F'\rangle$-level, one obtains a measure $S_{FF'}$ of the relative strength of the $|F\rangle \leftrightarrow |F'\rangle$-transitions. The atoms can be treated as two-level systems, with an effective dipole moment given by [80]:

$$|d_{\text{iso,eff}}(F \to F')|^2 = \frac{1}{3}S_{FF'}|\langle J\|e\vec{r}\|J'\rangle|^2, \tag{3.36}$$

where $\langle J|e\vec{r}\|J'\rangle = 4.484\,ea_0$ is the reduced dipole matrix element for the Cs-D$_2$-line ($J = 1/2$, $J' = 3/2$). The coupling strengths $\Omega_{\text{con}}^{(k)}$ and g_k are then proportional to the corresponding $(S_{FF'})^{1/2}$, and relative decay probabilities $\gamma_{1,2}^{(k)}/\gamma$ are proportional to $S_{FF'}$. The results, with $\Omega_{\text{con}}^{(k)}, g_k$ normalized on the coupling strengths Ω_{con}, g for the three-level system, are listed in table 3.1.

3.6 Optimization

The Hilbert space in a numerical simulation has a finite dimension and is spanned by the product basis of n_{lev} atomic and n_{cav} cavity states that are taken into account. At a typical mean intracavity photon number of $\bar{n}_{\text{p}} = 0.1$, it is sufficient for our

$|k\rangle$	F'	Δ_{ke}/MHz	$\Omega_{\mathrm{con}}^{(k)}/\Omega_{\mathrm{con}}$	g_k/g	$\gamma_1^{(k)}/\gamma$	$\gamma_2^{(k)}/\gamma$
$|c\rangle$	2	-352.51	$\sqrt{4/3}$	0	1	0
$|d\rangle$	3	-201.29	$\sqrt{7/5}$	$\sqrt{1/3}$	27/34	7/34
$|e\rangle$	4	0	1	1	45/94	49/94
$|f\rangle$	5	251.09	0	$\sqrt{44/21}$	0	1

Table 3.1: Normalized coupling strengths $\Omega_{\mathrm{con}}^k/\Omega_{\mathrm{con}}$ and g_k/g for the transitions $|g_1\rangle \leftrightarrow |k\rangle$ and $|g_2\rangle \leftrightarrow |k\rangle$, respectively, and relative decay probabilities γ_1^k/γ and γ_1^k/γ from $|k\rangle$ into $|g_1\rangle$ and $|g_2\rangle$, respectively.

purposes to incorporate $n_{\mathrm{cav}} = 3$ cavity states (0, 1, 2 photon Fock states)[3]. The product basis

$$|\Psi\rangle = |k\rangle_1 \otimes |k\rangle_2 \otimes \cdots \otimes |k\rangle_N \otimes |n\rangle = |k_1 k_2 \ldots k_N n\rangle, \qquad (3.37)$$
$$\text{where} \quad |k\rangle_i \in \{|g_1\rangle, |g_2\rangle, |c\rangle, |d\rangle, |e\rangle, |f\rangle\}$$

is the state of the i-th atom, consists of $\dim_{\mathrm{H}} = n_{\mathrm{lev}}^N \cdot n_{\mathrm{cav}}$ basis states, scaling exponentially with the number of atoms. The density matrix operator $\hat{\rho}$ has $\dim_{\mathrm{H}}^2$ elements, and the linear superoperators appearing in the master equation and describing the time evolution of $\hat{\rho}$, even have $\dim_{\mathrm{H}}^4$ elements. This means that the computational load which is required to solve the master equation can be enormous even for a small number of atoms: For example, with $n_{\mathrm{cav}} = 3$ and $n_{\mathrm{lev}} = 6$ the superoperators have about 10^5 elements for one atom, 10^8 for two and 10^{11} for three atoms.

To reduce the computational load, one would like to reduce the dimension of the Hilbert space by taking into account a smaller number of atomic levels explicitly. The interaction of light with closed, far-detuned transitions can be incorporated into the model by adding the resulting light shifts as effective detunings:

In our case, the closed $|g_1\rangle \leftrightarrow |c\rangle$ transition is far detuned compared to the linewidth but still much closer to the control laser frequency than the probe laser or cavity frequencies. Therefore, the only effect one has to consider is a differential light shift caused by the control laser that changes the energy splitting between the two ground states. The two-photon-detuning δ in Eqn. (3.35) can be replaced by an effective two-photon-detuning

$$\delta_{\mathrm{eff}} = \delta - \frac{(\Omega_{\mathrm{con}}^{(c)})^2}{4\Delta_c}, \qquad (3.38)$$
$$\text{where} \quad \Delta_c \equiv (\Delta_{\mathrm{con}} - \Delta_{ce}) \gg \Omega_{\mathrm{con}}^{(c)}$$

denotes the detuning of the control laser from the $|g_1\rangle \leftrightarrow |c\rangle$ transition. In this way, the state $|c\rangle$ can be removed from the model.

---

[3]Assuming a coherent state, i.e. a poissonian distribution, the population of all higher Fock states is below $2 \cdot 10^{-4}$.

The state $|f\rangle$ can be eliminated in a similar way: The dispersive interaction of the closed $|g_2\rangle \leftrightarrow |f\rangle$ transition with the cavity field leads to an effective detuning of the probe laser from the cavity frequency when the atoms are in state $|g_2\rangle$. The probe-cavity detuning Δ_{pc} in Eqn. (3.35) can be replaced by an effective probe-cavity detuning

$$\Delta_{\mathrm{pc}}^{\mathrm{eff}} = \Delta_{\mathrm{pc}} + \frac{g_f^2}{\Delta_f} \sum_{m=1}^N \hat{\sigma}_{g_2 g_2}^{(m)}, \tag{3.39}$$

$$\text{where} \quad \Delta_f \equiv (\Delta_{ef} + \Delta_{\mathrm{pc}} - \Delta_{\mathrm{p}}) \gg g_f$$

denotes the detuning of the cavity from the $|g_2\rangle \leftrightarrow |f\rangle$ transition.

These simplifications have been checked numerically for typical experimental parameters, i.e. that the deviations from the 'full' model (3.35) are small compared to the experimental uncertainties, see chapter 4. It has turned out that eliminating also state $|d\rangle$ is much more difficult since it couples to both ground states, hence population can be transferred between them via this excited state. However, now dealing with effective four-level systems, the computational load has already significantly decreased: The number of elements of the superoperators is about 2×10^4 for one, 5×10^6 for two and 10^9 for three atoms. However, in the latter case, this was still too much to be computed on a single machine in a reasonable amount of time!

4 Transmission measurements of EIT in the optical cavity

In this chapter I report on our experimental observation of EIT with a single atom inside the optical cavity [30]. After a description of the specific experimental configuration with estimations on the key parameters, I will present the measurement procedure. The experimental results are then discussed by comparing them with different theoretical models.

4.1 Setup

For the detection of EIT in the transmission of the optical resonator, we transport a small number the atoms to the center of the cavity mode using the optical conveyor belt. The transmission of a weak probe laser beam, which is coupled to the cavity mode and is resonant with the empty cavity frequency, is detected by a single photon counting module (SPCM), see Fig. 4.1 (a).
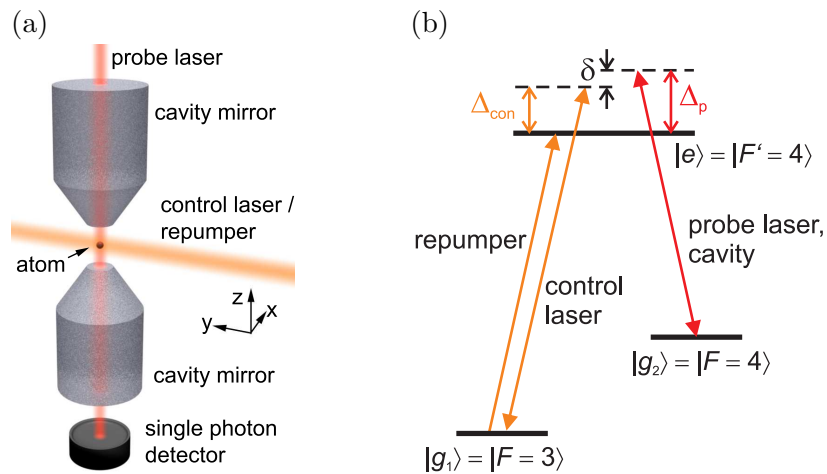

Figure 4.1: (a) Schematic experimental setup. A single atom is placed between the mirrors of the high-finesse cavity and illuminated from the side by a control laser and a repumper. The transmission of a weak probe laser beam is detected by a single photon counting module. (b) Scheme of the relevant levels, laser and cavity detunings.
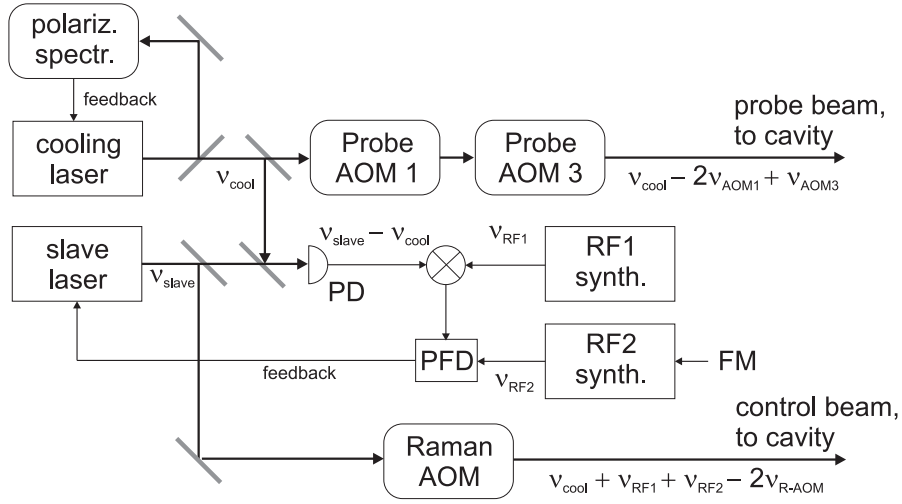
Figure 4.2: Locking scheme for the probe and the control laser beams. PD: photo diode; PFD: phase/frequency discriminator; FM: frequency modulation.

The atoms can be irradiated from the side with two different near-resonant laser beams — a control laser and a repumper beam — both propagating along the axis of the standing-wave optical dipole trap (conveyor belt), orthogonal to the cavity axis. The control laser beam can be tuned around the two-photon resonance ($\delta = 0$) with the probe laser, which is blue-detuned from the $|F = 4\rangle \leftrightarrow |F' = 4\rangle$ transition and resonant with the cavity, see Fig. 4.1 (b). The repumper laser beam, resonant with the $|F = 3\rangle \leftrightarrow |F' = 4\rangle$ transition is needed to check the coupling of atoms in $|F = 4\rangle$ to the cavity mode

4.1.1 Modified Raman laser setup

In order to realize a coherent two-photon process, the frequency of the control laser needs to be stabilized with respect to the probe laser. Any fluctuations of the frequency difference translate into fluctuations of the two-photon detuning δ, decreasing the resolution of the EIT measurement and causing also ground-state dephasing. To achieve this stability, we use one of the two lasers (the 'slave laser') of our the Raman laser setup (see section 1.3.2; for details, see [48]) as the control laser by phase-locking it on the cooling laser with frequency ν_{cool}, see Fig. 4.2. The latter is in turn stabilized on the crossover signal of the $|F = 4\rangle \leftrightarrow |F' = 3\rangle$ and $|F = 4\rangle \leftrightarrow |F' = 5\rangle$ transitions in a cesium polarization spectroscopy, such that

$$\nu_{\text{cool}} = \nu_{44'} + \Delta\nu_{\text{cr}}, \tag{4.1}$$

where $\nu_{44'}$ denotes the $|F = 4\rangle \leftrightarrow |F' = 4\rangle$ transition frequency which is $\Delta\nu_{\text{cr}} = 24.90\,\text{MHz}$ smaller the crossover transition frequency. The cooling laser light is frequency-shifted by two acousto-optical modulators 'Probe AOM1' and 'Probe
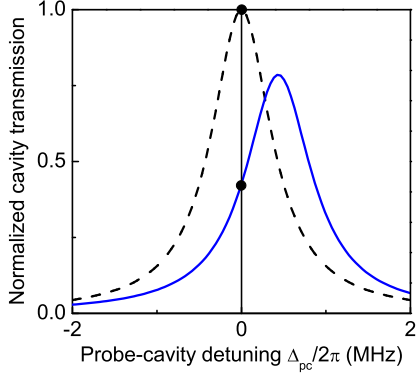
Figure 4.3: Calculated cavity transmission function for zero (dashed line) one atom (solid line) in state $|F = 4\rangle$ inside the cavity. The normalized transmission of the probe laser through the cavity drops to about 50% of its initial value when the probe laser is kept on resonance with the empty cavity ($\Delta_{\mathrm{pc}} = 0$).

AOM3' before it is coupled into the cavity mode as a probe beam. The AOMs are running in a -1st order double-pass and a $+1$st order single-pass configuration, respectively. The frequency of the probe light is then given by

$$\begin{aligned}
\nu_{\mathrm{p}} &= \nu_{\mathrm{cool}} - 2\nu_{\mathrm{AOM1}} + \nu_{\mathrm{AOM3}} \\
&= \nu_{44'} + \Delta\nu_{\mathrm{cr}} - 2\nu_{\mathrm{AOM1}} + \nu_{\mathrm{AOM3}} \,,
\end{aligned} \tag{4.2}$$

where ν_{AOM1} and ν_{AOM3} denote the RF driving frequencies of the AOMs.

Due to the phase-lock, the slave laser is running at the sum frequency of the cooling laser and the radio frequencies $\nu_{\mathrm{RF1,2}}$ of the two RF synthesizers. For fast frequency sweeps during the measurement of the EIT transmission signal, the analog frequency modulation input 'FM' is used, allowing to change the slave laser frequency ν_{con} and thereby δ by at most $\pm 1.3\,\mathrm{MHz}$. To switch the control laser beam inside our vacuum cell rapidly on and off, we use a 'Raman AOM' in a -1st order double-pass configuration. The resulting frequency of the control laser light is

$$\begin{aligned}
\nu_{\mathrm{con}} &= \nu_{\mathrm{cool}} + \nu_{\mathrm{RF1}} + \nu_{\mathrm{RF2}} - 2\nu_{\mathrm{R\text{-}AOM}} \\
&= \nu_{44'} + \Delta\nu_{\mathrm{cr}} + \nu_{\mathrm{RF1}} + \nu_{\mathrm{RF2}} - 2\nu_{\mathrm{R\text{-}AOM}} \,,
\end{aligned} \tag{4.3}$$

where $\nu_{\mathrm{R\text{-}AOM}}$ denotes the driving frequency of the Raman AOM.

4.2 Preparation

4.2.1 Configuration of the transmission measurement

The optimal probe-atom detuning as well as the probe laser power for the EIT transmission measurement are determined in a preparatory measurement. For this, the repumper is switched on in order to realize an effective two-level system, because the repumper and the probe are far detuned $\delta \gg \gamma$ from the two-photon resonance. In this limit, the transmission of the probe laser through the cavity is related to the coupling strength g by the two-level approximation, Eqn. (3.12).

For a probe-atom (cavity-atom) detuning of $\Delta_\mathrm{p}/2\pi \approx 20\,\mathrm{MHz}$, we observe the most stable coupling and longest lifetime of the atoms, whereas for $\Delta_\mathrm{p} \lesssim 0$, we observe an increase in atom losses. For larger detunings, the reduction of the transmission when atoms are coupled to the cavity decreases. Concerning the probe laser power, we find that an empty-cavity photon count rate of $R_\mathrm{D} = 10\,\mathrm{ms}^{-1}$ is a good compromise between low atom losses and a good signal-to-noise ratio. This count rate corresponds to a mean intracavity photon number of $n_\mathrm{p,0} = 0.07$, see Eqn. (1.8).

For these settings, the transmission of the probe beam through the cavity drops to about 50% of the empty cavity value when a single atom in state $|F = 4\rangle$ couples to the cavity mode. In that particular case, we are most sensitively to changes in the refractive index of the atom, since the probe laser is situated on the steep slope of the cavity transmission function, see Fig. 4.3. The transmission reduction can be explained by both the dispersive effect of the atom, shifting the cavity resonance to higher frequencies, and the absorptive effect, reducing the overall transmission.

4.2.2 Experimental parameters

For the quantitative modelling of the system, the key parameters for the EIT measurements such as Rabi frequencies and detunings are important. They can be independently inferred from, e.g. the intensities of the control- and dipole trap laser beams at the position of the atoms.

Control laser Rabi frequency

The control laser, which is near resonant with the $|F = 3\rangle \leftrightarrow |F' = 4\rangle$ transition, couples the two hyperfine states with an effective Rabi frequency

$$\Omega_\mathrm{con,eff}^{34'} \equiv d_\mathrm{iso,eff}^{34'} E_0/\hbar\,, \tag{4.4}$$

with the electric field amplitude at the center of the laser beam

$$E_0 = 2\sqrt{\frac{P_\mathrm{con}}{c\epsilon_0 \pi w_\mathrm{con,cav}^2}}\,. \tag{4.5}$$

There, P_con denotes the power and $w_\mathrm{con,cav} = 86\,\mu\mathrm{m}$ the waist of the control laser beam at the cavity position [48]. The effective dipole moment $d_\mathrm{iso,eff}^{34'} = 1.136 \times 10^{-29}\,\mathrm{Cm}$ is on assumption of a homogeneous distribution over m_F-sublevels, averaging over different Clebsch-Gordan coefficients, for details see section 3.5.

For a typical power of $P_\mathrm{con} = 1\,\mu\mathrm{W}$, I obtain $E_0 = 255\,\mathrm{V/m}$, yielding

$$\Omega_\mathrm{con,eff}^{34'}/2\pi = 4.4\,\mathrm{MHz}. \tag{4.6}$$

For specific transitions between $|F = 3, m_F\rangle$ and $|F' = 4, m_F'\rangle$ sublevels, the dipole moment ranges from $0.33 \times 10^{-29}\,\mathrm{Cm}$ to $1.73 \times 10^{-29}\,\mathrm{Cm}$ [80], corresponding to a control laser Rabi frequency between 1.3 and 6.7 MHz.

Atom-cavity coupling strength

Analogous to the effective control laser Rabi frequency, an effective coupling strength for the $|F = 4\rangle \leftrightarrow |F' = 4\rangle$ transition can be defined. Under the assumption of a homogenous distribution over m_F-sublevels, this coupling strength is given by (cf. Eqn. (1.7))

$$g_{\mathrm{eff}}^{44'} = d_{\mathrm{iso,eff}}^{44'} \sqrt{\frac{\omega}{2\hbar\epsilon_0 V_{\mathrm{mode}}}} \, , \tag{4.7}$$

where $d_{\mathrm{iso,eff}}^{44'} = 1.185 \times 10^{-29}$ Cm is the corresponding effective dipole moment [80]. From the last equation, I obtain an effective coupling strength of

$$g_{\mathrm{eff}}^{44'}/2\pi = 7.9\,\mathrm{MHz}. \tag{4.8}$$

This value serves only as a reference number that will later be needed to compare the fit results of different models. In contrast to other definitions of effective coupling strengths that are related to the thermal motion of the atoms [38], I assume here that the atom is located at an antinode of the probe standing wave.

Single-photon and two-photon detunings

The single-photon detunings are given by the differences between the laser frequencies $\nu_{\mathrm{p}}, \nu_{\mathrm{con}}$ and the atomic transition frequencies which are light-shifted due to the dipole trap. The light shift of an optical transition $|g\rangle \leftrightarrow |e\rangle$ is defined as

$$\Delta_{\mathrm{ls}}^{ge} \equiv (\Delta E_e - \Delta E_g)/h, \tag{4.9}$$

where ΔE_g and ΔE_e denote the energy shifts of the atomic ground and exited states, respectively. The single-photon detunings are defined as

$$\Delta_{\mathrm{p}}/2\pi \equiv \nu_{\mathrm{p}} - \nu_{44'} - \Delta_{\mathrm{ls}}^{44'}, \tag{4.10}$$

$$\Delta_{\mathrm{con}}/2\pi \equiv \nu_{\mathrm{con}} - \nu_{34'} - \Delta_{\mathrm{ls}}^{34'} = \nu_{\mathrm{con}} - \nu_{44'} - \Delta\nu_{\mathrm{HFS}} - \Delta_{\mathrm{ls}}^{34'}, \tag{4.11}$$

where $\nu_{34'}$ denotes the frequency of the un-shifted $|F = 3\rangle \leftrightarrow |F' = 4\rangle$ transition and $\Delta\nu_{\mathrm{HFS}} = \nu_{34'} - \nu_{44'} = 9192.631770\,\mathrm{MHz}$ is the ground-state hyperfine splitting of cesium.

In contrast to the single-photon detunings, the two-photon detuning does neither depend on absolute transition and laser frequencies nor on *common* light shifts:

$$\delta/2\pi \equiv (\Delta_{\mathrm{p}} - \Delta_{\mathrm{con}})/2\pi = \nu_{\mathrm{p}} - \nu_{\mathrm{con}} + \Delta\nu_{\mathrm{HFS}} + \delta_{34}, \tag{4.12}$$

where $\delta_{34} \equiv \Delta_{\mathrm{ls}}^{44'} - \Delta_{\mathrm{ls}}^{34'}$ denotes the *differential* light shift between the two ground states. In our experimental sequence, δ is varied by changing the control laser frequency ν_{con}. This is technically done according to Eqn. (4.3) by changing ν_{RF2}.

The energy shift ΔE_g of the ground states, which is closely related to the dipole trap depth $U_0(y)$, is inferred from a measurement of the axial trap frequency $\nu_{\mathrm{ax}}(y = 0) = (220 \pm 2)\,\mathrm{kHz}$ at the MOT position, for details see section 5.3.1.
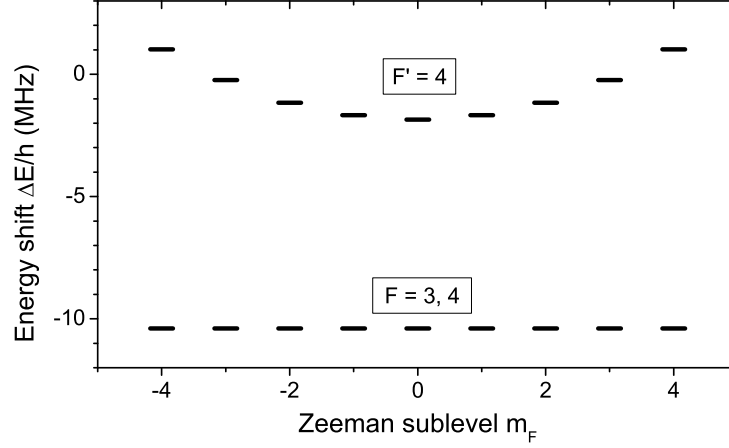
Figure 4.4: Calculated energy shifts due to the linearly polarized dipole trap beams. The Zeeman sublevels of the $|F = 3\rangle$ and $|F = 4\rangle$ ground states are shifted almost equally, while the sublevels of the $|F' = 4\rangle$ excited state show a quadratic dependence.

Using Eqns. (5.17)–(5.15), I obtain $U_{0,\text{MOT}} = h \times (9.5 \pm 0.2)\,\text{MHz}$. Since the trap depth is inversely proportional to $w_{\text{DT}}^2(y)$, I obtain for the energy shift at the cavity position

$$\Delta E_g = -U_{0,\text{cav}} = -U_{0,\text{MOT}} \times \frac{w_{\text{DT,MOT}}^2}{w_{\text{DT,cav}}^2} = -h \times (10.4 \pm 0.2)\,\text{MHz}. \qquad (4.13)$$

Assuming pure linear polarization of the standing-wave dipole trap beams, one can now calculate the energy shifts also for the $|F' = 4\rangle$ excited state manifold according to [39], see Fig. 4.4. While the energy shifts ΔE_g and with it the trap depths are practically equal for both hyperfine ground states and their sublevels (i.e. $\delta_{34} \ll \Delta E_g$), the energy shifts of the excited states range from -1.9 to $+1.0\,\text{MHz}$ for $|m_F'| = 0, \ldots, 4$. The resulting light shifts Δ_{ls} of the optical transitions range from $+8.5$ to $+11.4\,\text{MHz}$.

For typical values of the radio frequencies, one can now calculate the single- and two-photon detunings (in MHz):

ν_{AOM1}	ν_{AOM3}	ν_{RF1}	ν_{RF2}	$\nu_{\text{R-AOM}}$	$\Delta_{\text{p}}/2\pi$	$\Delta_{\text{con}}/2\pi$	$\delta/2\pi$
117	240	9290	66	79	$22\ldots 20$	$22\ldots 20$	0

The differential light shift δ_{34} between the outermost Zeeman states $|F = 3, m_F = -3\rangle$ and $|F = 4, m_F = -4\rangle$ induced by the dipole trap is measured using microwave spectroscopy at the position of the MOT. When we change the total dipole trap power by $\Delta P = 0.9\,\text{W}$, the transition frequency between the two states changes by $\delta_{34,\text{MW}}/2\pi \approx 5\,\text{kHz}$. By extrapolation, I estimate the differential light shift at the
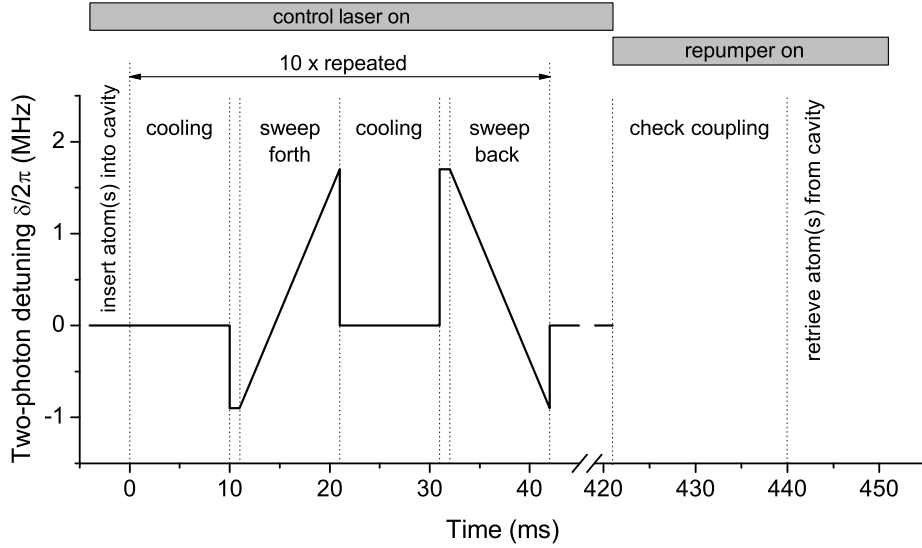
Figure 4.5: Main part of the EIT transmission measurement sequence. After insertion of atoms into the cavity, there are alternating cooling and measurement cycles. The coupling is checked at the end of the sequence. The short time intervals right before the detuning sweeps are needed for a relaxation of the control loop.

position of the cavity, yielding

$$|\delta_{34}| \le \delta_{34,\mathrm{MW}} \times \frac{P}{\Delta P} \times \frac{w_{\mathrm{DT,MOT}}^2}{w_{\mathrm{DT,cav}}^2} \approx 2\pi \times 22\,\mathrm{kHz}, \qquad (4.14)$$

where $P = 3.6\,\mathrm{W}$ is the full dipole trap power. According to [39], one would expect a differential light shift between those states of about $3\,\mathrm{kHz}$ for purely linearly and about $4.3\,\mathrm{MHz}$ for purely circularly polarized dipole trap beams. The value (4.14) can be explained by a small admixture of circularly polarized light in our dipole trap on the order of $1\,\%$ of the total power.

4.3 Main experimental sequence

The main part of the sequence for the measurement of the EIT transmission signals is shown in Fig. 4.5. The sequence starts with the insertion of a pre-selected number of atom(s) into the cavity mode and consists of cooling and measurement cycles. The arrival time of each photon which is detected by the SPCM is recorded with a time resolution of $50\,\mathrm{ns}$ using a timer card. The photon clicks which have been

recorded during the sweeps are binned to time intervals of $0.2\,\mathrm{ms}$, corresponding to intervals of the two-photon-detuning δ of $2\pi \times 52\,\mathrm{kHz}$, which turns out to be a good compromise between a high spectral resolution and a good signal-to-noise ratio.

We have observed that the atoms are cooled or heated at certain values of the two-photon detuning δ, as is described in more detail in chapter 5. This can significantly change the atom-cavity coupling strength g over the sweep or even heat the atom(s) out of the trap. To minimize this effect, we quickly sweep through the accessible range of δ, and additionally record a reversed sweep to compensate also for effects that depend on the sweep direction. To counteract the heating that occurs during the sweeps, we alternate them with cooling periods at $\delta = 0$. The cooling increases the avarage number of measurement cycles before the atoms are heated out of the trap by a factor of five.

After ten repetitions, the coupling of the atom(s) to the cavity mode is checked by switching the control laser off and the repumper on instead. This data will be used in the post-selection process described below.

Post-selection

After applying the main part of the sequence as described above, the atoms are retrieved from the cavity and counted again. We post-select data traces with no atom losses and strong coupling of all atoms to the cavity mode. For this, we first check whether the relative cavity transmission at the end of each sequence $(421 \ldots 440\,\mathrm{ms})$ is below 70% or not. From this, we deduce whether the transport of atom(s) into the cavity has worked or not. For one atom, this criterion is already sufficient.

However, two or more atoms can have significantly large distances (compared to the cavity mode waist $w_{0,\mathrm{cav}}$) among each other. Therefore, if $N > 1$ we also need to analyze a fluorescence image (see Fig. 1.1] [53] taken at the beginning of each sequence and check if the atoms are well positioned within the cavity mode, i.e. that their average position-dependent coupling

$$\bar{g} \equiv \sqrt{\frac{1}{N} \sum_{i=1}^{N} g_i^2} \tag{4.15}$$

is at least 95% of the maximum value g_0 at the center of the cavity mode. Here, r_i denotes the distance of the i-th atom from the cavity center and g_i its position-dependent coupling strength

$$g_i = g_0 \exp\left(-\frac{r_i^2}{w_{0,\mathrm{cav}}^2}\right) . \tag{4.16}$$
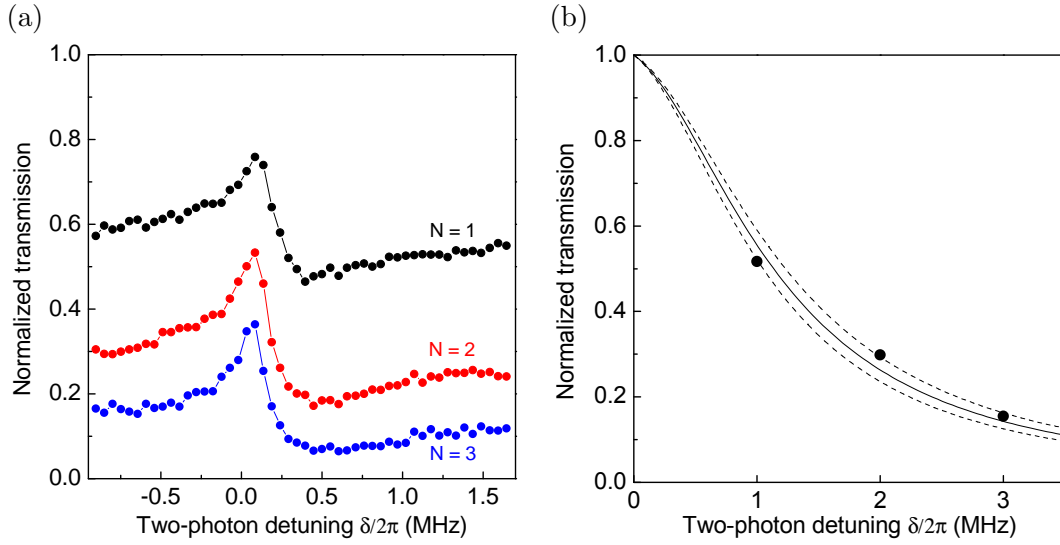
(a)

(b)

Figure 4.6: (a) Normalized cavity transmission as a function of the two-photon detuning δ, for $N = 1, 2, 3$ atoms. The statistical error of the data is smaller than the size of the circles. (b) Normalized cavity transmission as a function of the atom number N, at the end of the sequence where the repumper switched on. The solid line is the transmission calculated using the semiclassical formula (3.12) with $g/2\pi = \sqrt{N} \times 2.5$ MHz. The dashed lines correspond to $g/2\pi = \sqrt{N} \times 2.4$ MHz and $g/2\pi = \sqrt{N} \times 2.6$ MHz, respectively.

4.4 Results and discussion

4.4.1 EIT with different atom numbers

The EIT transmission is measured with different numbers of atoms inside the cavity to vary the collective coupling strength according to $g \propto \sqrt{N}$. According to the semiclassical model presented in section 3.2, the linear susceptibility $\chi^{(1)}$ and thus the phase shift and the absorption of probe light by the atom(s) are proportional to $g^2 \propto N$, see Eqn. (3.4).

For this type of measurement, the main sequence is always triggered if one, two or three atoms have been loaded into the MOT. This ensures that all three signals are effectively measured at the same time instead of pre-selecting first one atom, then two atoms, and so on. This speeds up the whole process and avoids long-term drifts of the experimental conditions.

Measurement result

The result of the measurement with different atom numbers is shown in Fig. 4.6 (a). For each atom number N, about 100 experimental shots, i.e. about 2000 single detuning sweeps of 10 ms each, have been averaged.

The experimental data exhibit a dispersive signal, consisting of a transmission maximum close to the two-photon resonance followed by a minimum about $250\,\mathrm{kHz}$ away. With increasing atom number N, the overall transmission and especially the transmission level for large values of $|\delta|$ decreases. A similar dependence can be observed for the cavity transmission at the end of the sequence, see Fig. 4.6 (b), when the repumper is switched on, i.e. far from the two-photon resonance. The atom-number-dependent transmission can be described by the semiclassical formula (3.12) for an effective two-level system with a coupling strength of $g/2\pi = \sqrt{N} \times (2.5 \pm 0.1)\,\mathrm{MHz}$.

Semiclassical interpretation

The shape of the transmission signal can be qualitatively interpreted in terms of the manipulation of the complex refractive index n_{ref} of a three-level atomic medium inside an optical cavity. The complex linear susceptibility $\chi^{(1)}(\omega_{\mathrm{p}})$, closely related to n_{ref} by Eqn.(3.5), is a direct measure for the dispersive and absorptive effects of a medium on the propagation of light.

In figure 4.7(a), the real and imaginary parts of $\chi^{(1)}(\omega_{\mathrm{p}})$ of one atom coupled with $g/2\pi = 3\,\mathrm{MHz}$ to the mode of an optical cavity are shown for a fixed control laser detuning of $\Delta_{\mathrm{con}}/2\pi = 20\,\mathrm{MHz}$ and a Rabi frequency of $\Omega_{\mathrm{con}}/2\pi = 4.4\,\mathrm{MHz}$. There is one broad resonance at $\delta \approx -\Delta_{\mathrm{con}}$ and one narrow resonance at $\delta \approx 0$, corresponding to dressed states $|-\rangle$ and $|+\rangle$, respectively. The latter are created by the off-resonant coupling of the ground state $|g_1\rangle = |F = 3\rangle$ and the excited state $|e\rangle = |F' = 4\rangle$ by the control laser. The susceptibility around the broad resonance $|-\rangle$ is nearly identical to that of a two-level atom. The state $|-\rangle$ has a large contribution from $|e\rangle$ and thus a width comparable with the natural line width Γ.

Much more interesting is the shaded region around the Fano-like [85] narrow resonance $|+\rangle$ and the two-photon resonance, see Fig. 4.7(b): Within a range of δ small compared to Γ, the susceptibility and thus the transmission of a probe laser resonant with the empty cavity (i.e. $\Delta_{\mathrm{pc}} = 0$) change dramatically. The small insets (i) – (vi) illustrate the effect of six particular values of $\chi^{(1)}$ appearing in this region on the cavity transmission function:

At $\delta = 0$, both absorption and dispersion vanish due to the EIT effect. Consequently, the corresponding transmission function (ii) is that of an empty cavity and thus the normalized transmission of the probe laser is unity.

The semiclassical model [Eqn. (3.4)] shows an absorption peak at a two-photon detuning of

$$\delta_{\mathrm{abs}} \approx \Omega_{\mathrm{con}}^2/(4\Delta_{\mathrm{con}}) \approx 2\pi \times 0.24\,\mathrm{MHz}, \tag{4.17}$$

region (iv). Here, the increased losses from the resonator due to spontaneous scattering of the probe laser field by the atom lead to a transmission minimum. The full width at half maximum of the absorption peak

$$\Delta\delta_{\mathrm{abs}} \approx \frac{\Gamma\Omega_{\mathrm{con}}^2}{4\Delta_{\mathrm{con}}^2} \approx 2\pi \times 63\,\mathrm{kHz} \tag{4.18}$$
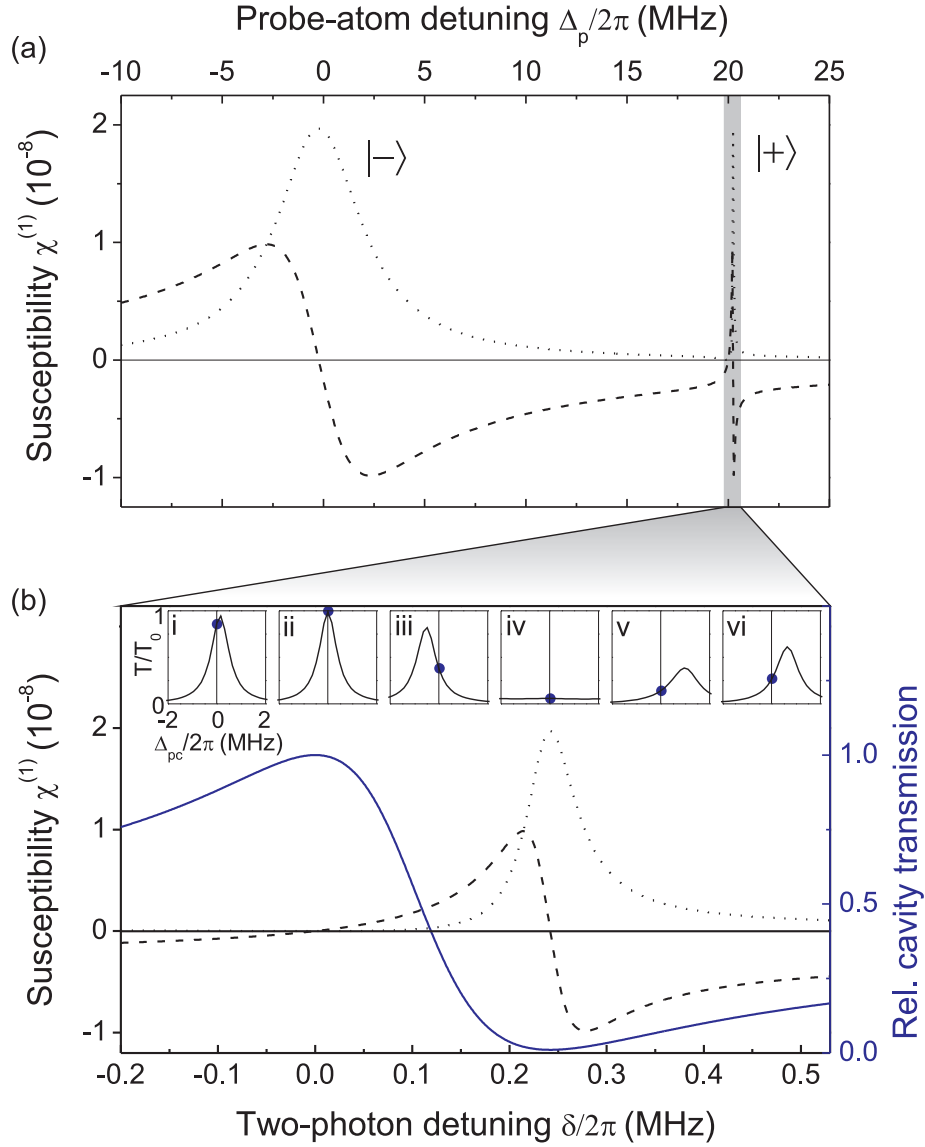
Figure 4.7: (a) Real (dashed line) and imaginary part (dotted line) of the linear susceptibility $\chi^{(1)}$ of a single atom inside the mode volume of the resonator for a control laser detuning of $\Delta_{\text{con}} = 20\,\text{MHz}$. (b) Zoom into the region around the narrow resonance where the experiments are performed. The transmission of a probe beam which is kept on the resonance frequency of the empty cavity (i.e. $\Delta_{\text{pc}} = 0$) is shown as a solid line. The small insets (i) – (vi) show cavity transmission functions as in Fig. 4.3 for a series of fixed values of $\delta/2\pi$ between -100 and $+500\,\text{kHz}$ and the corresponding values of $\chi^{(1)}$.

is much less than the atomic line width Γ, illustrating the large ground state contribution to the dressed state

$$|+\rangle = (1 - \epsilon^2)^{1/2}|g_1\rangle + \epsilon|e\rangle, \qquad (4.19)$$
$$\text{with} \quad \epsilon \approx \Omega_{\text{con}}/(2\Delta_{\text{con}}) \ll 1.$$

In the other regions (i), (iii), (v) and (vi), dispersion dominates over absorption. Here, the change in transmission is caused mainly by the shift of the cavity resonance frequency, tuning the cavity out of resonance with the probe laser. The sign of dispersion changes twice, at $\delta = 0$ and $\delta = \delta_{\text{abs}}$. In the regions (i), (v), and (vi) with negative dispersion ($\text{Re}(n_{\text{ref}}) < 1$), the cavity resonance is shifted to larger frequencies, and vice versa.

Finally, in the limit of large two-photon detunings $|\delta| \gg \delta_{\text{abs}}$, the control laser essentially acts as an incoherent repumping laser, which pumps atoms from state $|g_1\rangle$ to state $|g_2\rangle$, and the transmission approaches the value for a single atom in $|g_2\rangle$, as in Fig. 4.3.

The semiclassical model predicts a contrast of the dispersive transmission signal, defined by the difference between the maximum and the minimum transmission, of almost 100%, in contrast to our measured data. Although the semiclassical model provides still a good qualitative explanation for the shape of the transmission signal, more effects have to be taken into account for a better quantitative agreement.

In particular, the semiclassical model is only valid in the limit of weak probe laser power where all population remains in ground state $|g_2\rangle$. In fact, for our experimental parameters, the non-vanishing probe laser power inside the cavity corresponds to a classical Rabi frequency of $\Omega_{\text{p}} = 2g\sqrt{n_{\text{p}}} = 2\pi \times 1.6\,\text{MHz}$, which is on the same order as the control laser Rabi frequency. The probe intensity causes a finite scattering rate if δ is close to the narrow absorption peak, and a significant amount of population can be incoherently transferred to the ground state $|g_1\rangle$. Therefore, the suppression of the transmission around $\delta = \delta_{\text{abs}}$ is weaker than in the weak-probing limit of the semiclassical model.

Moreover, one has to take into account the contributions of other excited hyperfine states, as described in section 3.5. They contribute to differential light shifts and, in the case of $|F' = 3\rangle$, also to incoherent population transfer between the two ground states.

In addition, a decay of the coherence between the two ground states due to technical noise has to be included in a more realistic model. Ground state dephasing can be caused by spatial and temporal inhomogeneities, e.g., fluctuating atom-cavity coupling, inhomogeneous light shifts and residual magnetic fields. Those effects are subsumed in a phenomenological ground state dephasing rate γ_{deph}, which will be used as an additional fit parameter.

Fit with multilevel quantum model

All effects like finite probe laser power, other excited hyperfine states ($|F' = 3, 5\rangle$) and ground state dephasing have been included in a multilevel quantum model (MQ
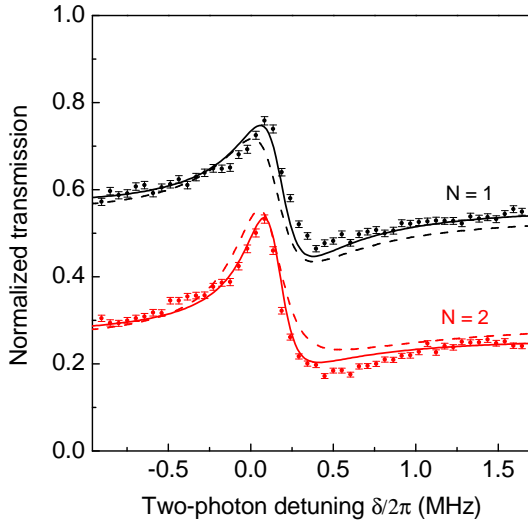
Figure 4.8: Fit of the multilevel quantum model (MQ model) to the measured data for one and two atoms. The solid lines show a fit considering $N_{\mathrm{mod}} = N$ individual atoms in the model (multi-atom sub-model). The dashed lines show a fit considering one atom in the model (eff. one-atom model), with a collective coupling strength of $\sqrt{N} \times g$.

model) for the cavity transmission, see section 3.5. It is an optimized, numerical calculation of the steady state of the Lindblad equation (3.20) for N multilevel atoms. In this model the cavity field is treated quantum mechanically.

Because the Hilbert space and the resulting time-consuming computation grow exponentially with the number of atoms N_{mod} that are incorporated into the model, one is limited by $N_{\mathrm{mod}} \leq 2$. The parameters $g, \Omega_{\mathrm{con}}, \gamma_{\mathrm{deph}}$, and δ_{34} have been varied to obtain the best agreement with the measured data (i.e., minimum χ^2-error χ^2_{min}) for the one- and two-atom data only, see Fig. 4.8. I compare two different variants of the MQ model: The first one incorporates $N_{\mathrm{mod}} = N$ atoms into the model, each atom coupled with g to the cavity mode (multi-atom model). In the second model, only one atom coupled with a collective coupling strength $\sqrt{N} \times g$ is considered (effective one-atom model). The fit results are listed in table 4.1.

First of all, I conclude that both sub-models provide a better quantitative agreement with the measured data than the semiclassical model, even though there are still some significant systematic deviations. The χ^2_{min} is much larger than a value of about 100 which would be expected for purely statistical deviations [1]. The multi-

---

[1] according to the χ^2-distribution with about 100 degrees of freedom, see e.g. [89]

Variant	N_{mod}	g	Ω_{con}	γ_{deph}	δ_{34}	χ^2_{min}
Multi-atom	N	2.85	2.84	0.16	0.11	650
Eff. one-atom	1	$\sqrt{N} \times 2.91$	2.99	0.20	0.07	2619

Table 4.1: Fit results of the multi-atom and the effective one-atom sub-models of the multilevel quantum model (MQ) to the data shown in Fig. 4.8. The values are given in units of 2π MHz.

atom sub-model fits the data still much better than the effective one-atom model. For the measurement with $N = 3$ atoms, a fit using the effective one-atom model with accordingly higher coupling strength even failed to converge. This supports the hypothesis in section 3.5 that several atoms have to be taken into account individually, at least for measurements which do not take place in the weak-probing limit.

The single-atom coupling strength $g/2\pi = 2.85$ MHz inferred from the MQ model fit with individual atoms is slightly higher than the 2.5 MHz deduced from fitting the semiclassical formula to the transmission far from two-photon resonance. This deviation arises from the two-level approximation, where the interactions with the $|F' = 3, 5\rangle$ states are neglected, yielding in a lower transmission for the same coupling strength.

The control laser Rabi frequency Ω_{con} is within the expected range from 1.3 to 6.7 MHz. Since there is no well-defined quantization axis in our system ($B \approx 0$), it is hard to predict the m_F-distribution and the effective dipole moment.

The ground state dephasing γ_{deph} is the only parameter in the multilevel quantum model which can account for the significant reduction of the contrast when compared to the expectation for the case $\gamma_{\mathrm{deph}} = 0$. Moreover, it sets a lower limit for the width of the dispersive signal, i.e. the frequency difference between the maximum and the minimum of the transmission signal, and thus an upper limit for its slope. One contribution to the dephasing might stem from a residual magnetic field: Using microwave spectroscopy of the ground state hyperfine splitting without optical pumping to a specific m_F-state, a width of (74 ± 25) kHz has been measured. If several m_F-sublevels of the ground states are involved, this leads to a broadening of the two-photon resonance. Furthermore, spatially inhomogeneous differential light shifts in connection with the thermal motion of the atoms can lead to dephasing [90]. However, the effect of the trapping laser fields is expected to be on the order of a few kilohertz, since they are linearly polarized and far-detuned from the atomic transition. The main contribution may come from the control laser, which is near-resonant and circularly polarized, leading to differential (vector-) light shifts that are strongly m_F-dependent. Another source of decoherence, the off-resonant photon scattering by the trapping laser fields, is on the order of several s^{-1} for both the lock laser [38] and the dipole trap [39] and can thus be neglected.

The additional differential light shift δ_{34} is the frequency offset between the model and the measured data. It might result from the simplification in the model taking into account only averaged, effective coupling strengths between $|F\rangle$ and $|F'\rangle$-states but neither all different coupling strengths between m_F-states nor their population. The light shift might arise from the coupling of the control or the probe field to 'auxiliary' transitions between $|F, m_F\rangle$ and $|F', m'_F\rangle$-(sub)levels which are not involved in the two-photon process (see next section). For instance, the coupling of $|F = 3, m_F\rangle$ and $|F' = 2, m'_F\rangle$ by the control laser can lead to a differential light shift between ~ 3 and ~ 50 kHz, depending on the specific m_F, m'_F. For the dipole trap, a differential light shift of about 22 kHz has been extrapolated from a microwave spectroscopy experiment (see section 4.14). Moreover, there is

a significant difference in δ_{34} between one and two atoms, which is most obvious when the position of the steep slope in the transmission signal is considered. This might arise from the different probe intensities inside the cavity which depend on the atom number. In principle, the MQ model should already take this effect into account, but the intracavity photon number could be underestimated.

In the next sections, measurements with different control and probe laser power will be presented to discuss the effects of both lasers on δ_{34} and γ_{deph}.

4.4.2 Control laser power variation

In the EIT transmission measurement with different atom numbers N, the control laser illuminating the atom(s) was kept at a constant power of $1\,\mu\mathrm{W}$. Here, we vary the control laser power in a range between $0.25\,\mu\mathrm{W}$ and $2\,\mu\mathrm{W}$ and use always one atom. The measured data is shown in Fig. 4.9. With increasing power, one notices an increase in contrast, a broadening and a shift of the transmission maximum towards higher two-photon detunings. This can be qualitatively understood from the semiclassical model: First of all, the narrow absorption peak becomes wider with increasing power and shifts to higher values of δ, i.e. the linear susceptibility is practically 'stretched' on the δ-axis. If one assumes a fixed dephasing rate, determining basically the experimental resolution on the δ-scale, one expects that with increasing power the dispersive feature can be better resolved and shows a higher contrast simply because it becomes wider. This would mean that one should be able to overcome the contrast reduction caused by dephasing when using a arbitrary high control laser power. However, this seems not to be the case for our experimental data; the contrast does not increase much more for $P_{\mathrm{con}} > 1\,\mu\mathrm{W}$.

Moreover, the shift of the EIT-peak with increasing power suggests that the additional differential light shift δ_{34} is caused to some extent by the control laser.

As mentioned before, a spatially inhomogeneous differential light shift in combination with the motion of the atoms can cause broadening. Therefore, it is obvious to assume in a more sophisticated model that both the shift δ_{34} and the broadening γ_{deph} depend also on the control laser power. To first order, both the light shift and the dephasing can be modelled by a constant offset plus a term which is proportional[2] to the control laser power:

$$\delta_{34}(P_{\mathrm{con}}) = \delta_{34}^{(0)} + \delta_{34}^{(1)} \cdot P_{\mathrm{con}} \tag{4.20}$$

$$\gamma_{\mathrm{deph}}(P_{\mathrm{con}}) = \gamma_{\mathrm{deph}}^{(0)} + \gamma_{\mathrm{deph}}^{(1)} \cdot P_{\mathrm{con}} \tag{4.21}$$

The fit results using this linear dependence in the MQ model are shown in Fig. 4.9. The coupling strength g has been kept constant for all graphs and the control laser Rabi frequency has been scaled according to $\Omega_{\mathrm{con}} \propto \sqrt{P_{\mathrm{con}}}$. The results for the fit parameters are (in units of $2\pi\,\mathrm{MHz}$ and $2\pi\,\mathrm{MHz}/\mu\mathrm{W}$, respectively):

---

[2]A linear dependence between EIT linewidth and control power has also been observed in most experiments with atomic vapors [82].
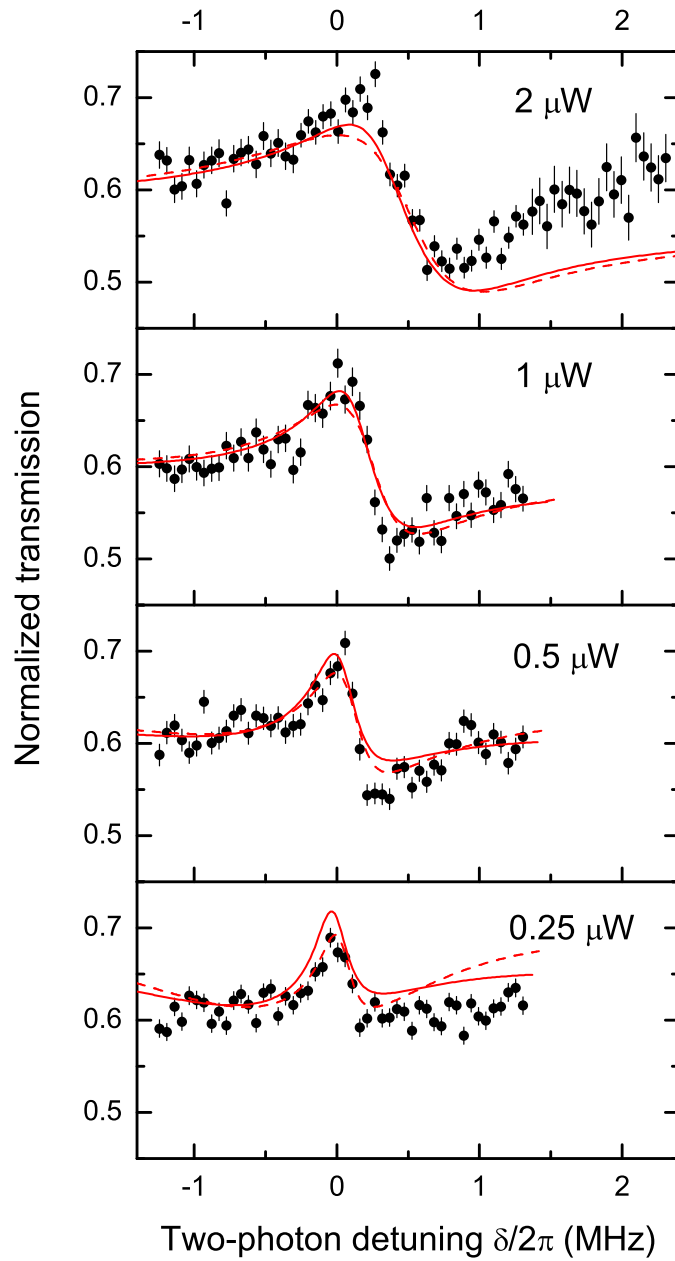
Figure 4.9: EIT transmission signals for $N = 1$, taken at different control laser
powers. The dashed line shows a fit with the multilevel quantum model (MQ
model), and the solid line shows a fit with the multiple Zeeman-sublevel model
(MZS model).

g	Ω_{con}	$\gamma_{\text{deph}}^{(0)}$	$\gamma_{\text{deph}}^{(1)}$	$\delta_{34}^{(0)}$	$\delta_{34}^{(1)}$	$\chi_{\min}^2$
2.73	2.86	0.10	0.33	-0.03	0.20	1738

The values for g and Ω_{con} are compatible with the values obtained from the fit of the data taken with different atom numbers, if one keeps in mind that these data sets have been taken on different days, i.e. the usual day-to-day variation of the coupling strength g. However, there are obvious systematic deviations between the fit curves and the measured data: To account for the saturation of the contrast of the EIT signal at higher control laser power ($2\,\mu$W), a much higher γ_{deph} has to be assumed also for the data taken at intermediate power ($0.5\,\mu$W,$1\,\mu$W) due to the linear model in Eqn. (4.21). The contrast of the calculated curves is lower and their widths are higher than in the corresponding measurements at intermediate power. One could conclude that there is a nonlinear, e.g. quadratic increase of the ground state dephasing rate with power. Another reason might be that the saturation of the contrast is not due to a higher ground state dephasing but due to the Zeeman substructure in Cesium which is not taken into account.

Moreover, there is a systematic deviation in the asymptotic behavior (large δ) especially for $0.25\,\mu$W and $2\,\mu$W. The model predicts incoherent population transfer to $|F = 3\rangle$ when decreasing the lower control laser power due to a lower repumping rate to $|F = 4\rangle$. This would lead to a higher cavity transmission since the $|F = 3\rangle \leftrightarrow |F' = 2, 3, 4\rangle$ transitions are far detuned from the cavity resonance frequency. However, in the measured data the effect seems to be at least much smaller. This could be due to an overestimated intracavity photon number. In section 4.4.3, the effect of the photon number is investigated in more detail. Another reason might be a lower atomic temperature at lower control laser powers: The survival probability of the atoms inside the resonator increases from $(45 \pm 3)\%$ to $(77 \pm 2)\%$ when decreasing the control laser power from $2\,\mu$W to $0.25\,\mu$W. At lower temperatures, the atoms are better localized near the cavity axis, leading to a lower average cavity transmission. This could explain why the measured transmission is systematically lower than inferred from the model at a low control laser power and vice versa.

Finally, the fit gives an additional differential light shift of $\delta_{34}^{(1)}/2\pi = 0.20\,$MHz per μW control laser power. The total shift at $1\,\mu$W is $0.17\,$MHz, which is $0.06\,$MHz larger than obtained in the one- and two-atom fit.

Model with multiple Zeeman states

To improve the model and for better agreement with the measured data, I take a closer look at the transitions that are driven by the near-resonant probe and control lasers, including their polarizations. The control laser is circularly polarized and propagating along the y-axis, whereas the probe laser is linearly polarized along the x-axis and propagating along the z-axis, see Fig. 4.10. When one chooses the quantization axis along the y-direction, the control laser drives pure σ^+ (or σ^-) transitions, while the probe laser simultaneously drives σ^+ and σ^- transitions, see Fig. 4.11. Each Zeeman sublevel $|g_2\rangle = |F = 4, m_F\rangle$ is coupled to both (a coherent

Figure 4.10: Polarization configuration of the probe and the control laser beams.
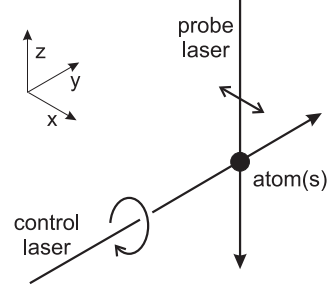
superposition of) the $|e_-\rangle = |F' = 4, m_F - 1\rangle$ and $|e_+\rangle = |F' = 4, m_F + 1\rangle$ excited states by the probe laser via the cavity field. The Hamiltonian describing the interaction between the atoms and the cavity field, see Eqns. (3.15) and (3.35), reads [38, 91]

$$\hat{H}_{\text{int}} = i\hbar \frac{g_-}{\sqrt{2}} (\hat{\sigma}_{e_-g}\hat{a} - \hat{\sigma}_{ge_-}\hat{a}^\dagger) + i\hbar \frac{g_+}{\sqrt{2}} (\hat{\sigma}_{e_+g}\hat{a} - \hat{\sigma}_{ge_+}\hat{a}^\dagger), \qquad (4.22)$$

where $g_\pm$ are the coupling strengths for the $\sigma_\pm$ transitions, which are only equal in the case $m_F = 0$. The excited states $|e_-\rangle$ and $|e_+\rangle$ are coupled to the $|g_{1,-}\rangle = |F = 3, m_F - 2\rangle$ and $|g_{1,+}\rangle = |F = 3, m_F\rangle$ ground states, respectively, forming a double-Λ-system. For some excited m_F levels, however, there is no coupling to ground states, and thus the EIT condition can not be fulfilled for all sublevels.

For each system consisting of these five states (seven, if the states $|F' = 3, m_F \pm 1\rangle$ are included), the cavity transmission is calculated by solving the corresponding Lindblad master equation. The coupling to other excited hyperfine states $|F' = 2\rangle$ and $|F' = 5\rangle$ is taken into account by adding differential light shifts to the $|F = 3\rangle$ ground state energies and changing the effective probe-cavity detuning, respectively, according to Eqns. (3.38) and (3.39). Assuming an equal distribution of the atoms over the $|F = 4, m_F\rangle$ states, the resulting transmission curve is the average of the transmission curves for all substates, see Fig. 4.12. Due to the large variation of the control laser Rabi frequency for different transitions, the position of the transmission minimum is varying or it can even be split into two minima (see $m_F = 3$), whereas the EIT transmission maximum stays almost at the same frequency. The resulting curve has thus a sharper 'peak' and a shallower 'valley' than the curves calculated in the simpler multilevel quantum model, where only averaged, effective coupling strengths between the hyperfine states are considered.

The multiple Zeeman-sublevel model (MZS model) discussed here fits our experimental data somewhat better, especially when the $0.25\,\mu\text{W}$ measurement is considered, see Fig. 4.9. In the multilevel quantum model, g and Ω_{con} are used directly as fit parameters and are later compared with the effective coupling strengths $g_{\text{eff}}^{44'}$ and $\Omega_{\text{con,eff}}^{34'}$, respectively. In the MZS model, the coupling strengths between all levels have been calculated for the ideal case from the corresponding Clebsch-Gordan coefficients and included in the model (assuming that the atom is at an antinode of the probe standing wave and on the control laser axis). The new fit
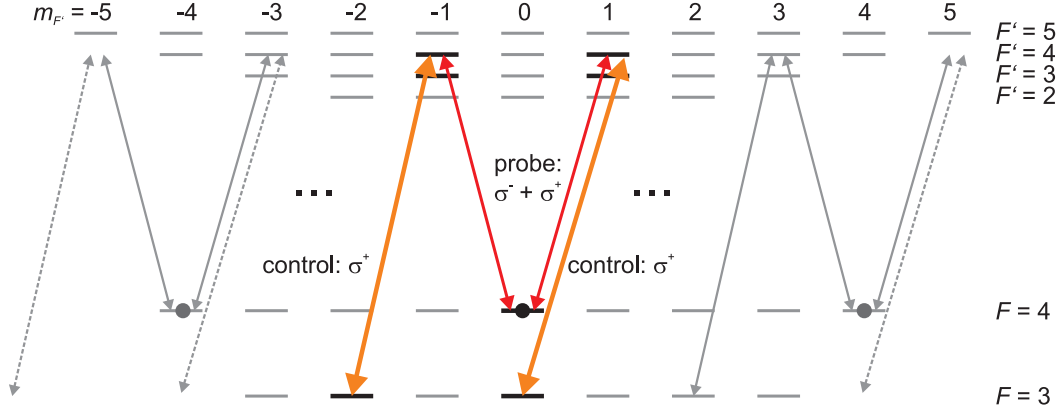
Figure 4.11: Model which incorporates the specific polarizations of the control and the probe beam including averaging over all Zeeman sublevels (MZS model).

Model	g	Ω_{con}	$\gamma_{\mathrm{deph}}^{(0)}$	$\gamma_{\mathrm{deph}}^{(1)}$	$\delta_{34}^{(0)}$	$\delta_{34}^{(1)}$	χ_{min}^2
MZS	2.77	3.35	0.15	0.19	-0.06	0.14	1560
MQ	2.73	2.86	0.10	0.33	-0.03	0.20	1738

Table 4.2: Fit results for the multiple Zeeman-sublevel (MZS) and the multi-level quantum model (MQ). The values are given in units of $2\pi\,\mathrm{MHz}$ and $2\pi\,\mathrm{MHz/\mu W}$, respectively.

parameters g', Ω'_{con} are dimensionless scaling factors for the corresponding coupling strengths in the model. In order to compare them with the MQ model results, one multiplies them with the effective coupling strengths $g_{\mathrm{eff}}^{44'}$ and $\Omega_{\mathrm{con,eff}}^{34'}$. The results are summarized in table 4.2. The value for g is compatible with the fit result of the MQ model. This is reasonable because the value for g is given in first order by the average cavity transmission over a large range of two-photon-detunings δ, i.e. its asymptotic value.

The value for Ω_{con} is higher than the MQ model fit result, since $\Omega_{\mathrm{con,eff}}$ does not include the vanishing couplings to non-existing m_F-sublevels of $|F = 3\rangle$ (dashed arrows in Fig. 4.11) and is thus effectively too large.

The power-dependent ground state dephasing rate $\gamma_{\mathrm{deph}}^{(1)}$ and additional differential light shift $\delta_{34}^{(1)}$ are smaller than in the MQ model. Obviously, some effects that 'look like' stronger dephasing or an additional light shift are to some extent an effect of averaging over different m_F-sublevels: For instance, the averaging smears out the transmission minimum, making it shallower. The MQ model requires a higher ground state dephasing rate to reproduce the same line shape but this leads at the same time to a stronger broadening of the transmission maximum (the EIT peak). The MQ model does not take into account the differential light shift due to
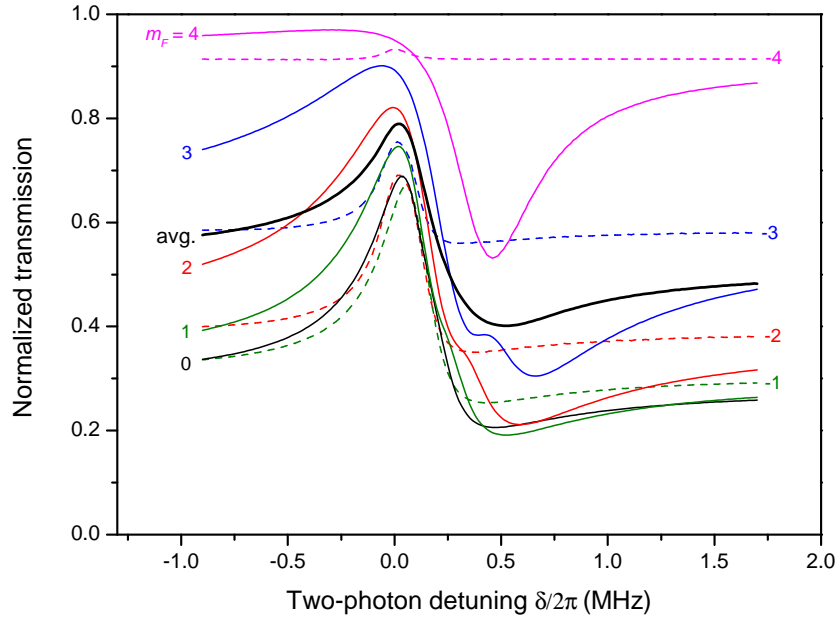
Figure 4.12: Calculated transmission curves for all different $|F = 4, m_F\rangle$ sublevels, and averaged curve.

the coupling of the control laser to the $|F = 3\rangle \leftrightarrow |F' = 2\rangle$ transition. This could at least partly explain the larger value of $\delta_{34}^{(1)}$ compared to the MZS model.

In conclusion, both models provide almost similar fit results. The MQ model, based on only five hyperfine states and on effective coupling strengths, is quite close to the much more sophisticated MZS model taking into account multiple Zeeman sublevels and the polarizations of the laser beams. So far, the MZS model assumes merely a homogeneous distribution over the m_F states and does not incorporate the effects of optical pumping, which are very likely present in our system, see section 2.3.2 and [38]. Ideally, a full simulation with all hyperfine states and Zeeman sublevels, as described in [91], would be required. However, the number of levels which can be explicitly included in such a simulation is limited by the computational power.

Influence of the phase noise of the control laser

In the ideal case, the beat signal between the slave laser and the cooling laser on the photo diode (PD) would be at a single frequency that is given by the two reference oscillators RF1 and RF2. In this case, the two-photon resonance condition between the control laser and the probe laser could be perfectly fulfilled and the scattering of probe and control laser light by the atoms would be suppressed by the EIT effect, i.e. the atom would be prepared in a dark state. However, due to the limited servo bandwidth of the optical phase lock loop and technical noise, the phase difference
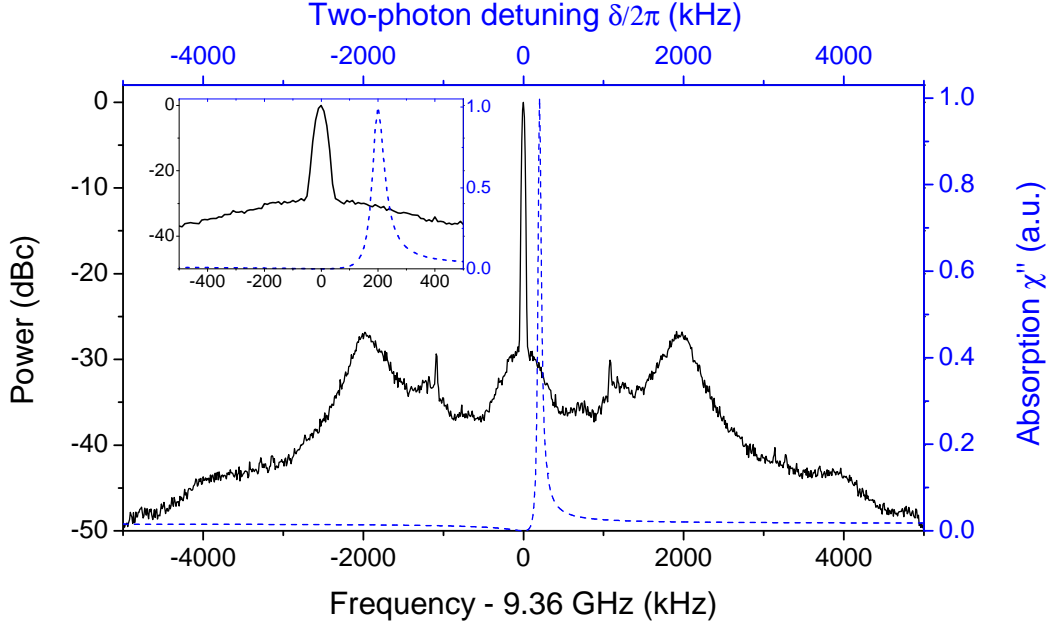
Figure 4.13: Beat signal between the slave laser and the cooling laser recorded
with a resolution bandwidth $\Delta\nu_{\mathrm{RBW}} = 30\,\mathrm{kHz}$ (solid line), in logarithmic units
normalized to the carrier ($0\,\mathrm{dBc}$), and imaginary (absorptive) part of the linear
susceptibility $\chi^{(1)}$. The inset shows a narrow region around the carrier (units
are the same).

of the two lasers with respect to the reference oscillators is fluctuating over time.
This phase noise, which has been characterized in [48], leads to a broadening of
the beat signal in frequency space, see Fig. 4.13. The monochromatic carrier at
$\nu - \nu_{\mathrm{RF1}} - \nu_{\mathrm{RF2}} = 0$ is surrounded by a broad background with characteristic 'servo
bumps' at around $\pm 2\,\mathrm{MHz}$ from the carrier. Consequently, only $\eta_{\mathrm{car}} = 83\,\%$ of the
total control laser intensity irradiated onto the atoms is contained in the carrier and
contributes to the coherent two-photon process. The remaining power in the broad
background contributes to spontaneous photon scattering by the atoms destroying
the (ground-state) coherence. Furthermore, it also contributes to differential light
shifts due to the coupling to other, far-detuned transitions ($|F = 3\rangle \leftrightarrow |F' = 2\rangle$)
in the same way as the carrier does. In the following, I will estimate the orders of
magnitude of the dephasing and additional differential light shifts arising from the
phase noise of the control laser.

For the estimation of the near-resonant scattering by the control laser, let's as-
sume that the carrier dresses the atomic $|F = 3\rangle \leftrightarrow |F' = 4\rangle$ transition with an
effective Rabi frequency of $\Omega_{\mathrm{con}} \approx \sqrt{\eta_{\mathrm{car}}} \times \Omega_{\mathrm{con,eff}}^{34'} \approx 2\pi \times 4\,\mathrm{MHz}$. A narrow ab-
sorption peak (χ'') of width $\Delta\delta_{\mathrm{abs}} \approx \Gamma\Omega_{\mathrm{con}}^2/4\Delta_{\mathrm{con}}^2 \approx 2\pi \times 50\,\mathrm{kHz}$ is created at a
two-photon detuning $\delta_{\mathrm{abs}}/2\pi \approx 0.2\,\mathrm{MHz}$ (Eqns. (4.17) and (4.17)), but with the
same height as the broad, natural resonance in Fig. 4.7(a). A weak laser with Rabi

frequency $\Omega \ll \gamma$ detuned by δ_{abs} from the carrier, i.e. resonant with this narrow peak, would cause a resonant scattering rate of $\Omega^2/2\gamma$. To determine the scattering rate, I determine the overlap integral of the spectral power density $S(\nu)$ of the beat signal with the absorption χ'' (which is normalized to one), yielding

$$R_{\text{sc}} \approx \frac{(\Omega_{\text{con,eff}}^{34'})^2}{2\gamma} \times \frac{\int \chi''(\nu) S(\nu) \mathrm{d}\nu}{\int S(\nu) \mathrm{d}\nu} \tag{4.23}$$

$$\approx (2\pi \times 3.7\,\text{MHz}) \times (3.2 \times 10^{-3}) \approx 75 \times 10^3\,\text{s}^{-1}$$

for a control laser power of $1\,\upmu\text{W}$. While the first factor in Eqn. (4.23) is proportional to the control laser power $P_{\text{con}} \propto \Omega_{\text{con}}^2$, the second factor is almost constant for the power range used in the measurement, so one expects a linear dependence $R_{\text{sc}} \propto P_{\text{con}}$. The value for R_{sc} is about one order of magnitude lower than the ground state dephasing rate $\gamma_{\text{deph}}^{(1)}$ obtained from the fits of the experimental data. Even though this scattering only marginally contributes to decoherence, it cannot be completely neglected.

For the EIT only stability of the *relative* phase of the two lasers is important. Therefore, the same argumentation as above can also be made from the point of view of the probe laser. Since the Rabi frequencies of the two lasers are also on the same order of magnitude, the decoherence effect would be on the same order of magnitude.

Concerning the power-dependent differential light shift due to the coupling of the control laser to the $|F = 3, m_F\rangle \leftrightarrow |F' = 2, m_F'\rangle$ transition, I estimated a value between approx. 3 and $50\,\text{kHz}$ for $P_{\text{con}} = 1\,\upmu\text{W}$, depending on the specific m_F, m_F', see section 4.4.1. The model assumes the interaction with one coherent, monochromatic control light field only, i.e. the $83\,\%$ of the total power which are contained in the carrier. The remaining $17\,\%$ do not contribute to the coherent two-photon process but to the differential light shift in the same way as the carrier does. As this incoherent fraction is not explicitly incorporated into the model, its effect is just contained in the *additional* differential light shift $\delta_{34}^{(1)}/2\pi$. A rough estimation yields

$$\delta_{34}^{(1)}/2\pi \leq 0.17 \times 50\,\text{kHz} \approx 9\,\text{kHz}/\upmu\text{W}, \tag{4.24}$$

one order of magnitude smaller than the fitted value. In summary, the phase noise of the control laser with respect to the probe laser cannot explain the measured dephasing rate and additional differential light shift but should not be neglected.

4.4.3 Probe laser power variation

To investigate the influence of the pre-set intra-cavity photon number $n_{\text{p,0}}$ on the differential light shift δ_{34} and the ground state dephasing rate γ_{deph}, we measure EIT transmission signals for three different probe laser powers. For higher values of $n_{\text{p,0}}$, the average normalized transmission increases and the contrast decreases, see Fig. 4.14. The increase in transmission can have two different reasons: A stronger
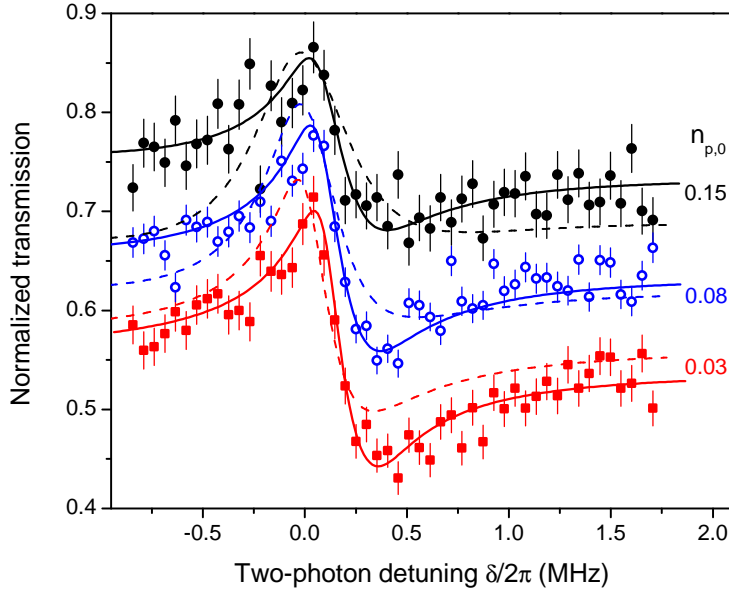
Figure 4.14: EIT transmission spectra for $N = 1$, taken at three different values of the (empty) intracavity photon number $n_{p,0}$. The dashed lines are the result of a MZS model fit where $n_{p,0}$ has been scaled linearly by a factor of 2.7. For the solid lines, $n_{p,0}$ has not been modified but different values of g and δ_{34} have been fitted for each curve.

incoherent population transfer to $|F = 3\rangle$ due to the higher probe intensity or a lower coupling strength g, e.g., due to a worse localization of the atom. To check both hypotheses, I first fit the curve with the smallest probe intensity, $n_{p,0} = 0.028$ with the MZS model (see section 4.4.2) to obtain the parameters $g, \Omega_{con}, \gamma_{deph}$, and δ_{34} for the data with the presumable lowest influence of the probe laser. The results are given in units of 2π MHz

g	Ω_{con}	γ_{deph}	δ_{34}	χ^2_{min}
2.84	3.21	0.14	0.065	49

To check the first hypothesis, I fit all three curves simultaneously with parameters g, δ_{34} and a constant scaling factor for $n_{p,0}$, assuming that our (careful) calibration (Eqn. (1.8)) between photon counts on our detector and $n_{p,0}$ might be incorrect. The fit yields reasonable values for $g/2\pi = 2.84$ MHz and $\delta_{34}/2\pi = -0.025$ MHz, but in a huge scaling factor of 2.7 for $n_{p,0}$. Apart from the strong deviation of the fit from the measured data ($\chi^2_{min} = 699$), this would imply that the intracavity photon number would be almost three times higher than we previously thought — this is quite unrealistic! The second hypothesis is that g depends on $n_{p,0}$. Therefore, I fit each curve with an independent value of g using the MZS model, while using the parameters obtained from the fit of the lowest curve. By this, one obtains a
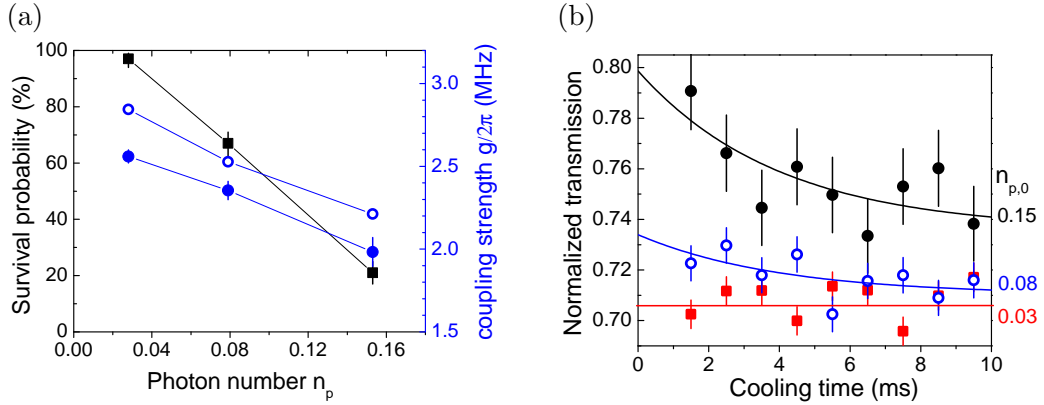
Figure 4.15: (a) Overall probability of atoms to survive the measurement sequence (squares) as a function of the mean empty cavity photon number $n_{p,0}$; coupling strength g as obtained from the fit of data in Fig. 4.14 (open circles) and from the transmission during cooling intervals (full circles). (b) Normalized cavity transmission during the cooling intervals as a function of time after the end of the detuning sweep. Exponential fits are used to extrapolate the transmission and from this the coupling strength in (a) directly after the sweep.

much better agreement ($\chi^2_{\mathrm{min}} = 232$), with coupling strengths $g/2\pi = 2.53\,\mathrm{MHz}$ and $g/2\pi = 2.21\,\mathrm{MHz}$ for intermediate and high probe power, respectively. This result implies that the localization of atoms becomes worse for higher $n_{p,0}$, e.g., due to an increasing temperature. A strong indication for this are significantly increasing atom losses from the trap with increasing probe power, see Fig. 4.15 (a). One can gain even more information when one investigates the transmission during the cooling intervals which are in between the detuning sweeps and where the same settings have been applied ($\delta/2\pi = 0.13\,\mathrm{MHz}$, intermediate $n_{p,0}$). For high and intermediate $n_{p,0}$ during the sweeps, the normalized transmission during the cooling intervals decreases with a time constant of about $4\,\mathrm{ms}$ after the cooling has been started, see Fig. 4.15 (b). Once the cooling has started the coupling strength increases, and thus the transmission decreases. Using this data, one can extrapolate the coupling strength g at the end of the EIT transmission sweeps, i.e. right before the beginning of the cooling intervals: For high and intermediate $n_{p,0}$, I determine the normalized transmission T_0 at $t_c = 0$ from exponential fit functions, and for low $n_{p,0}$, I simply take for T_0 the average transmission during the cooling interval. The coupling strengths g are then inferred from a comparison of T_0 with the MZS model with fixed, intermediate $n_{p,0}$, as set during for the cooling. Even though these coupling strengths are slightly lower than those obtained from the direct fits of the EIT signals with independent g, they change in the same way, see Fig. 4.15 (a). The vertical offset can also be explained since the atoms are heated during the sweeps: The g determined at the end of the sweeps is lower than the average g

inferred from the transmission signals. I conclude that the observed increase of the average transmission between the curves can be well explained by atomic heating and a resulting lowering of the coupling strength g, while a miscalibration of the intracavity photon number seems to be unlikely.

By fitting also the additional differential light shifts δ_{34} individually, I obtain slightly lower values (40 and 35 kHz compared to 65 kHz, resp.). However, the fit does not improve very much ($\chi^2_{\text{min}} = 216$). The fact that the differential light shift does not significantly depend on the intracavity photon number contradicts the hypothesis in section 4.4.1, which rather claims that the shift between the one- and two atom data might be due to the higher intracavity photon number for $N = 1$.

Concerning the ground state dephasing rate γ_{deph}, the data are compatible with a constant value, i.e. the influence of the probe laser is much less than the influence of the control laser.

4.5 Summary and conclusions

The effect of electromagnetically induced transparency of a single atom at two-photon resonance in a coherently driven, effective three-level system has been observed in transmission of the high-finesse cavity. The dispersive shape of the signal can be qualitatively understood with the help of the simple semiclassical model. Here, the linear response of the medium to a weak probe beam in terms of the linear susceptibility leads to a frequency shift or suppression of the cavity resonance due to the dispersive and absorptive properties of the medium. These properties can be strongly modified by a control laser beam.

In the semiclassical model, one should be able to switch between a full probe transmission through the cavity and almost full blockade. However, this is not the case for our system. Ground state dephasing, the coupling to other hyperfine (and m_F-levels) and averaging effects lead to a reduction of the contrast, as described by a multilevel quantum model. The dephasing and the additional differential light shift seem to be mainly caused by the control laser, whereas the probe laser seems to heat the atoms more if its power is increased.

In general, cooling and heating effects seem to play an important role in our system, and the cooling found at around two-photon-resonance has already been utilized during the measurement sequence of the EIT transmission to enhance the lifetime of the atoms. The measurements on cooling and heating will be presented in more detail in the next chapter, for the case inside and outside of the cavity.

5 Cooling atomic motion with EIT

Cooling of atoms to temperatures in the µK-range is an indispensable prerequisite of all our experiments. The colder the atoms are, the better they are confined by the optical trapping potentials and the more stable is their coupling to any other light field. The velocity-dependent, near-resonant interaction of light with atoms is the basis of Laser cooling. For freely moving two-level atoms, the standard cooling method is Doppler-cooling [6, 92] as used in a magneto-optical trap. The temperature limit T_D of Doppler-cooling is closely related to the atomic linewidth $\Gamma = 2\gamma$, yielding

$$T_D \approx \hbar\gamma/k_B \approx 125 \, \text{µK}. \tag{5.1}$$

This temperature is already sufficiently low to capture atoms in our dipole trap of depth $U_0 \approx k_B \times (500 \dots 1000)$ µK. With Sisyphus-type cooling of atoms in the dipole trap by the optical molasses beams, about 30 µK are reached [37]. However, the atomic motion is still significant compared to the waist of the cavity mode, causing, e.g., a fluctuating atom-cavity coupling strength g.

A way to achieve lower temperatures is to use a narrower (effective) atomic transition for cooling. As was discussed in the previous chapter, a resonance which is much narrower than the natural linewidth can be created by Electromagnetically Induced Transparency. This gives rise to a sub-Doppler cooling mechanism which can cool atoms close to quantum mechanical ground state of motion of an harmonic potential [32]. EIT-cooling of trapped ions close to the ground state has been achieved [33, 34].

Concerning our EIT-experiments with neutral atoms in our high-finesse cavity, there are striking similarities with the EIT-cooling scheme. We observe a strong cooling effect in a narrow region around the two-photon resonance, suggesting that such a cooling process plays an important role inside our cavity.

After a brief overview of sideband-cooling mechanisms and an introduction to EIT-cooling in the Lamb-Dicke regime, I will present our observations of EIT-cooling inside the cavity. In this context, cavity-cooling (see section 1.2.2) can also be effective, leading to a complex interplay of both effects. To exclude cavity-cooling effects and to gain more quantitative insight, we perform measurements of EIT-cooling outside the cavity in the optical dipole trap. Applying the method of microwave sideband spectroscopy, we determine the temperature and ground-state occupation of the atoms in the trap.
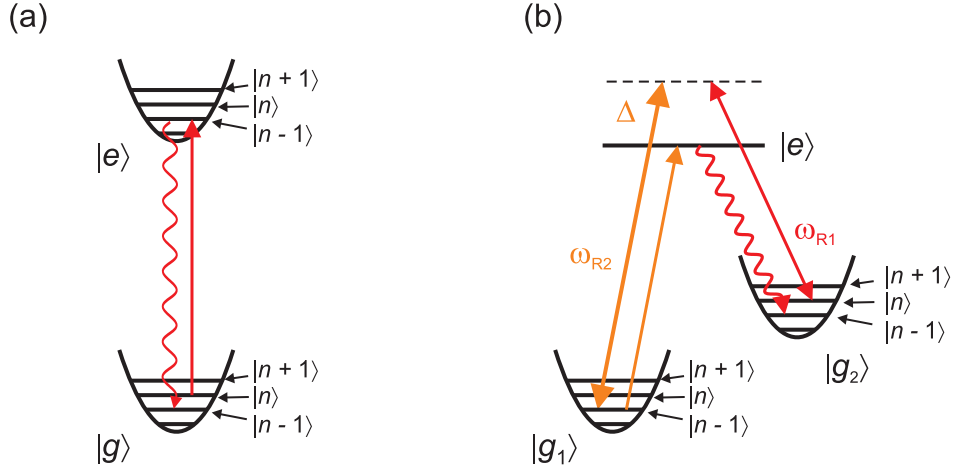
Figure 5.1: (a) Two-level sideband cooling. Energy level scheme of a two-level atom where both the ground state $|g\rangle$ and the excited state $|e\rangle$ are trapped in an harmonic potential. The laser is tuned to the $n \to n-1$ cooling sideband transition. (b) Raman sideband cooling. Energy level scheme of a three-level atom where the two ground states $|g_1\rangle$ and $|g_2\rangle$ are trapped in an harmonic potential. Population from state $|g_2, n\rangle$ is coherently transferred to the state $|g_1, n-1\rangle$ by a two-photon Raman process. A laser resonant with the $|g_1\rangle \to |e\rangle$ transition pumps the atoms back to the state $|g_2\rangle$.

5.1 Cooling in the Lamb-Dicke regime

In a 1D harmonic potential of the form

$$U(x) = \frac{1}{2}m\omega_{\mathrm{ax}}^2 x^2, \tag{5.2}$$

where m denotes the atomic mass and ω_{ax} the trapping frequency, the energy is quantized in equidistant vibrational levels $n \geq 0$ and given by

$$E(n) = \hbar\omega_{\mathrm{ax}}\left(n + \frac{1}{2}\right). \tag{5.3}$$

The fundamental cooling limit in this case is the ($n = 0$) zero-point energy of the binding potential [93]. This limit can be reached by methods of laser cooling when transitions which reduce the vibrational quantum number n can be driven at a much higher probability than transitions that increase the vibrational quantum number, as described in the following.

5.1.1 Two-level sideband cooling

The basic scheme is the method of two-level sideband cooling, which has been demonstrated for single trapped ions [94]. It relies on the selective excitation of

sidebands of the optical resonance, see Fig. 5.1 (a). In contrast to carrier transitions, sideband transitions not only change the internal (electronic) state of the atom but also change its vibrational state $|n\rangle$. A selective excitation requires that the linewidth of the optical transition Γ is much less than the frequency spacing of the vibrational levels, thus $\Gamma \ll \omega_{\mathrm{ax}}$ (*strong confinement* condition [95]). Let us consider the one-dimensional case where a laser propagates along the axis of motion. For cooling, the laser is red detuned by ω_{ax} from the bare atomic resonance frequency and excites an atom from $|g, n\rangle$ to $|e, n-1\rangle$. The subsequent spontaneous decay does not change the vibrational quantum state and ends up in $|g, n-1\rangle$ with highest probability if the *Lamb-Dicke* condition is fulfilled [95]: The extension of the atomic wavepacket x_0 is much smaller than the laser wavelength $\lambda = 2\pi/k$ or, equivalently, the recoil energy E_{rec} is much smaller than the energy spacing between the vibrational levels:

$$x_0 = \sqrt{\frac{\hbar}{2m\omega_{\mathrm{ax}}}} \ll \lambda/2\pi = k^{-1} \tag{5.4}$$

$$\Leftrightarrow E_{\mathrm{rec}} = \frac{\hbar^2 k^2}{2m} \ll \hbar\omega_{\mathrm{ax}} \tag{5.5}$$

$$\Leftrightarrow \eta = kx_0 = \sqrt{\frac{E_{\mathrm{rec}}}{\hbar\omega_{\mathrm{ax}}}} \ll 1, \tag{5.6}$$

where η is called the Lamb-Dicke parameter. On the other hand, the strength of the first-order sideband transitions are proportional to $n\eta^2$ [95], thus η should not be zero.

Two-level sideband cooling also relies on equal trapping potentials for the ground state and the excited state. Therefore, it is easier to implement in ion traps where the external potential does not depend on the internal state of the ion, rather than in experiments with neutral atoms in dipole traps, where this is usually not the case. Moreover, a sufficiently narrow optical transition has to be used. Since optical dipole transitions are usually too broad, one uses much narrower quadrupole transitions to metastable states instead [94, 96]. The long lifetime of such states makes the cooling cycles so slow that the laser coupling to a third level is used to depopulate this level faster.

5.1.2 Raman sideband cooling

To simultaneously obtain equal trapping potentials and a suitable linewidth, one can also couple two (equally trapped) hyperfine ground states $|g_1\rangle$ and $|g_2\rangle$ in a two-photon Raman process via a virtual state which is sufficiently far detuned ($\Delta \gg \Gamma$) from an excited state $|e\rangle$, see Fig. 5.1 (b). In the method of resolved-sideband Raman cooling [93], population from $|g_2, n\rangle$ is coherently transferred to $|g_1, n-1\rangle$ by a stimulated Raman transition. To close the cooling cycle, the population is incoherently pumped to $|g_2, n-1\rangle$ with an additional repumping beam by spontaneous

Raman scattering via, e.g. the excited state $|e\rangle$[1]. This cooling cycle is repeated until the motional ground state is reached.

In contrast to two-level sideband cooling where only one photon with momentum $\hbar\vec{k}$ is absorbed by the atom, Raman sideband cooling relies on the simultaneous absorption of a photon $\hbar\vec{k}_1$ from one laser beam and the emission of a photon $\hbar\vec{k}_2$ into the other beam. Therefore, the momentum transfer is given by $\hbar\Delta\vec{k} = \hbar(\vec{k}_1 - \vec{k}_2)$ and vanishes if the two beams co-progagate, i.e. sideband transitions cannot be driven. More precisely, the component of $\hbar\Delta\vec{k}$ in the direction of motion determines the corresponding Lamb-Dicke parameter [93]

$$\eta_x = \vec{e}_x \cdot (\vec{k}_1 - \vec{k}_2)\, x_0 \,, \tag{5.7}$$

where $\vec{e}_x$ denotes the unit vector along the x-axis. Although the Lamb-Dicke parameter η_x related to the *coherent* two-photon process can be made arbitrarily small, the efficiency of ground state cooling is still limited by the recoil energy of the *incoherently* scattered photon, and thus condition (5.6) has to be fulfilled.

5.1.3 Microwave sideband cooling

Instead of using two lasers to drive Raman transitions between two ground states, one can also couple them directly via a magnetic dipole transition using microwave radiation. Since the momentum of microwave photons is negligible compared to optical photons, the Lamb-Dicke parameter would be too small to drive sideband transitions. To obtain a significant coupling between different vibrational states, the trapping potentials for the two ground states are shifted spatially by an amount $\Delta x \lesssim x_0$ with respect to each other. In this case, an effective Lamb-Dicke parameter

$$\eta_{\text{eff}} \equiv i\Delta x/(2x_0) \tag{5.8}$$

can be defined [98].

Later in this chapter, the method of microwave sideband spectroscopy will be explained in more detail and its application in our setup to measure the temperatures obtained with EIT cooling will be presented.

5.1.4 EIT-cooling

The selective excitation of a sideband transition, which is the basis of the cooling schemes discussed above, can also be realized using EIT [32]. It allows to tailor the absorption profile such that the cooling transition can be selectively excited while carrier and heating sideband ($n \rightarrow n+1$) transitions are suppressed. Unlike in the Raman cooling scheme, both lasers are near-resonant with the dipole-allowed transitions $|g_1\rangle \leftrightarrow |e\rangle$ and $|g_2\rangle \leftrightarrow |e\rangle$, respectively, see Fig. 5.2 (a).

---

[1] If the lifetime $1/\Gamma$ of the state $|e\rangle$ is much shorter than the oscillation period $1/\omega_{\text{ax}}$ of the atoms, $|e\rangle$ can be adiabatically eliminated and doesn't have to be a trapped state [97].
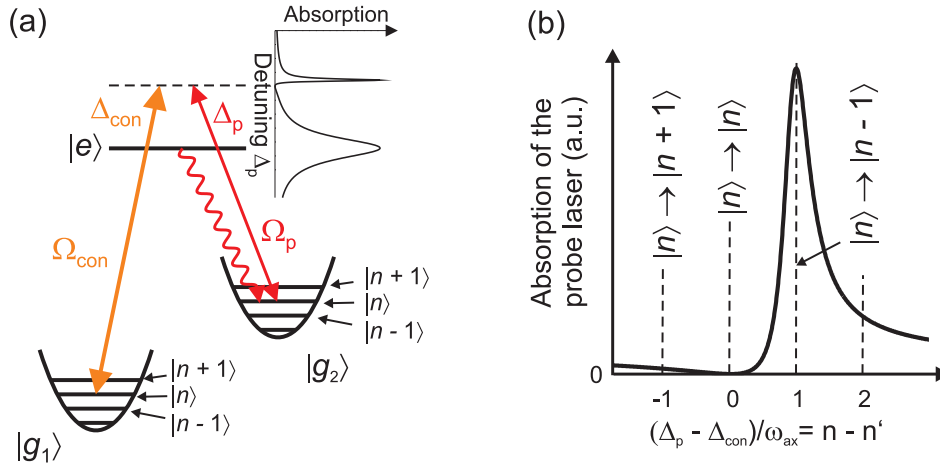
Figure 5.2: EIT-cooling: (a) Energy level scheme for an atom where the two ground states $|g_1\rangle$ and $|g_2\rangle$ are trapped in an harmonic potential with trap frequency ω_{ax}. For levels with the same vibrational quantum number n, the two-photon resonance condition is fulfilled. (b) Absorption of the cooling laser as a function of the two-photon-detuning, which depends on the change of n. For the carrier transition $(n \to n)$, the absorption vanishes due to the EIT effect while the cooling sideband transition $(n \to n-1)$ can be selectively excited (adapted from [32]).

Let's assume for the sake of simplicity that the cooling laser Ω_{p} is much weaker than the control laser Ω_{con}. For blue detuning of the control laser $\Delta_{\mathrm{con}} > 0$, the absorption spectrum of the probe laser [inset of (a); (b)] exhibits a broad resonance at $\Delta_{\mathrm{p}} = -\delta_{\mathrm{s}}$, a dark resonance at $\Delta_{\mathrm{p}} = \Delta_{\mathrm{con}}$ and a narrow resonance at $\Delta_{\mathrm{p}} = \Delta_{\mathrm{con}} + \delta_{\mathrm{s}}$, where

$$\delta_{\mathrm{s}} = \frac{1}{2}\sqrt{\Delta_{\mathrm{con}}^2 + \Omega_{\mathrm{con}}^2} - \frac{\Delta_{\mathrm{con}}}{2} \approx \frac{\Omega_{\mathrm{con}}^2}{4\Delta_{\mathrm{con}}} \tag{5.9}$$

is the AC-Stark shift induced by the control laser [32].

If the two-photon resonance condition for ground states with the *same* vibrational quantum number, e.g. $|g_1, n\rangle$ and $|g_2, n\rangle$, is fulfilled, excitation of the carrier transition $|n\rangle \to |n\rangle$ is completely suppressed due to the EIT effect, see Fig. 5.2 (b). Therefore, in contrast to sideband cooling schemes, there is no heating that accompanies (off-resonant) absorption on the carrier transition [32]. At the same time, the lasers are not in two-photon resonance for states with a *different* vibrational quantum number (the sideband transitions). In particular, the cooling laser is in resonance with the narrow resonance with respect to the cooling sideband transition $|n\rangle \to |n-1\rangle$ if the condition

$$\delta_{\mathrm{s}} = \omega_{\mathrm{ax}} \tag{5.10}$$

is fulfilled. This can be achieved, e.g., by tuning the control laser Rabi frequency,
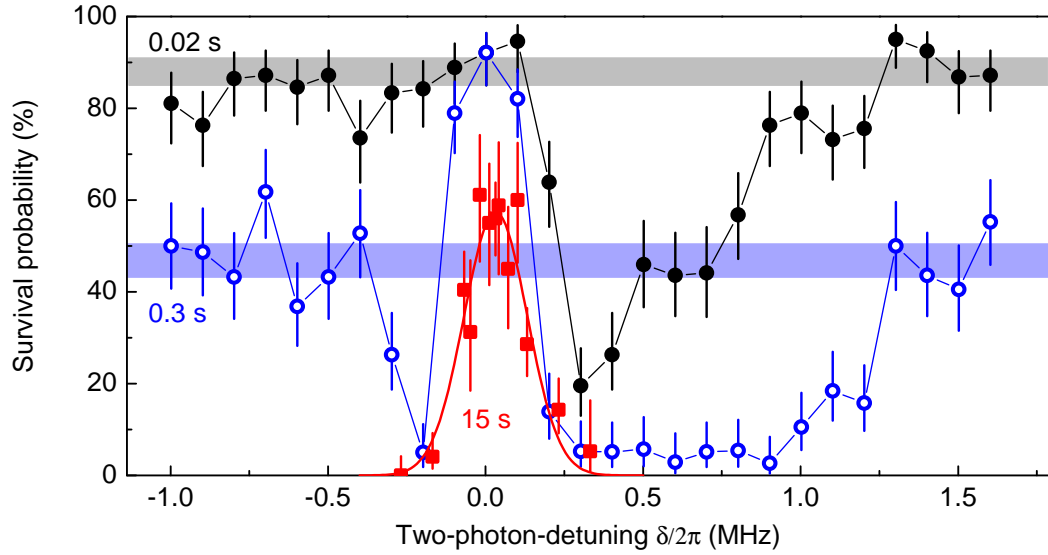
Figure 5.3: Survival probability of one atom inside the resonator for three differ-
ent holding times. The shaded areas indicate the survival probabilities for
large two-photon detunings for the two smaller holding times. For the longest
holding time of 15 s, a Gaussian fit curve is shown along with the data points.

see Eqn. (5.9). However, due to the special shape of the Fano-like resonance [85],
condition (5.10) is not so critical for cooling: Excitation of the cooling sideband can
be achieved for several modes that are within a range of vibrational frequencies,
whereas the excitation of the heating sideband transition $|n\rangle \rightarrow |n + 1\rangle$ is always
much lower.

Moreover, the whole argumentation as above is still valid if the role of the two
lasers is interchanged or if they are of equal strength (coherent population trapping,
CPT). Both lasers continuously cool the atoms and there is no need for or a pulsed
sequence or an additional repumping laser, as in a Raman-cooling scheme.

EIT-cooling experiments with trapped ions in the group of R. Blatt have reached
a 3D-ground state occupation of about 90 % [34]. Moreover, they have also demon-
strated that the method is a relatively robust and simple tool for the simultaneous
cooling of several vibrational modes.

5.2 EIT-cooling inside the cavity

During our first measurements of the EIT transmission signals (see last chapter) we
have observed that the shape of the signal depends on the direction of the detuning
sweep. Moreover, atoms got preferentially lost at certain values of the two-photon
detuning δ. This was an indication that there are strong heating (and cooling)
processes which change the atom-cavity coupling strength g, leading to a change in
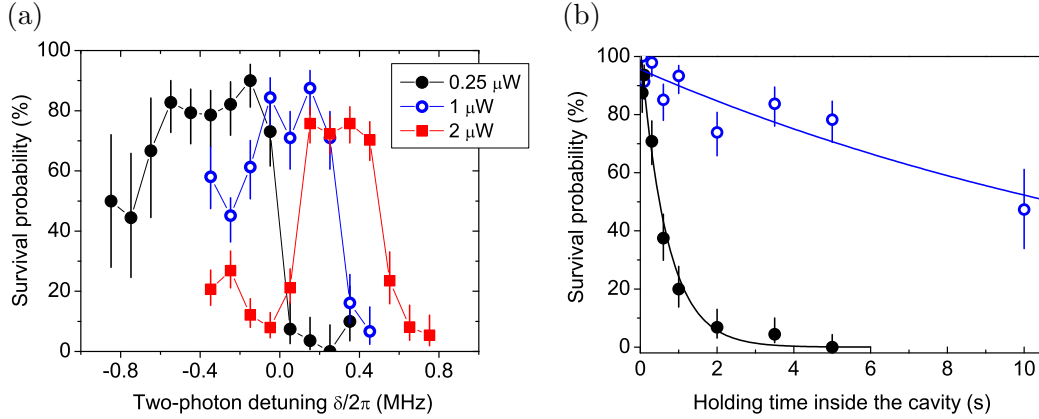
(a)

(b)

Figure 5.4: (a) Survival probability of one atom inside the resonator for a holding time of 0.3 s for different values of the control laser power showing the power-dependent shift oft the cooling region. (b) Survival probability of one atom inside the resonator as a function of time; *open circles*: with cooling at two-photon resonance; *full circles*: with only the far-off-resonant trapping lasers switched on. From exponential fits to the data (solid lines), I infer lifetimes of the atoms in the trap.

average cavity transmission.

We investigate this effect in more detail by measuring the survival probability of single atoms inside the cavity for different, fixed values of δ and for three different holding times Δt_{h} inside the resonator, see Fig. 5.3. The following sequence is applied: First, exactly one atom is placed into the center of the cavity. Then, the same settings as for the measurement of the EIT transmission traces with different atom numbers (section 4.4.1) are applied, but with a constant δ. After a time $\Delta t_{\mathrm{h}} = (0.02, 0.3, 15)$ s, the atom is retrieved from the cavity and transported back to the position of the MOT where its presence is checked by fluorescence detection. After the shortest holding time of 0.02 s, strong losses occur for $\delta/2\pi \approx (0.1 \ldots 1.2)$ MHz. Outside this heating region, the measured survival probabilities are compatible with the reference value measured far from two-photon resonance ($\delta/2\pi \approx \pm 3$ MHz), indicated by the gray-shaded area. The reference value is already significantly reduced to about 50 % for $\Delta t_{\mathrm{h}} = 0.3$ s. Here, the heating region is already saturated, but at around two-photon resonance, the survival probability is still close to 100 %. At $\delta/2\pi \approx -0.2$ MHz, another relatively narrow heating region appears. For a much longer holding time of 15 s, the majority of the atoms still survive around two-photon resonance. A Gaussian fit of this measurement reveals a center frequency of $\delta_{\mathrm{c}}/2\pi = (0.032 \pm 0.009)$ MHz and a full-width-at-half-maximum of (0.24 ± 0.02) MHz. Note that this value is comparable to the width of the dispersive EIT transmission signal (section 4.4.1) and significantly smaller than both the cavity and the atomic linewidths 2κ and Γ, respectively. This is a

first indication that the effect relies on the creation of a coherent dark state, i.e. on the EIT effect.

Moreover, we vary the control laser power and measure the survival probability for a holding time of $0.3\,\mathrm{s}$, see Fig. 5.4 (a). The steep transition from high to low survival probability shifts to higher values of δ by an amount that is comparable with the shift of the EIT transmission signal when the control laser power is increased, see section 4.4.2. This shows again the close connection between the heating and cooling effects and the EIT transmission signal.

The next question arises: Is this relatively long lifetime at two-photon-resonance a real *cooling* effect or just the *absence of heating* due to the suppression of near-resonant scattering due to the EIT effect? To answer this question, we compare the lifetime at two-photon resonance with the lifetime of the atoms when only the far-off-resonant trapping lasers (i.e. the dipole trap and the lock laser) are switched on. In the latter case, recoil heating due to near-resonant photon scattering can be neglected. The lifetime in this case is only $(0.7 \pm 0.1)\,\mathrm{s}$ compared to $(16 \pm 3)\,\mathrm{s}$ for the two-photon-resonance-case, see Fig. 5.4 (b). Therefore, the long lifetime at around two-photon resonance is indeed due to a strong cooling effect!

We utilized this cooling effect in our measurement sequence for the EIT transmission signals, see section 4.3. When the cooling is applied in between the detuning sweeps, the number of measurement cycles can be increased by about a factor five to obtain the same survival probability. This helps to speed up our measurements and to gain more information within the same amount of time.

A Sisyphus-type cavity-cooling mechanism is probably also effective in our system [7, 37, 38]. In particular, if the cavity frequency is blue-detuned from the $|F = 4\rangle \leftrightarrow |F' = 5\rangle$ transition, long trapping times of several seconds are observed, see section 1.2.2. This mechanism is based on the position-dependence of the dressed-states energies of the coupled system of a *two*-level to the cavity field [56]. In the *three*-level EIT-configuration presented here, this type of cavity-cooling could play a role for large two-photon-detunings, where the system becomes an effective two-level system, see section 4.4.1. To check whether this effect is significant, I compare the lifetime of the atoms for large values of δ with the lifetime limited by near-resonant photon scattering. The latter can be estimated from the scattering rate of probe laser light by the atom inside the cavity [38]

$$R_{\mathrm{sc}} \approx n_{\mathrm{p}} \times \frac{g^2 \Gamma}{\Delta_{\mathrm{p}}^2} \approx 3 \times 10^4\,\mathrm{s}^{-1}, \tag{5.11}$$

where $n_{\mathrm{p}} = 0.04$ is the mean intracavity photon number inferred from the photon count rate for large δ and $g/2\pi = 2.8\,\mathrm{MHz}$ is the atom-cavity coupling obtained from the fit, see section 4.4.1. To estimate the lifetime τ_{sc} inside our trap, I compare the trap depth $U_{0,\mathrm{cav}}$ with the heating rate: For every scattered probe photon, the atom is heated by twice the recoil energy $E_{\mathrm{rec}} = \hbar^2 \omega_{\mathrm{p}}^2/(2mc^2) = k_{\mathrm{B}} \times 100\,\mathrm{nK}$, where m is the atomic mass [99, 100]. One obtains

$$\tau_{\mathrm{sc}} \approx \frac{U_{0,\mathrm{cav}}}{2 E_{\mathrm{rec}} R_{\mathrm{sc}}} \approx 0.1\,\mathrm{s}, \tag{5.12}$$
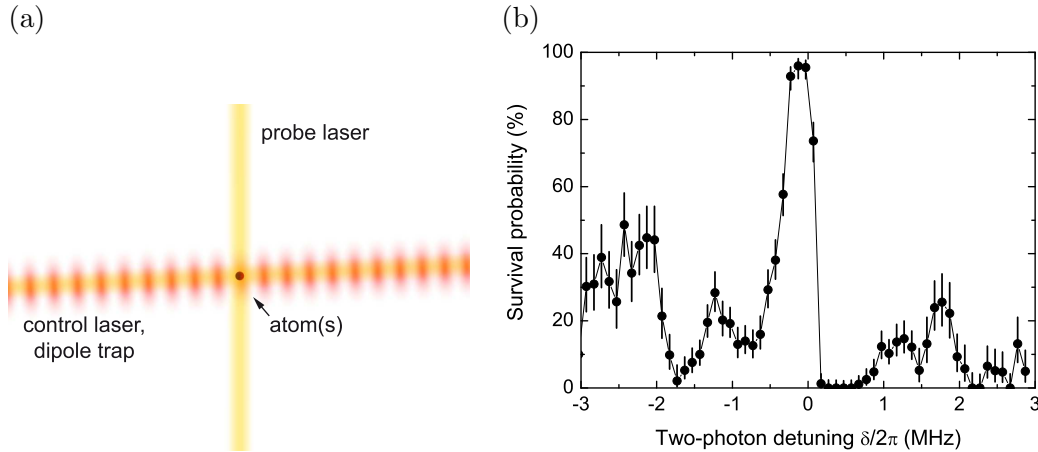
(a)

(b)

Figure 5.5: (a) Schematic setup for the EIT-cooling in the dipole trap. The atoms are illuminated by both the control laser, running along the trap axis and the probe laser incident from the z-direction. (b) Survival probability of a small number of atoms in the standing-wave dipole trap as a function of the two-photon detuning.

where $U_{0,\text{cav}} \approx k_{\text{B}} \times 0.5\,\text{mK}$ [Eqn. (4.13)]. The measured lifetime for large values of δ is about $0.4\,\text{s}$, which is inferred from the measurement presented in Fig. 5.3. So there is probably also a cavity-cooling effect, but not as strong as for the $|F = 4\rangle \leftrightarrow |F' = 5\rangle$ transition.

In conclusion, the observation of a narrow cooling region around two-photon resonance and the close relationship with the position and width of the EIT transmission signal is a strong indication that EIT-cooling is effective inside the cavity. However, cavity-cooling effects cannot be neglected, at least not for large values of $|\delta|$.

5.3 EIT-cooling measurements in the dipole trap

To gain more insight into the EIT-cooling effect and to exclude possible cooling effects relying only on the atom-cavity coupling, we perform measurements with the atoms trapped in the standing-wave dipole trap but outside the cavity, at the position of the MOT. The control laser beam is still running along the trap axis but the probe laser is directly shone on the atom(s) instead of being coupled into the cavity, see Fig. 5.5 (a). The atoms are strongly confined along the trap axis (y-axis) with a trap frequency of about $\nu_{\text{ax}} \approx (0.2 \ldots 0.3)\,\text{MHz}$. This corresponds to a Lamb-Dicke parameter of $\eta \approx 0.1$. In contrast, there is only a weak confinement in the radial directions with trap frequencies of $\nu_{\text{rad}} \approx (1 \ldots 2)\,\text{kHz}$.

For a typical control laser power of $P_{\text{con}} = 1\,\mu\text{W}$, I estimate an effective con-
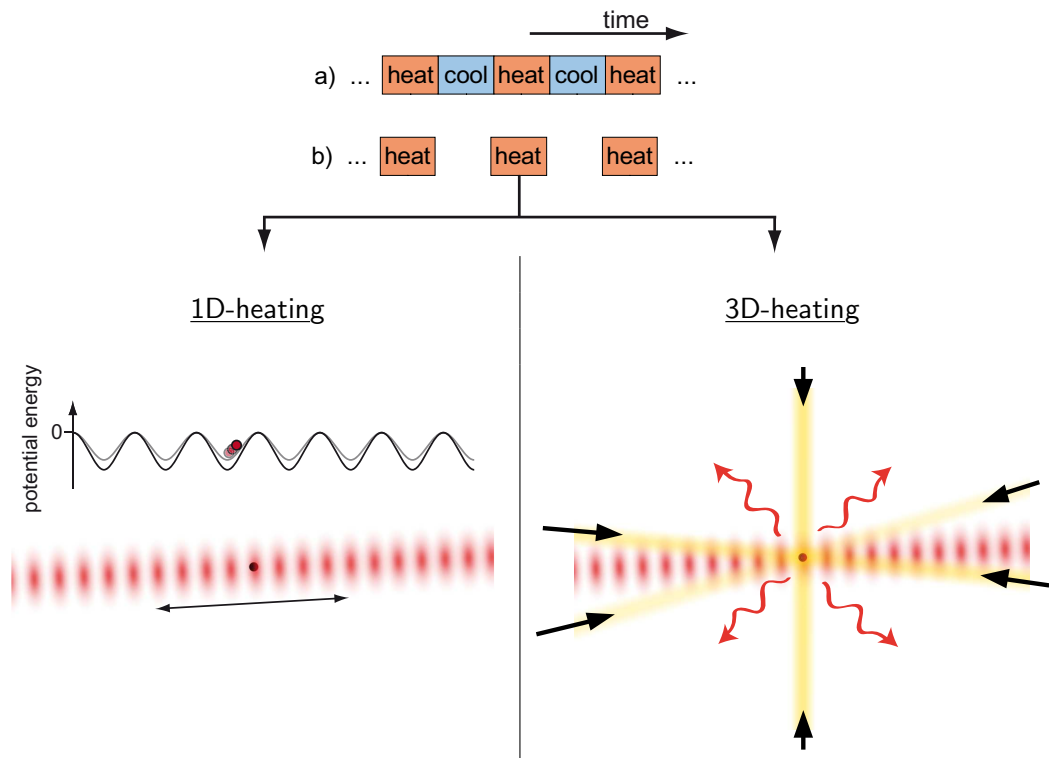
Figure 5.6: *Upper part:* Sequences to check for cooling in different spatial dimensions: (a) Heating pulses are alternated with EIT-cooling pulses. (b) Only heating pulses are made. *Lower part:* 1D-heating: The optical lattice is shifted back and forth along the trap axis. During the shift the potential depth is modulated due to an interference effect. 3D-heating: The near-resonant optical molasses beams are shone onto the atoms, causing isotropic recoil heating due to photon scattering.

| Heating | EIT-cooling | |
	applied	not applied
1D	65 ± 3	26 ± 3
3D	$15.8^{+1.5}_{-1.4}$	$17.2^{+1.4}_{-1.3}$

Table 5.1: Survival probabilities (in %) after applying three 1D- and 3D-heating pulses with and without EIT-cooling pulses in between.

trol laser Rabi frequency of $\Omega^{34'}_{\mathrm{con,eff}}/2\pi = 3.1\,\mathrm{MHz}$ at the position of the MOT ($w_{\mathrm{con,MOT}} = 103\,\mathrm{\mu m}$ [48]). There, the probe laser beam has a waist of about $0.6\,\mathrm{mm}$ and a typical power of about $1\,\mathrm{\mu W}$, corresponding to an effective Rabi frequency of $\Omega^{44'}_{\mathrm{p,eff}}/2\pi = 0.5\,\mathrm{MHz}$.

Similarly to the measurements inside the cavity, the survival probability of a small number (approx. 10 per repetition) of atoms loaded into the dipole trap is measured for a fixed holding time of $300\,\mathrm{ms}$ as a function of the two-photon detuning δ between the two lasers. Almost all atoms stay trapped in the range $\delta/2\pi \approx -0.2\ldots0.0\,\mathrm{MHz}$ and strong losses occur between 0.2 and $0.8\,\mathrm{MHz}$. The next question that arises is whether this maximum of the survival probability is due to cooling and not only due to the absence of heating because of the suppression of photon scattering by the atoms due to the EIT effect. If it is cooling, it is also interesting to know along which spatial dimensions it is effective. To answer these questions, we use heating pulses with different dimensionality (1D and 3D) and alternate them with EIT-cooling pulses ($\delta/2\pi = -0.07\,\mathrm{MHz}$, duration $10\,\mathrm{ms}$), see Fig. 5.6 (a). If the cooling can counteract the heating, the survival probability of the atoms should be higher than in the case where only the heating pulses are made, Fig. 5.6 (b).

We induce one-dimensional heating along the dipole trap axis by detuning the frequencies of the two counter-propagating laser beams with respect to each other by $\Delta\nu_{\mathrm{DT}}$. This has two effects: On one hand, the lattice moves with a velocity $\Delta\nu_{\mathrm{DT}}\lambda_{\mathrm{DT}}/2$, and on the other hand, the effective trap depth and phase are modulated due to a parasitic optical interference effect [35]. The latter can cause either resonant or parametric heating of the atoms, if the relative detuning $\Delta\nu_{\mathrm{DT}}$ of the the two beams is equal to ν_{ax} or $2\nu_{\mathrm{ax}}$, respectively. A 1D-heating pulse consists of shifting the lattice and with it the atoms by $0.62\,\mathrm{mm}$ in one direction and back to the initial position. A shift is done by increasing $\Delta\nu_{\mathrm{DT}}$ linearly from 0 to $0.6\,\mathrm{MHz}$ within $2\,\mathrm{ms}$ and then decreasing it to 0 in another $2\,\mathrm{ms}$, sweeping over both the direct and the parametric resonance.

Three-dimensional heating is induced by near-resonant optical molasses beams (see section 1.1.1), consisting of three mutually orthogonal pairs of counter-propagating laser beams, which are shone onto the atoms, causing isotropic heating due to near-resonant photon scattering. The duration of the pulses is about $10\,\mathrm{ms}$ each.

The measured survival probabilities after applying three 1D- and 3D-heating

pulses with and without EIT-cooling pulses in between are listed in table 5.1. The values in the 1D-case show a strong increase of the survival probability when EIT-cooling is applied, but no significant change is effected in the 3D-case. So the EIT-cooling is effective at least along the dipole trap axis, but not in all spatial dimensions. This is not surprising since there is no component of the difference wave vector $\Delta \vec{k}$ of the EIT-cooling beams in the x-direction, which is perpendicular to both the control laser beam and the probe laser beam, and thus the corresponding Lamb-Dicke parameter η_x vanishes, cf. Eqn. (5.7). Therefore, there can be at least no cooling in the x-direction. Cooling also along this direction could be achieved, e.g., by changing the direction of the control laser beam in the x-y-plane.

5.3.1 Microwave sideband spectroscopy

The two hyperfine ground states $|F = 3, 4\rangle$ in cesium can be directly coupled using microwave radiation with a frequency of about $9.2\,\mathrm{GHz}$. When one takes into account also the external degree of freedom, i.e. the vibrational quantum state n in the (one-dimensional) optical lattice, we drive a sideband transition if n changes during the transition between the two internal states. From sideband spectroscopy, one can gain information about the occupation of different n-states and thus the (one-dimensional) temperature of the atoms. In particular, if an atom is in the lowest vibrational state $n = 0$, it is impossible to drive a $n \rightarrow n - 1$ sideband transition. Therefore, the strength of this sideband is a sensitive measure for the occupation of the motional ground state. We use microwave sideband spectroscopy as a tool to characterize the efficiency and the dynamics of EIT-cooling in the dipole trap as a function of experimental parameters.

State-dependent optical lattice

The strength of a transition between different internal and external states is determined by matrix elements describing the interaction between light and atoms, taking into account also the external degree of freedom of the atomic center-of-mass motion [92, 101]:

$$\hbar\Omega_{n,n'} = \langle F', m'_F, n'_{F',m'_F} | \hat{H}_{\mathrm{af}} \exp(i\Delta k \hat{y}) | F, m_F, n_{F,m_F} \rangle \qquad (5.13)$$

$$= \underbrace{\langle F', m'_F | \hat{H}_{\mathrm{af}} | F, m_F \rangle}_{\hbar\Omega_{\mathrm{bare}}} \times \underbrace{\langle n'_{F',m'_F} | \exp(i\Delta k \hat{y}) | n_{F,m_F} \rangle}_{f_{nn'}}, \qquad (5.14)$$

where the atom-field Hamiltonian $\hat{H}_{\mathrm{af}}$ acts exclusively on the internal degree of freedom and the momentum shift operator $T_{\Delta p} \equiv \exp(i\Delta k \hat{y})$ on the external degree of freedom [97]. The (resonant) Rabi frequency $\Omega_{n,n'}$ of a sideband transition is the product of the Rabi frequency of the 'bare' internal transition Ω_{bare} and the wave function overlap $f_{nn'} = \langle n'_{F',m'_F} | T_{\Delta p} | n_{F,m_F} \rangle$, which is is called, in analogy to molecular physics, Franck-Condon factor [102].
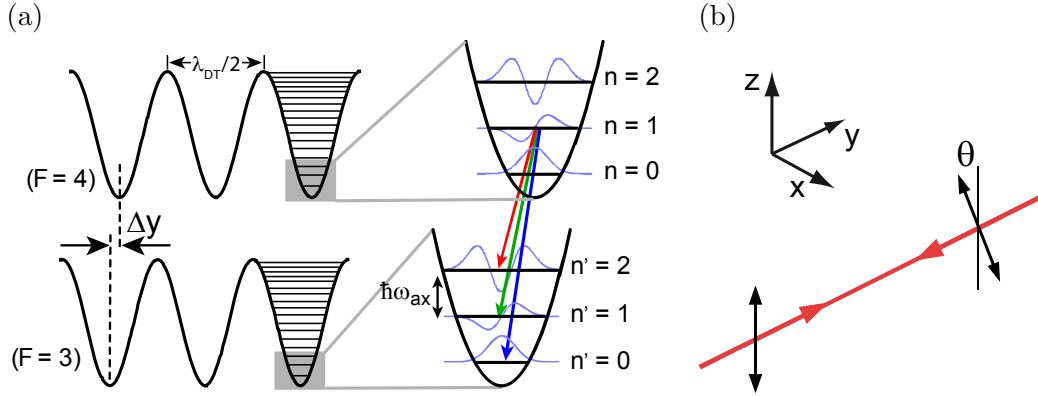
(a)

(b)

Figure 5.7: (a) The effective standing-wave potentials for the states $|F = 3\rangle$ and $|F = 4\rangle$ are displaced by an amount Δy with respect to each other. The right part shows the three lowest energy levels of each potential and the corresponding wave functions. Starting from $|F = 4\rangle$, the blue sideband transition corresponds to $n \rightarrow n-1$ and the red sideband to $n \rightarrow n+1$. Adapted from [98]. (b) The state-dependent lattice is formed by the two counter-propagating laser beams of the dipole trap where the directions of the linear polarizations are rotated by an angle $\theta \neq 0$ with respect to each other.

Due to the negligible recoil momentum Δk of a microwave photon, the Franck-Condon factor reduces to $\langle n'_{F',m'_F} | n_{F,m_F} \rangle$. If the trapping potentials for both hyperfine ground states are equal, which is usually the case in our setup, all wave function overlaps between different vibrational states vanish, i.e. $\langle n'_{F',m'_F} | n_{F,m_F} \rangle = \delta_{nn'}$, and thus sideband transitions cannot occur.

However, a significant coupling between different motional states can be achieved by shifting the trapping potentials for $|F = 3\rangle$ and $|F = 4\rangle$ by an amount Δy with respect to each other, see Fig. 5.7 (a). This means replacing the momentum shift operator $T_{\Delta p}$ in Eqn. (5.13) by a shift operator $T_{\Delta y} \equiv \exp(-i\Delta y \hat{p}/\hbar)$ in position space [97]. The wave function overlap for different n, n', and with it the relative strength of the sideband transitions, can then be controlled by the relative shift Δy.

Such a state-dependent optical lattice can be generated in a so-called lin-θ-lin configuration of two counter-propagating linearly polarized laser beams, where the electric-field vectors of the two waves enclose an angle θ, see Fig. 5.7 (b). The resulting standing wave can be decomposed into two circularly polarized standing waves which are mutually displaced by $\lambda_{\mathrm{DT}}\theta/2\pi$. Due to the strong $|F, m_F\rangle$ state-dependency of the AC-Stark-shifts for circularly polarized light, the effective trapping potentials for $|F = 3, m_F\rangle$ and $|F = 4, m'_F\rangle$ are shifted by an amount Δy with respect to each other along the trap axis. The effective potential for atoms in
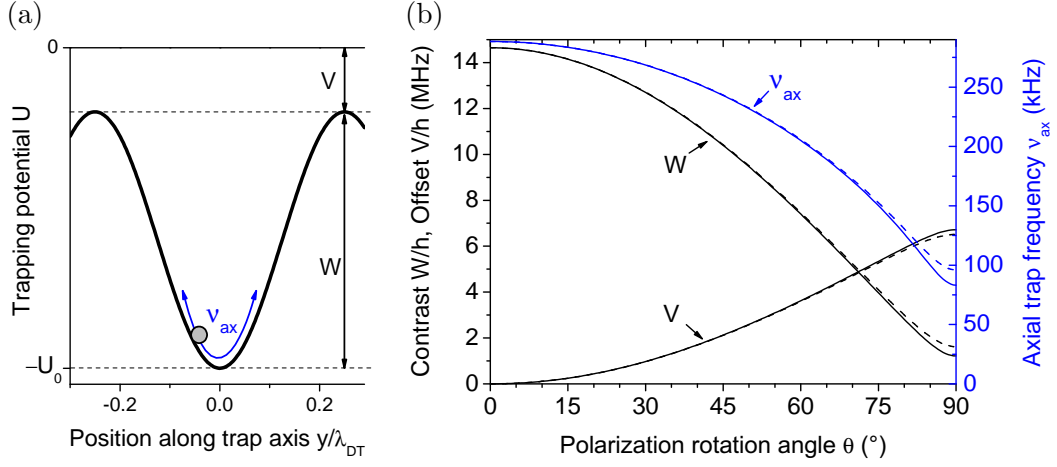
Figure 5.8: (a) Illustration of the trapping potential for atoms in a state $|j\rangle$ as a function of position along the y-axis. (b) Calculated contrast $W_{|j\rangle}(\theta)$, offset $V_{|j\rangle}(\theta)$ and axial trap frequencies $\nu_{\mathrm{ax},|j\rangle}(\theta)$ of the effective potentials for the states $|F = 3, m_F = -3\rangle$ (solid lines) and $|F = 4, m_F = -4\rangle$ (dashed lines).

a state $|j\rangle = |F, m_F\rangle$ can be expressed in the form [103]

$$U_{|j\rangle}(y, \theta) = -V_{|j\rangle}(\theta) - W_{|j\rangle}(\theta) \cos^2[2\pi y/\lambda_{\mathrm{DT}} + \vartheta_{|j\rangle}(\theta)], \qquad (5.15)$$

composed of an effective offset $V_{|j\rangle}(\theta)$, an effective contrast $W_{|j\rangle}(\theta)$ and an effective phase $\vartheta_{|j\rangle}(\theta)$. The trap depth is thus given by

$$U_{0,|j\rangle}(\theta) = \max |U_{|j\rangle}(y, \theta)| = V_{|j\rangle}(\theta) + W_{|j\rangle}(\theta). \qquad (5.16)$$

The effective contrast W determines the axial oscillation frequency ν_{ax} of the atoms, see Fig. 5.8 (a). In the harmonic approximation of the potential it is given by [103]

$$\nu_{\mathrm{ax},|j\rangle}(\theta) = \sqrt{\frac{2W_{|j\rangle}(\theta)}{m\lambda_{\mathrm{DT}}^2}}. \qquad (5.17)$$

I have calculated offset, contrast and axial trap frequencies for the states $|j\rangle = |3, -3\rangle$ and $|j\rangle = |4, -4\rangle$ for typical trap parameters ($\lambda_{\mathrm{DT}} = 1030\,\mathrm{nm}$, $P_{\mathrm{tot}} = 3.6\,\mathrm{W}$, $w_{\mathrm{DT}} = 45\,\mu\mathrm{m}$) according to [103]. With increasing θ, the contrast decreases and the offset increases in a non-linear way, see Fig. 5.8 (b). For angles $\theta \gtrsim 70°$, all three quantities become significantly different for the two states. The relative displacement between the effective potentials for the two states

$$\Delta y(\theta) = \lambda_{\mathrm{DT}} |\vartheta_{|3,-3\rangle}(\theta) - \vartheta_{|4,-4\rangle}(\theta)|/2\pi \qquad (5.18)$$
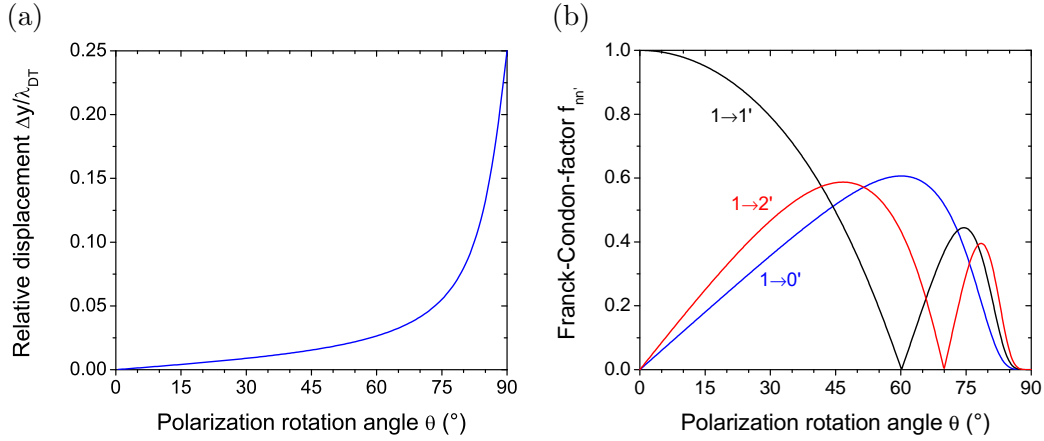
(a)

(b)

Figure 5.9: (a) Relative displacement of the two effective potentials with respect to each other, in units of the trapping laser wavelength λ_{DT}. (b) Franck-Condon factors for transitions between vibrational states $n \to n'$.

is strongly non-linear[2] and approaches its maximum value $\lambda_{\mathrm{DT}}/4$ at $\theta = 90°$, see Fig. 5.9 (a). According to [97], I have calculated the Franck-Condon factors using both the exact eigenfunctions of the periodic potentials (Bloch functions) and of a harmonic oscillator potential, which is a very good approximation for the lowest vibrational states of individual wells in our optical lattice. Starting from $|F = 4, m_F = 4, n = 1\rangle$, the results for the carrier transition $(n = 1 \to n' = 1)$, the red sideband $(1 \to 2')$ and the blue sideband transition $(1 \to 0')$ are shown in Fig. 5.9 (b). The difference between the results of the two methods is negligible for such low vibrational quantum numbers and the simpler harmonic approximation can be used.

Sideband thermometry

The ability to drive sideband transition can give us information about the occupation of the vibrational states. The 'smoking gun' for ground-state cooling is the disappearance of the blue sideband $(n \to n - 1)$: Atoms in $n = 0$ cannot be transferred to a lower vibrational state since they are already in the lowest possible state.

For the probability $p(n_{\mathrm{ax}})$ of an atom to be in the axial vibrational state n_{ax}, I assume a thermal distribution with temperature T_{ax}. The ratio of the occupation

---

[2]If the state $|3, -3\rangle$ ($|4, -4\rangle$) would only couple to the σ^+ (σ^-) component, the dependence would be perfectly linear.

probabilities of two neighboring states is then given by

$$\frac{p(n_{\mathrm{ax}}+1)}{p(n_{\mathrm{ax}})} = \exp\left(-\frac{h\nu_{\mathrm{ax}}}{k_{\mathrm{B}}T_{\mathrm{ax}}}\right) \equiv \xi \quad \text{or} \tag{5.19}$$

$$p(n_{\mathrm{ax}}) \propto \exp\left(-\frac{h\nu_{\mathrm{ax}}}{k_{\mathrm{B}}T_{\mathrm{ax}}}\right)^{n_{\mathrm{ax}}} = \xi^{n_{\mathrm{ax}}}, \tag{5.20}$$

where ξ is the Boltzmann factor. Red sideband (or carrier) transitions can in principle be driven from all states $n \geq 0$, but the (first) blue sideband transition only from $n \geq 1$. Therefore, the ratio $P_{\mathrm{blue}}/P_{\mathrm{red}}$ between the blue and red sideband (carrier) transfer probabilities equals the fraction of atoms which are *not* in the ground state

$$p(n_{\mathrm{ax}} > 0) = \frac{P_{\mathrm{blue}}}{P_{\mathrm{red}}} = \frac{\sum_{m=1}^{\infty}\xi^m}{\sum_{m=0}^{\infty}\xi^m} = \xi. \tag{5.21}$$

Conversely, the ground state occupation is given by

$$p_{0,\mathrm{ax}} = 1 - \xi = 1 - \frac{P_{\mathrm{blue}}}{P_{\mathrm{red}}}. \tag{5.22}$$

The mean vibrational quantum number and the axial temperature are given by

$$\langle n_{\mathrm{ax}}\rangle = \frac{\sum_{m=0}^{\infty}m\xi^m}{\sum_{m=0}^{\infty}\xi^m} = \frac{1}{\xi^{-1}-1} \quad \text{and} \tag{5.23}$$

$$T_{\mathrm{ax}} = \frac{h\nu_{\mathrm{ax}}}{k_{\mathrm{B}}\ln(\xi^{-1})}, \tag{5.24}$$

respectively.

To get an idea in which regime we already are with our standard cooling technique: From previous measurements [37], we expect a temperature of about $30\,\mu\mathrm{K}$ for atoms in the dipole trap which are cooled by the optical molasses beams. Assuming a typical trap frequency of $\nu_{\mathrm{ax}} = 280\,\mathrm{kHz}$, we expect a mean vibrational quantum number of about $\langle n_{\mathrm{ax}}\rangle = 1.8$. This is already close to the axial ground state and only the lowest vibrational states are populated.

5.3.2 Microwave sideband spectra

In our experiment, we perform microwave spectroscopy as follows: After counting the atoms in the MOT and loading them into the dipole trap, the atoms are optically pumped to the state $|F = 4, m_F = -4\rangle$. This is done using a circularly polarized pumping beam[3] and a guiding magnetic field $B_y = 0.4\,\mathrm{G}$ along the dipole trap axis, see also section 1.3.3. Then, a microwave pulse with a constant power and a duration Δt_{MW} is shone onto the atoms (Agilent 8375A + 5 W amplifier), eventually transferring population to $|F = 3, m_F = -3\rangle$. The final state is detected using a state-selective push-out-beam, removing all atoms in $|F = 4\rangle$ from the trap. The

---

[3]resonant with the $|F = 4\rangle \to |F' = 4\rangle$ transition, intensity ca. $0.4\,\mathrm{mW/cm^2}$, duration: ca. $1\,\mathrm{ms}$
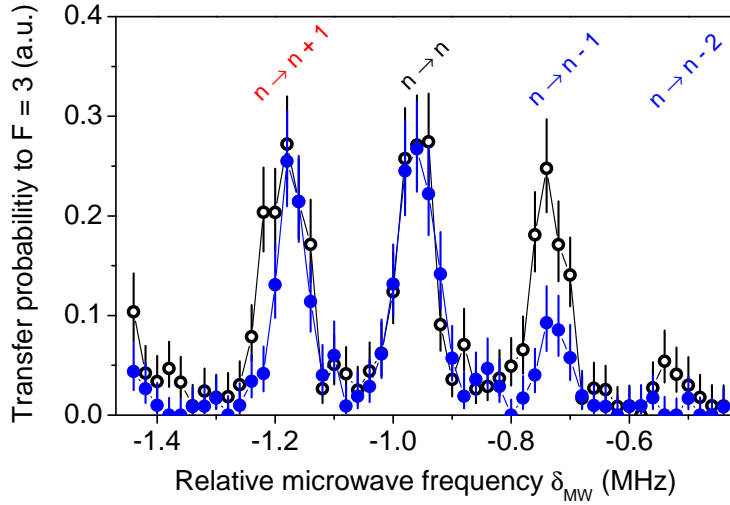
Figure 5.10: Microwave sideband spectra: The transfer probability to $|F = 3\rangle$ (survival probability after push-out) is measured as a function of the relative microwave frequency. The blue sidebands $n \to n-1$ and $n \to n-2$ are strongly reduced for the EIT-cooled atomic sample (filled circles) when compared to the molasses-cooled sample (open circles).

fraction of atoms that are detected after loading them back to the MOT is thus a measure for the transfer probability to $|F = 3\rangle$.

Driving resonant Rabi oscillations on the $|4, -4\rangle \to |3, -3\rangle$ transition in the state-independent optical lattice ($\theta = 0$) with maximum microwave power (ca. 5 W) yields a 'bare' Rabi frequency of $\Omega_{\mathrm{bare}}/2\pi = 31\,\mathrm{kHz}$, corresponding to a π-pulse duration of $\Delta t_{\mathrm{MW}} = 16\,\mu\mathrm{s}$. To shift the effective potentials for the two states with respect to each other, a half-wave plate (HWP) is used, rotating the polarization of one dipole-trap beam by typically $\theta = 26°$ with respect to the polarization of the other beam. For this setting, the expected Franck-Condon factors $f_{nn'}$ and Rabi frequencies for the transitions $n \leftrightarrow n'$ are listed in table 5.2.

We record microwave sideband spectra in such a state-dependent lattice by measuring the transfer probability to $|F = 3\rangle$ as a function of the relative microwave frequency $\delta_{\mathrm{MW}} \equiv \nu_{\mathrm{MW}} - \Delta\nu_{\mathrm{HFS}}$, see Fig. 5.10. We use pulses with maximum power and a duration of $\Delta t_{\mathrm{MW}} = 24\,\mu\mathrm{s}$. In this case, we take spectra with EIT-cooled atoms and with atoms that are cooled by the optical molasses beams only. Both spectra show three to four equally spaced peaks, which, except of the central peak, disappear when the HWP is removed ($\theta = 0$). Thus the central peak corresponds to the carrier transition and the other peaks to sideband transitions. The position $\delta_{\mathrm{MW}} = -0.96\,\mathrm{MHz}$ of the central peak is due to a magnetic offset field of $|B| = 0.4\,\mathrm{G}$, see also section 1.3.3.

From the relative peak positions I infer the oscillation frequency along the dipole trap axis. For the molasses-cooled sample, I obtain an axial trap frequency of

	$n' = n$		$n' = n + 1$	
n	$f_{nn'}$	$\Omega_{nn'}/2\pi$	$f_{nn'}$	$\Omega_{nn'}/2\pi$
0	0.95	29 kHz	0.31	10 kHz
1	0.85	26 kHz	0.42	13 kHz
2	0.75	23 kHz	0.48	15 kHz
3	0.66	20 kHz	0.52	16 kHz

Table 5.2: Expected Franck-Condon factors $f_{nn'}$ and Rabi frequencies for the transitions $n \leftrightarrow n$ and $n \leftrightarrow n + 1$, respectively.

$\nu_{\mathrm{ax}} = (220 \pm 2)\,\mathrm{kHz}$, which is only 81% of the value one infers from the calculated effective standing wave contrast $W_{|j\rangle}(\theta = 26°)$, see Fig. 5.8 (a). This discrepancy might arise from a non-perfect overlap of the two beams or an underestimated beam waist $w_{\mathrm{DT,MOT}}$ at the MOT position.

Concerning the height of the peaks, the EIT-cooled sample shows a substantial reduction of the first blue sideband ($n \to n - 1$) compared to the molasses-cooled sample, and the second blue sideband even vanishes. This is already a strong indication that with EIT-cooling a large fraction of atoms is cooled to the axial vibrational ground state of the trap: Only a minor fraction of the atoms is still in $n = 1$ or a higher state.

However, determining an axial temperature from a microwave spectrum is not straightforward: Due to the different Franck-Condon factors for the sideband transitions and their dependency on the initial (and final) vibrational state, Rabi oscillations on one and the same sideband take place with various different Rabi frequencies at the same time: When a sideband transition is resonantly driven and the population transfer is measured as a function of the pulse duration, the result is not a simple sinusoidal oscillation but a superposition of different frequency components which have to be separated by a Fourier transformation [98, 104]. This is possible but requires both a high temporal resolution and a good signal-to-noise ratio, i.e. a long measurement time.

5.3.3 Microwave sideband adiabatic passages

A simple and robust method to efficiently transfer population from one state to another is the technique of adiabatic passages [105, 106]. In contrast to drive a transition with resonant pulses, the Rabi frequency and the resonance frequency of a transition don't have to be precisely known, yet one can still achieve a population transfer close to 100%, as has been demonstrated also in our setup [107]. Here, we perform these passages on sideband transitions to determine the (axial) atomic temperature and the ground-state occupation in a robust and simple way.

A microwave adiabatic passage (AP) is performed by sweeping the microwave frequency ν_{MW} slowly over the transition frequency ν_0, going from a large negative

detuning ($\delta_0 \equiv 2\pi(\nu_{MW} - \nu_0) < 0$, $|\delta_0| \gg |\Omega_{MW}|$) to a large positive detuning ($\delta_0 > 0$, $|\delta_0| \gg |\Omega_{MW}|$). In a Bloch-vector model [2], the direction of the torque vector $\vec{\Omega}_{eff} = (\Omega_{MW}, 0, -\delta_0)$ should change much more slowly than the precession time $1/|\vec{\Omega}_{eff}|$ around this vector [106]. The Bloch vector can then adiabatically follow the torque vector from one pole of the Bloch sphere to the opposite one. The condition for adiabaticity is reflected by the following criterion [106, 107]

$$\frac{\left| \dot{\delta}_0(t)\Omega_{MW}(t) - \delta_0(t)\dot{\Omega}_{MW}(t) \right|}{2 \left[\Omega_{MW}^2(t) + \delta_0^2(t) \right]^{3/2}} \ll 1 \, . \tag{5.25}$$

On one hand, the passage should be slow enough to fulfil this criterion, on the other hand, it should be shorter than the coherence time which is of the order of several hundred microseconds [39, 107]. Here we perform a linear frequency sweep from $\delta_0/2\pi = -100\,\text{kHz}$ to $+100\,\text{kHz}$ within a time of $\tau = 10\,\text{ms}$. However, the time interval during which the direction of the Bloch vector changes significantly ($|\delta_0| \lesssim \Omega_{MW}$) is still on the order of the coherence time. By modulating the microwave power[4], we change also the Rabi frequency as a function of time, similarly to [107]

$$\Omega_{MW}(t) = \Omega_{MW,max} \times \left(a \sin^2 \left(\pi \frac{t}{\tau} \right) + b \right) \, , \tag{5.26}$$

where $a = 0.9$ is the contrast and $b = 0.1$ the offset of the modulation[5].

For all carrier transitions with $n < 8$ and all sideband transitions with $n < 21$, I expect a maximum Rabi frequency of at least $\Omega_{MW,max}/2\pi = 10\,\text{kHz}$, see table 5.2. For this value, the left hand side of Eqn. (5.25) is less than 0.02 for all values of t and even lower for higher values of $\Omega_{MW,max}$. Therefore, the adiabaticity criterion is fulfilled at least for all transitions mentioned above.

The robustness with respect to the Rabi frequency and the ability to resolve sidebands using APs are checked in the following way: The polarizations are made parallel ($\theta = 0°$) to obtain a maximum Rabi frequency for the carrier and to suppress the sidebands. First, APs are performed on the carrier transition by sweeping the frequency from $\delta_{MW} = -1.06\,\text{MHz}$ to $-0.86\,\text{MHz}$. The microwave power was attenuated by 15.7 dB, 5.7 dB and 0 dB, which correspond to maximum Rabi frequencies of $\Omega_{MW,max}/2\pi = 5, 16, 31\,\text{kHz}$. The measured transfer probabilities range from $(80 \pm 2)\%$ to $(82 \pm 2)\%$ and are thus compatible with a constant value. This means that the APs are robust for a large range of Rabi frequencies. For the resolution test, we perform APs on the first blue and the first red sideband, which should completely vanish. The measured transfer probabilities are $(1.3^{+0.4}_{-0.3})\%$ and $(2.3^{+0.5}_{-0.4})\%$, respectively. These values are compatible with a non-perfect push-out efficiency and represent the background of our measurements.
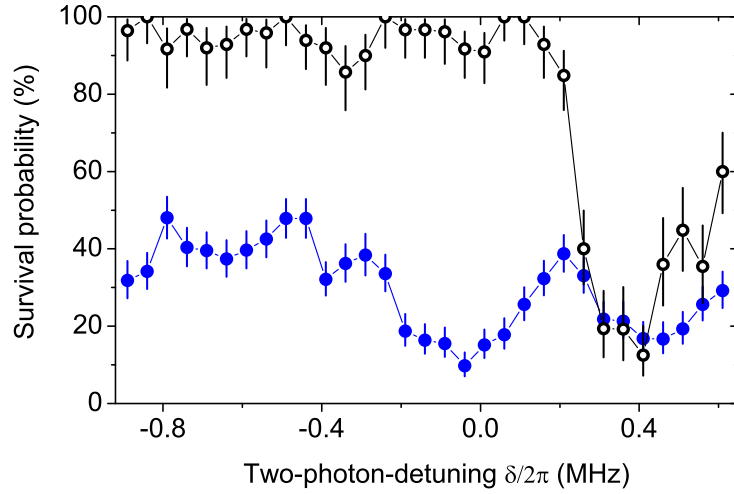
Figure 5.11: Survival probability of atoms in the standing-wave dipole trap after EIT-cooling with (full circles) and without (open circles) state-selective detection after an adiabatic passage on the blue sideband transition has been performed.

5.3.4 EIT-cooling results

Our first goal is to determine the optimal value of the two-photon-detuning δ for the EIT-cooling, i.e. where the transfer probability on the blue sideband is minimal. After an EIT-cooling pulse with a duration of $10\,\mathrm{ms}$ at a control laser power of $0.5\,\mu\mathrm{W}$, followed by optical pumping to the state $|4, -4\rangle$, we perform adiabatic passages on the blue sideband as described above and measure the transfer probability to $|F = 3\rangle$ with the push-out-technique. The result is shown in Fig. 5.11. The strength of the blue sideband has a dip at $\delta/2\pi = -(0.05 \pm 0.01)\,\mathrm{MHz}$ with a FWHM of $2\pi \times (0.33 \pm 0.04)\,\mathrm{MHz}$, obtained from a Gaussian fit. A second dip at around $\delta/2\pi = 0.4\,\mathrm{MHz}$ is not due to cooling but due to strong atom losses around $\delta/2\pi = 0.3\,\mathrm{MHz}$, when one considers also the overall survival probability of atoms in the trap, i.e. *without* applying state-selective detection (no push-out).

Having found the optimum value of δ for EIT-cooling, we are also interested in the timescale on which cooling and heating processes equilibrate. Then, the system has reached its steady-state and the mean vibrational quantum number and the temperature have attained their lowest values. The strength of the blue sideband as a function of the duration of the EIT-cooling pulse is shown in Fig. 5.12. Fitting the data with an exponential decay function reveals a time constant of $\tau_{\mathrm{cool}} = (1.62 \pm 0.12)\,\mathrm{ms}$ and an offset of $(18 \pm 1)\%$. Thus a EIT-cooling pulse duration of $(5 \ldots 10)\,\mathrm{ms}$ seems to be sufficient to reach the equilibrium. Moreover,

---

[4]using the analog modulation input of the Agilent 8375A

[5]In contrast to the setup described in [107], $a < 1$ and $b > 0$ due to technical reasons.
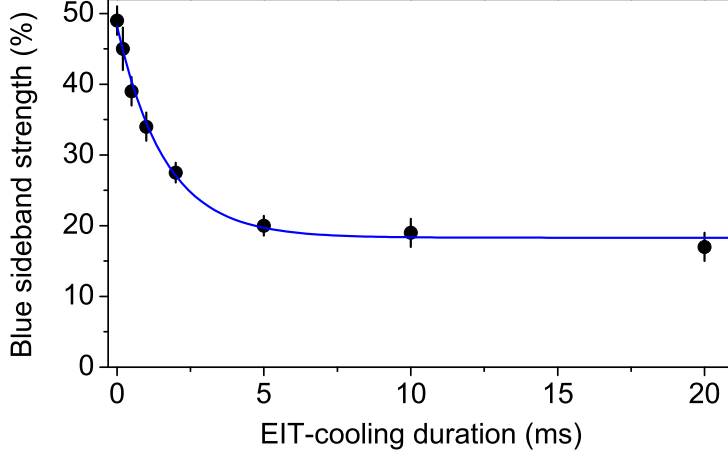
Figure 5.12: Strength of the blue sideband as a function of the duration of the EIT-cooling pulse. The solid line shows a fit of an exponential decay function to the data.

I compare our value for the cooling rate $1/\tau_{\rm cool} = (0.62 \pm 0.05)\,{\rm ms}^{-1}$ with the theoretical prediction (Eqn. (33) in [108])

$$W^{\rm max} \sim \frac{\eta^2 \Omega_{\rm con}^2 \Omega_{\rm p}^2}{2\gamma(\Omega_{\rm p}^2 + \Omega_{\rm con}^2)} \approx \frac{\eta^2 \Omega_{\rm p}^2}{2\gamma} \approx 3\,{\rm ms}^{-1}\,, \tag{5.27}$$

which is on the same order of magnitude. However, the theoretical model assumes an ideal three-level atom in a state-independent, harmonic trapping potential. Moreover, it does not take into account technical heating sources in our setup, e.g. intensity and phase noise of the trapping lasers.

Finally, I determine the axial temperature $T_{\rm ax}$, the mean vibrational quantum number $\langle n_{\rm ax} \rangle$ and the ground state occupation $p_{0,\rm ax}$ that can be reached with EIT-cooling and compare it with our molasses cooling. For this, we perform adiabatic passages on both the blue and the red sideband and determine their transfer ratio ξ. For the EIT-cooling, we choose a pulse duration of $10\,{\rm ms}$ at the optimal cooling detuning of $\delta/2\pi = -0.04\,{\rm MHz}$. Using equations (5.22)–(5.24), I obtain the results listed in table 5.3.

Cooling method	ξ	$T_{\rm ax}/\mu{\rm K}$	$\langle n_{\rm ax} \rangle$	$p_{0,\rm ax}$
EIT	0.22 ± 0.02	7.0 ± 0.5	0.29 ± 0.04	0.78 ± 0.02
Molasses	0.71 ± 0.05	31 ± 6	2.5 ± 0.6	0.29 ± 0.05

Table 5.3: Transfer ratio ξ, axial temperature $T_{\rm ax}$, mean vibrational quantum number $\langle n_{\rm ax} \rangle$ and ground state occupation $p_{0,\rm ax}$ for EIT and molasses cooling.

Almost 80% of the atoms are cooled to the axial ground state of the trap by the EIT-cooling compared to only about one third for the molasses cooled atoms. The temperature of the latter is compatible with the values of about 30 µK which have also been determined by other methods. However, for the EIT-cooling one can only claim so far that the atoms are cooled along the trap axis but not along the other spatial dimensions, as has been shown for the molasses-cooled atoms. It could even be that the atoms are hotter along the radial direction in the EIT case compared to the molasses cooling. In order to determine a temperature in 3D one would need, for example, a release-recapture technique [109].

5.4 Summary and conclusions

In this chapter I have presented our results on EIT-cooling. For both the measurements inside or outside of the cavity, we observe strong cooling effects in a narrow region around the two-photon resonance, as is expected for EIT-cooling. The experimental implementation of the scheme is relatively simple and robust. The cooling manifests itself by increased trapping times since it counteracts heating mechanisms. With atoms trapped outside of the cavity, we show that the cooling is at least effective along the strongly confined axis of the standing-wave optical dipole trap. Applying microwave adiabatic passages on sideband transition, we demonstrate that an axial ground-state occupation of almost 80% can be reached within a few milliseconds.

Since the atoms inside the cavity are even strongly confided along two axes, the atoms are presumably EIT-cooled along these directions. However, this cavity-EIT system is much more complex to understand and to investigate experimentally, since additional cooling effects relying on the atom-cavity coupling and other (technical) heating effects play also an important role. Moreover, when the trapping frequency becomes larger than the cavity linewidth 2κ, resolved-sideband cavity-cooling can occur [110]. Although still theoretically challenging, we could utilize the cooling effect to strongly enhance the trapping time of atoms inside the cavity and to increase the atom-cavity coupling strength g, see section 4.4.3.

6 Outlook

Finally, I present some ideas which could be realized in our setup in the near future, or in a more advanced experiment in the far future.

EIT-cooling

Cooling of atoms to temperatures far below the Doppler limit is of great interest in our setup since all our experiments rely on a good localization of the atoms within the cavity mode. The EIT-cooling observed here could be further developed to achieve strong cooling in all three dimensions. First, the confinement along the direction perpendicular to the dipole trap and the cavity axis should be improved to get deeper into the Lamb-Dicke regime, a prerequisite for cooling to the motional ground-state. Second, the beam directions should be chosen such that the difference wave vector $\Delta \vec{k}$ has a component in each of the three directions. This could be achieved by changing the direction of the control laser beam in the $x - y$-plane.

Concerning the model of EIT-cooling inside the cavity, there is already significant progress in the group of G. Morigi based on [108,111]. On the experimental side, we would like to distinguish the cooling effects that are due to the interaction with the cavity mode from those due to the coupling to the control laser. For this purpose, one would need to explore a broader range of parameters, e.g. change also the atom-cavity detuning.

Two-mode cavity-EIT

At the single-particle level, the control of optical properties with light can be utilized for atom-light quantum interfaces [112]. Nonlinearities can lead to an effective photon-photon interaction, forming the basis of quantum logic gates [113, 114]. However, in our case, still many photons are needed in the control laser beam to change the optical properties of the atom. Using a second cavity mode to enhance the interaction with the control beam could lead to an optical transistor for single photons. For this, one could couple four atomic states in an N-type scheme by two cavity modes g_1 and g_2 and a classical coupling field Ω, see Fig. 6.1 (a) and [115,116]. Analogous to the quantum model of cavity-EIT (see section 3.3), I simulated the steady-state normalized transmission of a weak probe beam resonantly coupled to the g_1 mode, populating it on average with $n_{\mathrm{p},0}^{(1)} = 10^{-3}$ photons if there is no atom inside, see Fig. 6.1 (b). Moreover, for the coupling strengths and the decay rates, I assumed typical values of our current setup: $(g_1, g_2, \Omega, \kappa, \gamma)/2\pi = (5, 5, 50, 0.4, 2.6)\,\mathrm{MHz}$. If the control mode g_2 is not populated, there is no coupling
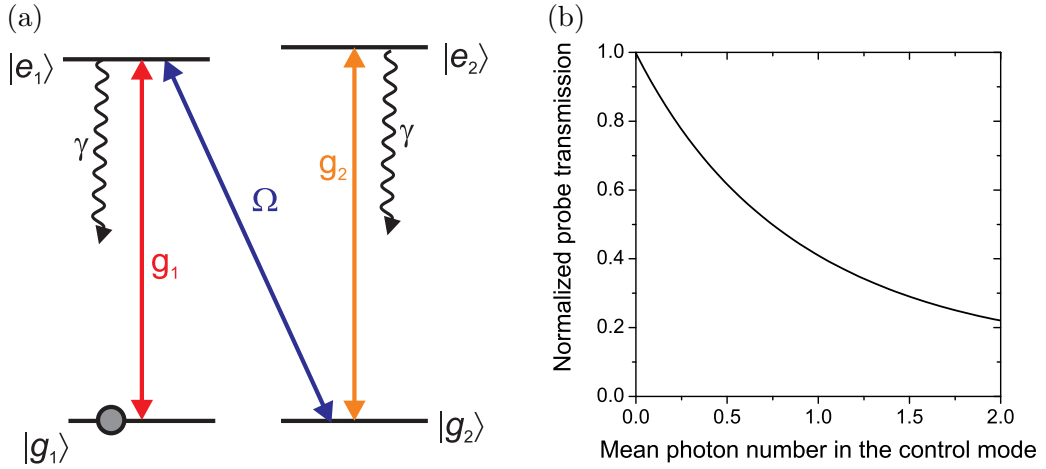
(a)

(b)

Figure 6.1: (a) Four-level atom with two ground states and two excited states, coupled to two different cavity modes with strengths g_1 and g_2 and to a classical coupling field Ω. For weak excitation of the first cavity mode g_1, the atom stays in the state $|g_1\rangle$. (b) Normalized transmission of the probe laser, weakly coupled into the first cavity mode g_1, as a function of the mean photon number in the second cavity mode g_2 pumped by a control beam.

to the second excited state $|e_2\rangle$. The system is then effectively a three-level EIT-system with full transmission at two-photon resonance between the probe field g_1 and the coupling field Ω. When one increases the photon number in the control mode g_2, this leads to a shift or splitting of the ground state $|g_2\rangle$, changing the two-photon resonance condition. The normalized transmission of the probe beam drops already below 50% for less than one photon in the control mode. With cesium, the four-level scheme could be realized using two adjacent Zeeman sublevels of the $|F = 4\rangle$ ground state and two sublevels of the $|F' = 3\rangle$ excited state, coupled by two orthogonally polarized cavity modes. In conclusion, with realistic experimental parameters, one is already in the regime of optical switching with single photons.

Bibliography

[1] H. A. Lorentz, *The theory of electrons and its applications to the phenomena of light and radiant heat*, B.G. Teubner, Leipzig (1916), URL `http://www.archive.org/details/electronstheory00lorerich`

[2] F. Bloch, *Nuclear induction*, Phys. Rev. **70**, 460 (1946)

[3] S. A. Aljunid, M. K. Tey, B. Chng, T. Liew, G. Maslennikov, V. Scarani, and C. Kurtsiefer, *Phase shift of a weak coherent beam induced by a single atom*, Phys. Rev. Lett. **103**, 153601 (2009)

[4] P. R. Berman (ed.), *Cavity Quantum Electrodynamics*, Academic Press, San Diego (1994)

[5] S. Haroche and J.-M. Raimond, *Exploring the Quantum*, Oxford University Press (2006)

[6] H. J. Metcalf and P. van der Straten, *Laser Cooling and Trapping*, Springer-Verlag, New York (1999)

[7] M. Khudaverdyan, W. Alt, I. Dotsenko, T. Kampschulte, K. Lenhard, A. Rauschenbeutel, S. Reick, K. Schörner, A. Widera, and D. Meschede, *Controlled insertion and retrieval of atoms coupled to a high-finesse optical resonator*, New Journal of Physics **10**, 073023 (2008)

[8] E. T. Jaynes and F. W. Cummings, *Comparison of quantum and semiclassical radiation theories with application to the beam maser*, Proceedings of the IEEE **51**, 89 (1963)

[9] A. D. Boozer, A. Boca, R. Miller, T. E. Northup, and H. J. Kimble, *Cooling to the ground state of axial motion for one atom strongly coupled to an optical cavity*, Physical Review Letters **97**, 083602 (2006)

[10] J. Bochmann, M. Mücke, C. Guhl, S. Ritter, G. Rempe, and D. L. Moehring, *Lossless state detection of single neutral atoms*, Phys. Rev. Lett. **104**, 203601 (2010)

[11] R. Gehr, J. Volz, G. Dubois, T. Steinmetz, Y. Colombe, B. L. Lev, R. Long, J. Estève, and J. Reichel, *Cavity-based single atom preparation and high-fidelity hyperfine state readout*, Phys. Rev. Lett. **104**, 203602 (2010)

[12] M. Khudaverdyan, W. Alt, T. Kampschulte, S. Reick, A. Thobe, A. Widera, and D. Meschede, *Quantum jumps and spin dynamics of interacting atoms in a strongly coupled atom-cavity system*, Phys. Rev. Lett. **103**, 123006 (2009)

[13] S. Reick, K. Mølmer, W. Alt, M. Eckstein, T. Kampschulte, L. Kong, R. Reimann, A. Thobe, A. Widera, and D. Meschede, *Analyzing quantum jumps of one and two atoms strongly coupled to an optical cavity*, J. Opt. Soc. Am. B **27**, A152 (2010)

[14] K. Bergmann, H. Theuer, and B. W. Shore, *Coherent population transfer among quantum states of atoms and molecules*, Rev. Mod. Phys. **70**, 1003 (1998)

[15] B. Misra and E. C. G. Sudarshan, *The Zeno's paradox in quantum theory*, J. Math. Phys. **18**, 756 (1977)

[16] W. M. Itano, D. J. Heinzen, J. J. Bollinger, and D. J. Wineland, *Quantum Zeno effect*, Phys. Rev. A **41**, 2295 (1990)

[17] C. Balzer, R. Huesmann, W. Neuhauser, and P. E. Toschek, *The quantum Zeno effect - evolution of an atom impeded by measurement*, Optics Communications **180**, 115 (2000)

[18] J. Bernu, S. Deléglise, C. Sayrin, S. Kuhr, I. Dotsenko, M. Brune, J. M. Raimond, and S. Haroche, *Freezing coherent field growth in a cavity by the quantum Zeno effect*, Phys. Rev. Lett. **101**, 180402 (2008)

[19] G. Dubois, *Préparation, manipulation et détection d'atomes uniques sur une puce à atomes*, Ph.D. thesis, Université Pierre et Marie Curie - Paris VI (2009), URL http://tel.archives-ouvertes.fr/tel-00593875/fr/

[20] S. E. Harris, J. E. Field, and A. Imamoglu, *Nonlinear optical processes using electromagnetically induced transparency*, Phys. Rev. Lett. **64**, 1107 (1990)

[21] M. Fleischhauer, A. Imamoglu, and J. P. Marangos, *Electromagnetically induced transparency: Optics in coherent media*, Rev. Mod. Phys. **77**, 633 (2005)

[22] S. E. Harris, J. E. Field, and A. Kasapi, *Dispersive properties of electromagnetically induced transparency*, Phys. Rev. A **46**, R29 (1992)

[23] L. V. Hau, S. E. Harris, Z. Dutton, and C. H. Behroozi, *Light speed reduction to 17 metres per second in an ultracold atomic gas*, Nature **397**, 594 (1999)

[24] O. Schmidt, R. Wynands, Z. Hussein, and D. Meschede, *Steep dispersion and group velocity below $\frac{c}{3000}$ in coherent population trapping*, Phys. Rev. A **53**, R27 (1996)

[25] M. Xiao, Y.-q. Li, S.-z. Jin, and J. Gea-Banacloche, *Measurement of dispersive properties of electromagnetically induced transparency in rubidium atoms*, Phys. Rev. Lett. **74**, 666 (1995)

[26] C. Liu, Z. Dutton, C. H. Behroozi, and L. V. Hau, *Observation of coherent optical information storage in an atomic medium using halted light pulses*, Nature **409**, 490 (2001)

[27] D. F. Phillips, A. Fleischhauer, A. Mair, R. L. Walsworth, and M. D. Lukin, *Storage of light in atomic vapor*, Phys. Rev. Lett. **86**, 783 (2001)

[28] U. Schnorrberger, J. D. Thompson, S. Trotzky, R. Pugatch, N. Davidson, S. Kuhr, and I. Bloch, *Electromagnetically induced transparency and light storage in an atomic Mott insulator*, Phys. Rev. Lett. **103**, 033003 (2009)

[29] L. Slodička, G. Hétet, S. Gerber, M. Hennrich, and R. Blatt, *Electromagnetically induced transparency from a single atom in free space*, Phys. Rev. Lett. **105**, 153604 (2010)

[30] T. Kampschulte, W. Alt, S. Brakhane, M. Eckstein, R. Reimann, A. Widera, and D. Meschede, *Optical control of the refractive index of a single atom*, Phys. Rev. Lett. **105**, 153603 (2010)

[31] M. Mücke, E. Figueroa, J. Bochmann, C. Hahn, K. Murr, S. Ritter, C. J. Villas-Boas, and G. Rempe, *Electromagnetically induced transparency with single atoms in a cavity*, Nature **465**, 755 (2010)

[32] G. Morigi, J. Eschner, and C. H. Keitel, *Ground state laser cooling using electromagnetically induced transparency*, Phys. Rev. Lett. **85**, 4458 (2000)

[33] C. F. Roos, D. Leibfried, A. Mundt, F. Schmidt-Kaler, J. Eschner, and R. Blatt, *Experimental demonstration of ground state laser cooling with electromagnetically induced transparency*, Phys. Rev. Lett. **85**, 5547 (2000)

[34] F. Schmidt-Kaler, J. Eschner, G. Morigi, C. Roos, D. Leibfried, A. Mundt, and R. Blatt, *Laser cooling with electromagnetically induced transparency: Application to trapped samples of ions or neutral atoms*, Appl. Phys. B: Lasers Opt. **73**, 807 (2001)

[35] W. Alt, *Optical control of single neutral atoms*, Ph.D. thesis, Universität Bonn (2004), URL `http://nbn-resolving.de/urn:nbn:de:hbz:5N-04297`

[36] I. Dotsenko, *Single atoms on demand for cavity QED experiments*, Ph.D. thesis, Universität Bonn (2007), URL `http://nbn-resolving.de/urn:nbn:de:hbz:5N-10697`

[37] M. Khudaverdyan, *A controlled one and two atom-cavity system*, Ph.D. thesis, Universität Bonn (2009), URL `http://nbn-resolving.de/urn:nbn:de:hbz:5N-18880`

[38] S. Reick, *Internal and external dynamics of a strongly-coupled atom-cavity system*, Ph.D. thesis, Universität Bonn (2010), URL `http://nbn-resolving.de/urn:nbn:de:hbz:5N-19901`

[39] D. Schrader, *A neutral atom quantum register*, Ph.D. thesis, Universität Bonn (2004), URL `http://nbn-resolving.de/urn:nbn:de:hbz:5N-04870`

[40] S. Kuhr, *A controlled quantum system of individual neutral atoms*, Ph.D. thesis, Universität Bonn (2003), URL `http://nbn-resolving.de/urn:nbn:de:hbz:5n-01913`

[41] Y. Miroshnychenko, *An atom-sorting machine*, Ph.D. thesis, Universität Bonn (2006), URL `http://nbn-resolving.de/urn:nbn:de:hbz:5N-08430`

[42] W. Rosenfeld, *A high finesse optical resonator for cavity QED experiments*, Diplom thesis, Universität Bonn (2003), URL `http://quantum-technologies.iap.uni-bonn.de`

[43] M. Khudaverdyan, *Addressing of individual atoms in an optical dipole trap*, Diplom thesis, Universität Bonn (2003), URL `http://quantum-technologies.iap.uni-bonn.de/`

[44] A. Stiebeiner, *Deterministische Kopplung eines einzelnen Atoms an die Mode eines Resonators hoher Finesse*, Diplom thesis, Universität Bonn (2007), URL `http://quantum-technologies.iap.uni-bonn.de/`

[45] K. Lenhard, *Stabilisierung eines Resonators hoher Finesse zur Atom-Lichtfeld-Kopplung*, Diplom thesis, Universität Bonn (2008), URL `http://quantum-technologies.iap.uni-bonn.de/`

[46] K. Schörner, *Ein phasenstabilisiertes Lasersystem für resonatorinduzierte Raman-Prozesse*, Diplom thesis, Universität Bonn (2008), URL `http://quantum-technologies.iap.uni-bonn.de/`

[47] A. Thobe, *Quantum jumps of one and two atoms in a strongly coupled atom-cavity system*, Diplom thesis, Humboldt-Universität zu Berlin (2009), URL `http://quantum-technologies.iap.uni-bonn.de/`

[48] M. Eckstein, *Three-level physics of a single atom coupled to a high finesse cavity*, Diplom thesis, Universität Bonn (2010), URL `http://quantum-technologies.iap.uni-bonn.de/`

[49] S. Brakhane, *Kontrolle der Atom-Resonator-Wechselwirkung mit Hilfe einer Regelschleife*, Diplom thesis, Universität Bonn (2011), URL `http://quantum-technologies.iap.uni-bonn.de/`

[50] W. Alt, *An objective lens for efficient fluorescence detection of single atoms*, Optik - International Journal for Light and Electron Optics **113**, 142 (2002)

[51] L. Förster, W. Alt, I. Dotsenko, M. Khudaverdyan, D. Meschede, Y. Miroshnychenko, S. Reick, and A. Rauschenbeutel, *Number-triggered loading and collisional redistribution of neutral atoms in a standing wave dipole trap*, New Journal of Physics **8**, 259 (2006)

[52] R. Grimm, M. Weidemüller, and Y. B. Ovchinnikov, *Optical dipole traps for neutral atoms*, Advances in Atomic, Molecular, and Optical Physics **42**, 95 (2000)

[53] Y. Miroshnychenko, D. Schrader, S. Kuhr, W. Alt, I. Dotsenko, M. Khudaverdyan, A. Rauschenbeutel, and D. Meschede, *Continued imaging of the transport of a single neutral atom*, Opt. Express **11**, 3498 (2003)

[54] I. Dotsenko, W. Alt, M. Khudaverdyan, S. Kuhr, D. Meschede, Y. Miroshnychenko, D. Schrader, and A. Rauschenbeutel, *Submicrometer position control of single trapped neutral atoms*, Phys. Rev. Lett. **95**, 033002 (2005)

[55] D. Meschede, *Optics, Light and Lasers*, Wiley-VCH, Weinheim (2006)

[56] P. Domokos and H. Ritsch, *Mechanical effects of light in optical resonators*, J. Opt. Soc. Am. B **20**, 1098 (2003)

[57] S. Nußmann, K. Murr, M. Hijlkema, B. Weber, A. Kuhn, and G. Rempe, *Vacuum-stimulated cooling of single atoms in three dimensions*, Nature Physics **1**, 122 (2005)

[58] R. W. P. Drever, J. L. Hall, F. V. Kowalski, J. Hough, G. M. Ford, A. J. Munley, and H. Ward, *Laser phase and frequency stabilization using an optical resonator*, Applied Physics B: Lasers and Optics **31**, 97 (1983)

[59] O. Föllinger, *Regelungstechnik*, AEG-TELEFUNKEN AG, Berlin, Frankfurt am Main (1980)

[60] S. Kuhr, W. Alt, D. Schrader, I. Dotsenko, Y. Miroshnychenko, W. Rosenfeld, M. Khudaverdyan, V. Gomer, A. Rauschenbeutel, and D. Meschede, *Coherence properties and quantum state transportation in an optical conveyor belt*, Phys. Rev. Lett. **91**, 213002 (2003)

[61] D. Schrader, I. Dotsenko, M. Khudaverdyan, Y. Miroshnychenko, A. Rauschenbeutel, and D. Meschede, *Neutral atom quantum register*, Phys. Rev. Lett. **93**, 150501 (2004)

[62] A. D. Boozer, A. Boca, R. Miller, T. E. Northup, and H. J. Kimble, *Reversible state transfer between light and a single trapped atom*, Phys. Rev. Lett. **98**, 193601 (2007)

[63] A. Kuhn, M. Hennrich, and G. Rempe, *Deterministic single-photon source for distributed quantum networking*, Physical Review Letters **89**, 067901 (2002)

[64] J. McKeever, A. Boca, A. D. Boozer, R. Miller, J. R. Buck, A. Kuzmich, and H. J. Kimble, *Deterministic generation of single photons from one atom trapped in a cavity*, Science **303**, 1992 (2004)

[65] L. You, X. X. Yi, and X. H. Su, *Quantum logic between atoms inside a high-Q optical cavity*, Physical Review A **67**, 032308 (2003)

[66] B. W. Shore, *The Theory of Coherent Atomic Excitation, Volume 2, Multi-level Atoms and Incoherence*, John Wiley & Sons Inc. (1990)

[67] I. Dotsenko, *Raman spectroscopy of single atoms*, Diplom thesis, Universität Bonn (2002), URL http://quantum-technologies.iap.uni-bonn.de/

[68] D. Haubrich, M. Dornseifer, and R. Wynands, *Lossless beam combiners for nearly equal laser frequencies*, Review of Scientific Instruments **71**, 338 (2000)

[69] V. B. Braginsky, Y. I. Vorontsov, and K. S. Thorne, *Quantum nondemolition measurements*, Science **209**, 547 (1980)

[70] A. S. Sørensen and K. Mølmer, *Measurement induced entanglement and quantum computation with atoms in optical cavities*, Physical Review Letters **91**, 097905 (2003)

[71] J. C. Berquist, R. G. Hulet, W. Itano, and D. J. Wineland, *Observation of quantum jumps in a single atom*, Physical Review Letters **57**, 1669 (1986)

[72] W. M. Itano, J. Berquist, R. G. Hulet, and D. Wineland, *Radiative decay rates in Hg^+ from observations of quantum jumps in a single ion*, Physical Review Letters **59**, 2732 (1987)

[73] S. Gleyzes, S. Kuhr, C. Guerlin, J. Bernu, S. Deleglise, U. B. Hoff, M. Brune, J.-M. Raimond, and S. Haroche, *Quantum jumps of light recording the birth and death of a photon in a cavity*, Nature **446**, 297 (2007)

[74] D. S. Sivia, *Data Analysis: A Bayesian Tutorial*, Oxford University Press (2006)

[75] A. R. R. Carvalho and J. J. Hope, *Stabilizing entanglement by quantum-jump-based feedback*, Physical Review A **76**, 010301 (2007)

[76] A. R. R. Carvalho, A. J. S. Reid, and J. J. Hope, *Controlling entanglement by direct quantum feedback*, Physical Review A **78**, 012334 (2008)

[77] W. M. Itano, D. J. Heinzen, J. J. Bollinger, and D. J. Wineland, *Quantum Zeno effect*, Phys. Rev. A **41**, 2295 (1990)

[78] L. S. Schulman, *Continuous and pulsed observations in the quantum Zeno effect*, Phys. Rev. A **57**, 1509 (1998)

[79] E. W. Streed, J. Mun, M. Boyd, G. K. Campbell, P. Medley, W. Ketterle, and D. E. Pritchard, *Continuous and pulsed quantum Zeno effect*, Phys. Rev. Lett. **97**, 260402 (2006)

[80] D. A. Steck, *Cesium D line data* (23 January 1998, Revision 2.1.2, 12 August 2009), URL http://steck.us/alkalidata/

[81] E. M. Purcell, *Proceedings of the american physical society*, Phys. Rev. **69**, 681 (1946)

[82] E. Figueroa, F. Vewinger, J. Appel, and A. I. Lvovsky, *Decoherence of electromagnetically induced transparency in atomic vapor*, Opt. Lett. **31**, 2625 (2006)

[83] M. D. Lukin, M. Fleischhauer, M. O. Scully, and V. L. Velichansky, *Intracavity electromagnetically induced transparency*, Opt. Lett. **23**, 295 (1998)

[84] G. Hernandez, J. Zhang, and Y. Zhu, *Vacuum rabi splitting and intracavity dark state in a cavity-atom system*, Phys. Rev. A **76**, 053814 (2007)

[85] B. Lounis and C. Cohen-Tannoudji, *Coherent population trapping and Fano profiles*, J. Phys. II France **2**, 579 (1992)

[86] H. Carmichael, *An Open Systems Approach to Quantum Optics*, Springer, Berlin (1993)

[87] S. M. Tan, *A computational toolbox for quantum and atomic optics*, Journal of Optics B: Quantum and Semiclassical Optics **1**, 424 (1999)

[88] A. D. Boozer, A. Boca, J. R. Buck, J. McKeever, and H. J. Kimble, *Comparison of theory and experiment for a one-atom laser in a regime of strong coupling*, Physical Review A **70**, 023814 (2004)

[89] S. L. Meyer, *Data analyis for scientists and engineers*, John Wiley & Sons Inc., New York (1975)

[90] S. Kuhr, W. Alt, D. Schrader, I. Dotsenko, Y. Miroshnychenko, A. Rauschenbeutel, and D. Meschede, *Analysis of dephasing mechanisms in a standing-wave dipole trap*, Phys. Rev. A **72**, 023406 (2005)

[91] K. M. Birnbaum, A. S. Parkins, and H. J. Kimble, *Cavity QED with multiple hyperfine levels*, Physical Review A **74**, 063802 (2006)

[92] D. J. Wineland and W. M. Itano, *Laser cooling of atoms*, Phys. Rev. A **20**, 1521 (1979)

[93] C. Monroe, D. M. Meekhof, B. E. King, S. R. Jefferts, W. M. Itano, D. J. Wineland, and P. Gould, *Resolved-sideband Raman cooling of a bound atom to the 3D zero-point energy*, Phys. Rev. Lett. **75**, 4011 (1995)

[94] F. Diedrich, J. C. Bergquist, W. M. Itano, and D. J. Wineland, *Laser cooling to the zero-point energy of motion*, Phys. Rev. Lett. **62**, 403 (1989)

[95] S. Stenholm, *The semiclassical theory of laser cooling*, Rev. Mod. Phys. **58**, 699 (1986)

[96] H. Rohde, S. T. Gulde, C. F. Roos, P. A. Barton, D. Leibfried, J. Eschner, F. Schmidt-Kaler, and R. Blatt, *Sympathetic ground-state cooling and coherent manipulation with two-ion crystals*, Journal of Optics B: Quantum and Semiclassical Optics **3**, S34 (2001)

[97] L. Förster, *Microwave control of atomic motion in a spin dependent optical lattice*, Ph.D. thesis, Universität Bonn (2010), URL `http://nbn-resolving.de/urn:nbn:de:hbz:5N-22879`

[98] L. Förster, M. Karski, J.-M. Choi, A. Steffen, W. Alt, D. Meschede, A. Widera, E. Montano, J. H. Lee, W. Rakreungdet, and P. S. Jessen, *Microwave control of atomic motion in optical lattices*, Phys. Rev. Lett. **103**, 233001 (2009)

[99] J. D. Miller, R. A. Cline, and D. J. Heinzen, *Far-off-resonance optical trapping of atoms*, Phys. Rev. A **47**, R4567 (1993)

[100] J. P. Gordon and A. Ashkin, *Motion of atoms in a radiation trap*, Physical Review A **21**, 1606 (1980)

[101] C. Cohen-Tannoudji, J. Dupont-Roc, and G. Grynberg, *Atom-Photon Interactions: Basic Processes and Applications*, Wiley-VCH (1998)

[102] E. Condon, *A theory of intensity distribution in band systems*, Phys. Rev. **28**, 1182 (1926)

[103] M. Karski, *State-selective transport of single neutral atoms*, Ph.D. thesis, Universität Bonn (2010), URL `http://nbn-resolving.de/urn:nbn:de:hbz:5N-23401`

[104] D. M. Meekhof, C. Monroe, B. E. King, W. M. Itano, and D. J. Wineland, *Generation of nonclassical motional states of a trapped atom*, Phys. Rev. Lett. **76**, 1796 (1996)

[105] L. Allen and J. H. Eberly, *Optical Resonance and Two-level Atoms*, Wiley, New York (1975)

[106] N. V. Vitanov, T. Halfmann, B. W. Shore, and K. Bergmann, *Laser-induced population transfers by adiabatic passage techniques*, Annual Review of Physical Chemistry **52**, 763 (2001)

[107] M. Khudaverdyan, W. Alt, I. Dotsenko, L. Förster, S. Kuhr, D. Meschede, Y. Miroshnychenko, D. Schrader, and A. Rauschenbeutel, *Adiabatic quantum state manipulation of single trapped atoms*, Phys. Rev. A **71**, 031404 (2005)

[108] G. Morigi, *Cooling atomic motion with quantum interference*, Phys. Rev. A **67**, 033402 (2003)

[109] C. Tuchendler, A. M. Lance, A. Browaeys, Y. R. P. Sortais, and P. Grangier, *Energy distribution and cooling of a single atom in an optical tweezer*, Phys. Rev. A **78**, 033425 (2008)

[110] D. R. Leibrandt, J. Labaziewicz, V. Vuletić, and I. L. Chuang, *Cavity sideband cooling of a single trapped ion*, Phys. Rev. Lett. **103**, 103001 (2009)

[111] S. Zippilli and G. Morigi, *Mechanical effects of optical resonators on driven trapped atoms: Ground-state cooling in a high-finesse cavity*, Phys. Rev. A **72**, 053408 (2005)

[112] A. D. Boozer, A. Boca, R. Miller, T. E. Northup, and H. J. Kimble, *Reversible state transfer between light and a single trapped atom*, Physical Review Letters **98**, 193601 (2007)

[113] L.-M. Duan and H. J. Kimble, *Scalable photonic quantum computation through cavity-assisted interactions*, Phys. Rev. Lett. **92**, 127902 (2004)

[114] Q. A. Turchette, C. J. Hood, W. Lange, H. Mabuchi, and H. J. Kimble, *Measurement of conditional phase shifts for quantum logic*, Phys. Rev. Lett. **75**, 4710 (1995)

[115] M. Soljačić, E. Lidorikis, J. D. Joannopoulos, and L. V. Hau, *Ultralow-power all-optical switching*, Applied Physics Letters **86**, 171101 (2005)

[116] P. Bermel, A. Rodriguez, S. G. Johnson, J. D. Joannopoulos, and M. Soljacic, *Single-photon all-optical switching using waveguide-cavity quantum electrodynamics*, Phys. Rev. A **74**, 043818 (2006)

Danksagung

Hiermit möchte ich mich bedanken bei

- Herrn Prof. Dr. Dieter Meschede für die Möglichkeit in seiner Arbeitsgruppe eine Doktorarbeit anzufertigen, die Freiheit bei der Wahl des Themas und seinen Einsatz für Kontakte und Förderungsmöglichkeiten, auch über die Universität hinaus

- Herrn Prof. Dr. Jakob Reichel für die Übernahme des Zweitgutachtens

- der „dritten Etage" des Instituts für die allzeit bereite, unbürokratische Unterstützung: Annelise, Dietmar, Fien, und Ilona

- den Angehörigen der Elektronik- und Mechanikwerkstatt am IAP

- Marc Bienert und Giovanna Morigi für gute Zusammenarbeit und Diskussionen im Zusammenhang mit dem EIT-Kühlmechanismus

- unseren Postdocs, insbesondere Wolfgang und Artur. Wolfgang kann man immer alles fragen, nicht nur zur Physik; kann von ihm lernen, Dinge kritischer zu hinterfragen und aus verschiedenen Blickwinkeln zu sehen. Artur hält Paper-Diskussionen in Schwung und motiviert einen auch in schwierigen Situationen.

- den ehemaligen und aktuellen Kollegen am CQED-Experiment für die enge und konstruktive Zusammenarbeit in einer guten Atmosphäre, dabei insbesondere den Doktoranden Mika, Sebastian und René und den Diplomanden Alex, Martin und Stefan

- allen anderen Kollegen am Institut, insbesondere Kotya und Michał für viele hilfreiche Ratschläge und interessante Diskussionen

- meinem Bruder Timon für gute Tipps aus der Praxis

- meinen Eltern für ihre liebevolle Unterstützung